Doctor Thesis

Search for a stochastic background of gravitational waves at 100 MHz with laser interferometers

レーザー干渉計による 100 MHz 重力波背景放射の探査

Akutsu Tomotada
阿久津 智忠
Department of Astronomy, School of Science,
University of Tokyo
東京大学大学院理学系研究科天文学専攻

Submitted on December 19, 2007
Revised on February 27, 2008

Abstract

This thesis describes a direct search for a stochastic background of gravitational waves at very high frequencies ($\sim$ 100 MHz) by laser interferometry. We have developed a gravitational-wave detector, which is a pair of 75-cm baseline synchronous recycling (or resonant recycling) interferometers. This interferometer can detect gravitational waves at the frequencies with higher signal-to-noise ratio than a standard laser interferometric gravitational-wave detector based on a Michelson interferometer. Moreover, the signal-to-noise ratio can be improved by cross-correlating the outputs of the two interferometers. The synchronous recycling interferometer is formed by a four-mirror ring cavity (recycling cavity) and a Sagnac interferometer. The recycling cavity has a 75-cm baseline, and has a resonant response to gravitational waves at 100 MHz. The Sagnac interferometer responds to light fields that are induced by gravitational waves in the recycling cavity. For each synchronous recycling interferometer, a laser source is stabilized to the recycling cavity by the Pound-Drever-Hall technique. The gravitational-wave signals are downconverted into recordable low frequencies by optical and electrical local oscillators. Each interferometer has a shot-noise-limited strain sensitivity of about 10^{-16} $\mathrm{Hz}^{-1/2}$ and a signal bandwidth of about 1 MHz. After 1070-second data taking, uncorrelated noises between the two interferometers are reduced by the cross-correlation analysis with an optimal filter. Using a narrow bandwidth ($\sim$ 2 kHz) around 100.1 MHz, and assuming a flat spectrum of the gravitational-wave background in the bandwidth, we obtain a one-sided 90% upper limit of $h_0^2\Omega_{\mathrm{gw}} < 6 \times 10^{25}$ on the normalized energy density of gravitational-wave background per unit *logarithmic* frequency interval around 100 MHz.

Contents

Chapter 1

Introduction

Gravitational waves are ripples of spacetime curvature (propagating fields of spacetime strain) predicted by the theory of general relativity [1, 2]. The theory predicts that observable amounts of gravitational waves can be emitted from astronomical and cosmoligical phenomena: super nova, binary star system, black hole ringdown, primordial background, and so on. The existence of gravitational waves has been indirectly verified through the observation of the binary pulsar PSR B1913+16 (or, J1915+1606) [3, 4], but the direct detection of gravitational waves has not yet been achieved. This is because gravitational interactions are very weak.

There have been a lot of experiments to detect such weak signals. Resonant-mass detectors have been developed since 1960s [5]. Laser-interferometric detectors have been developed since 1970s [6]. Today, large-scale laser-interferometeric observatories have been constructed for detetcting gravitational waves from a few Hz to kHz (e.g. TAMA300 [7], LIGO [8], GEO600 [9], VIRGO [10], and CLIO [11]). There are future plans to construct large-scale interferometeric observatories with improved sensitivities (e.g. LCGT [12], enhanced/advanced LIGO, and so on). Also, there are future plans to construct space observatories (e.g. LISA [13] and DECIGO [14]) for detecting gravitational waves below 1 Hz.

There are many theoretical predictions of stochastic background of gravitational waves in a broad range of frequencies, $10^{-18} - 10^{10}$ Hz. Some models in cosmology and particle physics predict that there are large gravitational-wave background at very high frequency ~ 100 MHz. In the quintessential inflation model [15], the blue spectrum of gravitational-wave background is produced during the kinetic energy-dominated era after the inflationary expansion of the universe [16, 17, 18] and is very sensitive to subsequent reheating processes [19]. In other inflation models, during the first stage of the process of reheating, called preheating, gravitational waves at high frequencies are created due to large density inhomogeneities [20, 21, 22]. Pre-big-bang scenarios in string cosmology can also generate high-frequency backgrounds [23, 24, 25].

Not only cosmological sources but also compact objects can create gravitational-wave background at around 100 MHz. Primordial black holes produced in the early

universe, which have much smaller mass than the sun, emit gravitational waves via binary evolution and coalescence [26, 27] and evaporation [28]. There is a prediction that gravitational waves from black strings in the Randall-Sundrum model generate spectral features characteristic of the curvature of extra dimensions at high frequencies [29, 30].

Upper limits on gravitational-wave background in wide frequency ranges have been obtained from various observations:

- cosmic microwave radiation at $10^{-18} - 10^{-15}$ Hz [31],
- pulsar timing at $10^{-9} - 10^{-7}$ Hz [32],
- Doppler tracking of the Cassini spacecraft at $10^{-6} - 10^{-3}$ Hz [33],
- direct observation by LIGO at $10 - 10^{4}$ Hz [34], and
- helium-4 abundance due to big-bang nucleosynthesis at higher frequencies than 10^{-10} Hz [35].

Nevertheless, as far as we know, no direct experiment has been done above 100 kHz except for the experiment by A. M. Cruise and R. M. J. Ingley in Birmingham [36]. They have used a pair of electromagnetic waveguide loops, where the gravitational wave changes the polaizations of the electromagnetic wave [37]. Their detector has a strain sensitivity of $h \leq 10^{-14}$, and they obtain an upper limit on the amounts of gravitational-wave background as $h_0^2\Omega_{\rm gw} \leq 10^{34}$ at 100 MHz, where $\Omega_{\rm gw}$ is the normalized energy density of gravitational-wave background per unit logarithmic frequency [see Eq.(2.51)].

We have developed more sensitive detector for 100-MHz gravitational waves by laser interferometry. The detector is constructed at the Mitaka campus in Tokyo, National Astronomical Observatory of Japan. The detector consists of a pair of small-scale laser interferometers, each of which is a synchronous recycling interferometer (or resonant recycling interferometer). By cross-correlating two outputs of the interferometers, we improve the ratio of gravitational-wave signals to the detector noises.

Although the concept of the synchronous recycling technique was proposed in 1980s [38], our work is the first experiment to construct the interferometer for actual use. The synchronous recycling interferometer has an advantage for detecting the gravitational waves at such very high frequencies [40]. The frequency response of the interferometer to gravitaional waves has a resonant at a specific frequency (in our case 100 MHz) that depends on the baseline length [41, 42]. At a high frequency, the wavelength of gravitational wave is comparable to the size of a detector, which is the order of a few meters. The usual approximation that the wavelength of gravitational wave is much larger than the detector size is not valid. Therefore we have to use a detector design that is able to integrate gravitational-wave signals efficiently.

The contents of this thesis are as follows. Chapter 2 describes a breif derivation of gravitaional waves from the linearized Einstein equation, and connects the energy density of gravitational-wave background with the strain amplitude expression. Chapter 3

introduces the synchronous recycling interferometer, and shows its response function to gravitational waves. Using realistic parameters, we also derive a detection limit caused by a shot noise. Chapter 4 describes how to extract a required signal and a desired signal from the interferometer. We must lock the interferometer to its operation point in order to keep a high sensitivity to gravitational waves, and thus we require an error signal that is proportional to a deviation from the operation point. In addition, we require gravitational-wave signals; the original signals at around 100 MHz must be converted into the lower frequency to be recorded. Chapter 5 describes about our experiment. The structures and performances of the two interferometers are shown. Each interferometer achieves the strain sensitivitiy of about 10^{-16} $\mathrm{Hz}^{-1/2}$ at around 100 MHz. The strain sensitivity at around 100 MHz improves by two-order of magnitude compared to the previous best sensitivity by Cruise and Ingley [36]. Chapter 6 describes the results of cross-correlation analysis of the two outpus from the interferometers. We obtain the (one-sided 90% confidence) upper limit estimate $h_0^2\Omega_{\mathrm{gw}} < (6.0 \pm 1.2) \times 10^{25}$ at around 100 MHz. Chapter 7 describes discussions and future works, and Chapter 8 describes a conclusion of this thesis.

Chapter 2

Stochastic background of gravitational waves

2.1 Propagation of gravitational waves

In the theory of general relativity [1, 2], the interval ds^2 between adjacent two events (x^μ and $x^\mu + dx^\mu$) is written as

$$ds^2 = g_{\mu\nu}\, dx^\mu dx^\nu, \tag{2.1}$$

where $\mathsf{g} = \{g_{\mu\nu}\}$ is the metric tensor[1]. The metric tensor is derived from the Einstein equation

$$\mathsf{G} = \frac{8\pi G}{c^4}\mathsf{T}, \tag{2.2}$$

where $G \simeq 6.6742 \times 10^{-11}\,\mathrm{N\,m^2\,kg^{-2}}$ is Newton's constant, $c = 299792458\,\mathrm{m/s}$ is the speed of light in vacuum, and $\mathsf{T} = \{T_{\mu\nu}\}$ is the energy momentum tensor of objects. The Einstein tensor $\mathsf{G} = \{G_{\mu\nu}\}$ has generally ten independent componetns, which are functions of the metric tensor.

2.1.1 Linearized Einstein equation

The Einstein equation (2.1) is a set of nonlinear partial differential equations for the metric tensor. In Minkowski spacetime, the metric tensor is written as

$$g_{\mu\nu} = \eta_{\mu\nu} \equiv \begin{pmatrix} -1 & 0 & 0 & 0 \\ 0 & 1 & 0 & 0 \\ 0 & 0 & 1 & 0 \\ 0 & 0 & 0 & 1 \end{pmatrix}. \tag{2.3}$$

[1] This thesis follows the notation used in Refs [1, 2] on the indices of the components of tensors; greek letters ($\mu, \nu, \cdots = 0, 1, 2, 3$) represent a time coordinate and three spatial coordinates, and roman letters ($a, b, \cdots = 1, 2, 3$) represent three spatial coordinates.

On the other hand, with very weak gravity, the metric tensor is written as

$$g_{\mu\nu} = \eta_{\mu\nu} + h_{\mu\nu}, \qquad |h_{\mu\nu}| \ll 1, \tag{2.4}$$

where $h_{\mu\nu}$ represents metric perturbations by the gravity. In the weak gravity limit, Eq.(2.2) reduces to a set of linear equations. The linearized Einstein equation has a solution of propagating wave, that is, gravitational waves.

The linearized theory allows two kind of coordinate transformations: the global Lorentz transformation and the gauge transformation. The gauge transfomation is an infinitesimal transformation of coordinate system:

$$x^{\mu}_{\rm new} = x^{\mu}_{\rm old} + \xi^{\mu} \tag{2.5}$$

or,

$$h^{\rm new}_{\mu\nu} = h^{\rm old}_{\mu\nu} - \xi_{\mu,\nu} - \xi_{\nu,\mu}, \tag{2.6}$$

where $\{\xi^{\mu}\}$ is an arbitrary vector small enough to preserve $|h^{\rm new}_{\mu\nu}| \ll 1$. Then define a trace-reverse tensor:

$$\bar{h}^{\mu\nu} \equiv h^{\mu\nu} - \tfrac{1}{2}\eta^{\mu\nu}h, \tag{2.7}$$

where $h \equiv h^{\alpha}{}_{\alpha}$ is the trace of $h_{\mu\nu}$. The trace-reverse tensor $\bar{h}^{\mu\nu}$ has the same magnitude as $h_{\mu\nu}$, while the sign of its trace is reversed: $\bar{h}^{\alpha}{}_{\alpha} = -h^{\alpha}{}_{\alpha}$. Note that the gauge transformation Eq.(2.6) for the trace-reverse tensor is written as

$$\bar{h}^{\rm new}_{\mu\nu} = \bar{h}^{\rm old}_{\mu\nu} - \xi_{\mu,\nu} - \xi_{\nu,\mu} + \eta_{\mu\nu}\xi^{\alpha}{}_{,\alpha}. \tag{2.8}$$

When we use the Lorentz gauge, the trace-reverse tensor satisfies

$$\bar{h}^{\mu\nu}{}_{,\nu} = 0, \tag{2.9}$$

and the gauge transformation vector ξ^{μ} in Eq.(2.8) satisfies

$$\Box\,\xi^{\mu} = \bar{h}^{({\rm old})\mu\nu}{}_{,\nu}, \tag{2.10}$$

where d'Alembertian $\Box$ is defined as

$$\Box \equiv -\frac{1}{c^2}\frac{\partial^2}{\partial t^2} + \nabla^2.$$

Note that the Lorentz gauge is not defined uniquely; in other words, the coordinate system of an observer is not fully fixed by the condition Eq.(2.10). For example, consider another vector $\tilde{\xi}^{\mu}$ satisfying the condition

$$\Box\,\tilde{\xi}^{\mu} = 0, \tag{2.11}$$

then the new gauge by the transformation $\xi^{\mu} + \tilde{\xi}^{\mu}$ is also the Lorentz gauge, because the following relation is satisfied:

$$\Box(\xi^{\mu} + \tilde{\xi}^{\mu}) = \bar{h}^{({\rm old})\mu\nu}{}_{,\nu}. \tag{2.12}$$

In the Lorentz gauge, the Einstein tensor is simplified:

$$G_{\mu\nu} = -\frac{1}{2}\,\Box\,\bar{h}_{\mu\nu}. \tag{2.13}$$

Substituting Eq.(2.13) into Eq.(2.2) yields the linearized Einstein equation in the Lorentz gauge:

$$\Box\bar{h}^{\mu\nu} = -\frac{16\pi G}{c^4}T^{\mu\nu}, \tag{2.14a}$$

$$\bar{h}^{\mu\nu}{}_{,\nu} = 0. \tag{2.14b}$$

2.1.2 Propagating wave solutions in vacuum

In vacuum, the energy momentum tensor $T^{\mu\nu}$ in the right-hand side of Eq.(2.14a) vanishes, so Eq.(2.14) becomes

$$\Box\,\bar{h}^{\mu\nu} = 0, \tag{2.15a}$$

$$\bar{h}^{\mu\nu}{}_{,\nu} = 0. \tag{2.15b}$$

These equations consist of ten sourceless wave equations in Eq.(2.15a) and four conditions in Eq.(2.15b). One solution of Eq.(2.15a) is

$$\bar{h}^{\mu\nu} = \mathrm{Re}\,[A^{\mu\nu}\exp(\mathrm{i}k_\alpha x^\alpha)], \tag{2.16a}$$

$$k_\alpha k^\alpha = 0, \tag{2.16b}$$

while Eq.(2.15b) yields

$$A^{\mu\nu}k_\nu = 0. \tag{2.17}$$

Eq.(2.16b) means that the wave vector k^μ is a null vector, so the phase velocity of the wave is the same as the speed of light, c, while Eq.(2.17) means that the wave is plane (or transverse); in other words the propagating direction of the wave (wave vector k^μ) is orthogonal to its wavefront $A^{\mu\nu}$.

The solutions consist of ten components in Eq.(2.16a) and four conditions in Eq.(2.17). Thus the wave solution $\bar{h}^{\mu\nu}$ appears to have six independent components, but that is not true. As mentioned above, the Lorentz gauge condition Eq.(2.15b) does not fix uniquely the frame (or coordinate system) of the observer; the additional four conditions in Eq.(2.11) fix the frame. Thus only two components of $\bar{h}^{\mu\nu}$ remain independently.

Now select the gauge transformation vector ξ^μ in Eq.(2.8) so that $A^{\mu\nu}$ satisfies the relations:

$$A^\alpha{}_\alpha = 0, \tag{2.18a}$$

$$A_{\mu\nu}u^\nu = 0. \tag{2.18b}$$

This Lorentz gauge is known as the transverse-traceless gauge (TT gauge). Here, u^ν is an arbitrary constant time-like vector, which corresponds to the time axis of an observer. Note that Eq.(2.18a) has only three independent conditions, not four, owing to $k^\mu(A_{\mu\nu}u^\nu) = 0$. Instead, Eqs.(2.17) and (2.18) yield eight conditions to the amplitude $A^{\mu\nu}$. A metric tensor could have ten independent components, but now two components in $A^{\mu\nu}$ remain independently. The only two components have real physical existences, that is, the remaining two degrees of freedom will not vanish by any coordinate transformations.

Eq.(2.18a) leads to $\bar{h}^{\mu\nu} = h^{\mu\nu}$. As a result, the propagating wave solution in vacuum is written as

$$h_{\mu\nu} = \mathrm{Re}\left[A_{\mu\nu}\exp(\mathrm{i}k_\alpha x^\alpha)\right], \tag{2.19a}$$

$$k^\alpha k_\alpha = 0 \tag{2.19b}$$

with the conditions Eqs.(2.17) and (2.18). This is the gravitational wave.

Consider a gravitational wave propagating in the z direction. Then its wave vector is written as $\{k^\mu\} = (\omega/c, 0, 0, \omega/c)$, where ω is an angular frequency. When an observer selects the coordinate system to be $\{u^\mu\} = (1, 0, 0, 0)$ in Eq.(2.18b), the two independent components of $\{A_{\mu\nu}\}$ are represented by $A_+ \equiv A_{xx} = -A_{yy}$ and $A_\times \equiv A_{xy} = A_{yx}$, which are called plus polarization and cross polarization, respectively. As a whole, the gravitational wave is written as

$$h_{\mu\nu} = \mathrm{Re}\left[A_{\mu\nu}\mathrm{e}^{\mathrm{i}\omega(t-z/c)}\right], \tag{2.20a}$$

$$A_{\mu\nu} = \begin{pmatrix} 0 & 0 & 0 & 0 \\ 0 & A_+ & A_\times & 0 \\ 0 & A_\times & -A_+ & 0 \\ 0 & 0 & 0 & 0 \end{pmatrix}. \tag{2.20b}$$

For an observer at event $(t, \mathbf{X})$, where $\mathbf{X}$ is a spatial position vector, the spatial components of a gravitational wave propagating in the direction of $\mathbf{\Omega}$ (unit spatial vector) is written as

$$h_{ab}(t, \mathbf{X}; \mathbf{\Omega}) = h_+(t, \mathbf{X}; \mathbf{\Omega})\, e^+_{ab}(\mathbf{\Omega}) + h_\times(t, \mathbf{X}; \mathbf{\Omega})\, e^\times_{ab}(\mathbf{\Omega}) \tag{2.21}$$

$$= \sum_{A=+,\times} h_A(t, \mathbf{X}; \mathbf{\Omega})\, e^A_{ab}(\mathbf{\Omega}), \tag{2.22}$$

where h_+ and $h_\times$ are the amplitudes of the gravitational wave with plus and cross polarization, respectively. The polarization tensor $e^+_{ab}(\mathbf{\Omega})$ and $e^\times_{ab}(\mathbf{\Omega})$ represent the

plus polarization and cross polarization, respectively, and they are written as

$$\{e^{+}_{ab}\} = \mathbf{x}\otimes\mathbf{x} - \mathbf{y}\otimes\mathbf{y} \mapsto \begin{pmatrix} 1 & 0 & 0 \\ 0 & -1 & 0 \\ 0 & 0 & 0 \end{pmatrix} \tag{2.23}$$

$$\{e^{\times}_{ab}\} = \mathbf{x}\otimes\mathbf{y} + \mathbf{y}\otimes\mathbf{x} \mapsto \begin{pmatrix} 0 & 1 & 0 \\ 1 & 0 & 0 \\ 0 & 0 & 0 \end{pmatrix}, \tag{2.24}$$

where the unit spatial vectors $\mathbf{x}$ and $\mathbf{y}$ are orthogonal to each other, and orthogonal to $\boldsymbol{\Omega}$ as well. The set of $\mathbf{x}$ and $\mathbf{y}$ indicates a preferred coordinate system for the gravitational wave. Note that the linearized theory allows the global Lorentz transformation of the background spacetime, and one can treat $h_{\mu\nu}$ as if it were a tensor on Minkowski spacetime.

2.1.3 Effect of gravitational waves

Now let us investigate the effect of gravitational waves with test particles (free falling masses). Consider two test particles separated infinitesimally. The separation (spatial) vector ϵ^i follows the equation of geodesic deviation [1, 2]:

$$-\frac{1}{c^2}\frac{d^2}{dt^2}\epsilon^i = R^i{}_{0j0}\,\epsilon^j, \tag{2.25}$$

where $R^i{}_{0j0}$ is a component of Riemann tensor, which represents a spacetime curvature. The components of Riemann tensor is invariant with respect to the gauge transformation, so one can use the expression in the TT gauge as follows:

$$R^i{}_{0j0} = -\frac{1}{2c^2}\frac{\partial^2 h^i_j}{\partial t^2}. \tag{2.26}$$

Then Eq.(2.25) reduces to

$$\frac{\partial^2}{\partial t^2}\epsilon^i = \frac{1}{2}\frac{\partial^2 h^i{}_j}{\partial t^2}\epsilon^j. \tag{2.27}$$

The solution of this differential equation is

$$\epsilon^i = \left(\delta^i{}_j + \tfrac{1}{2}h^i{}_j\right)\epsilon^j_{(0)}, \tag{2.28}$$

where $\epsilon^i_{(0)}$ represents the initial separation vector (without gravitational waves). More explicitly, the above equation is

$$\begin{pmatrix} \epsilon^x \\ \epsilon^y \end{pmatrix} = \begin{pmatrix} 1+\frac{1}{2}h_+ & \frac{1}{2}h_\times \\ \frac{1}{2}h_\times & 1-\frac{1}{2}h_+ \end{pmatrix}\begin{pmatrix} \epsilon^x_{(0)} \\ \epsilon^y_{(0)} \end{pmatrix}. \tag{2.29}$$

Figure 2.1 illustrates the geodesic deviations induced by gravitational waves on a system of test particles located as a circle around an observor. If a gravitational wave

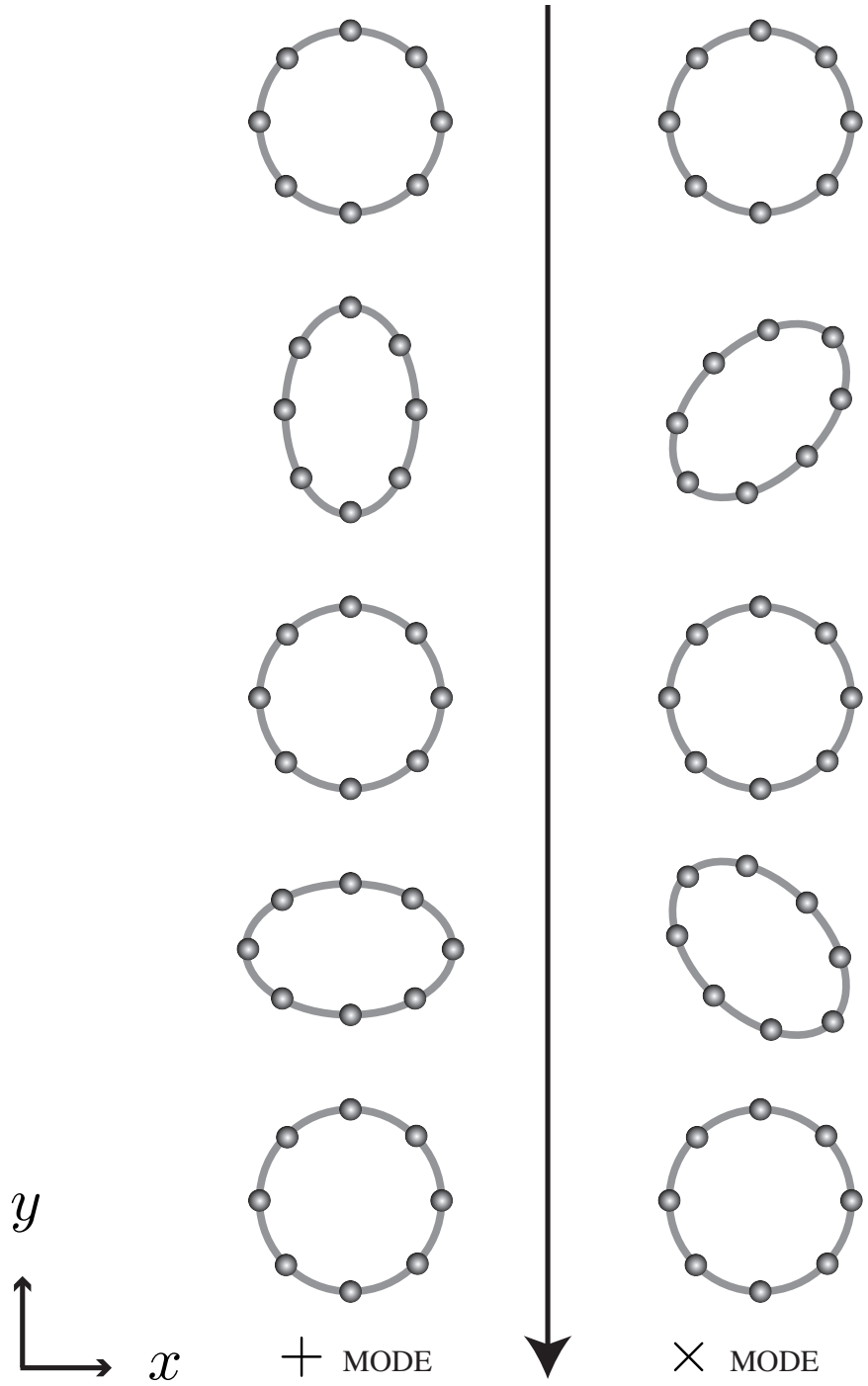

Figure 2.1 Effect of gravitational waves on a system of test particles (free masses) located as a circle on a flat surface. Here it is assumed that the gravitational wave is propagating in the orthogonal direction (or z-direction) to the surface of the particle system. The polarizations are indicated in the bottom: "+ MODE" for plus polarization and "× MODE" for cross polarization. The arrow in the center indicates the flow of time. The x, y coordinate axes are laid as shown.

is incident on the system in the z-direction, each particle fluctuates with respect to the observor (i.e. center of the circle), according to the polarization of the gravitational wave. Note that each particle follows its geodesic world line whether or not the gravitational wave is incident on the system; instead, the geodesics itselves are curved by the gravitational wave.

2.2 Stochastic background of gravitational waves

Here we assume that a stochastic background of gravitational waves is isotropic, unpolarized, stationary, and Gaussian, because we expect that the background arises from a superposition of gravitational waves propagating in different directions with different polarizations coming from a large number of unresolved and uncorrelated sources. Thus the background is considered to be a random process, which cannot be described by a mathematical function. Instead, the background can be characterized by its energy density.

2.2.1 All sky average

From Eq.(2.22), the total (*or* net) amplitude of a stochastic background of gravitational waves at a certain event $(t, \mathbf{X})$ is written as

$$h_{ab}(t, \mathbf{X}) = \sum_{A=+,\times} \int_{\Omega} h_A(t, \mathbf{X}; \mathbf{\Omega})\, e^A_{ab}(\mathbf{\Omega})\, d\mathbf{\Omega}, \tag{2.30}$$

where $\int_\Omega d\mathbf{\Omega}$ represents an integration over all sky:

$$\int_{\Omega} f(\mathbf{\Omega}) d\mathbf{\Omega} \equiv \int_0^{\pi} \sin\theta d\theta \int_0^{2\pi} d\phi\, f(\theta, \phi), \tag{2.31}$$

here the zenith angle $0 \leq \theta < \pi$ and azimuth angle $0 \leq \phi < 2\pi$ are defined as shown in Figure 2.2. The Fourier expansion of $h_A(t, \mathbf{X}; \mathbf{\Omega})$ is

$$h_A(t, \mathbf{X}; \mathbf{\Omega}) = \int_{-\infty}^{\infty} \tilde{h}_A(f; \mathbf{\Omega})\, \mathrm{e}^{\mathrm{i}2\pi f(t - \mathbf{X}\cdot\mathbf{\Omega}/c)}\, df, \tag{2.32}$$

and thus

$$h_{ab}(t, \mathbf{X}) = \sum_{A=+,\times} \int_{-\infty}^{\infty} df \int_{\Omega} d\mathbf{\Omega}\, \tilde{h}_A(f; \mathbf{\Omega})\, \mathrm{e}^{\mathrm{i}2\pi f(t - \mathbf{X}\cdot\mathbf{\Omega}/c)}\, e^A_{ab}(\mathbf{\Omega}). \tag{2.33}$$

2.2.2 Energy density of a gravitational-wave background

In the TT gauge (and in the linearized theory), the energy density of a gravitational wave is described as [1]

$$\rho_{\mathrm{gw}} = \frac{c^2}{32\pi G} \left\langle \dot{h}_{ab} \dot{h}^{ab} \right\rangle, \tag{2.34}$$

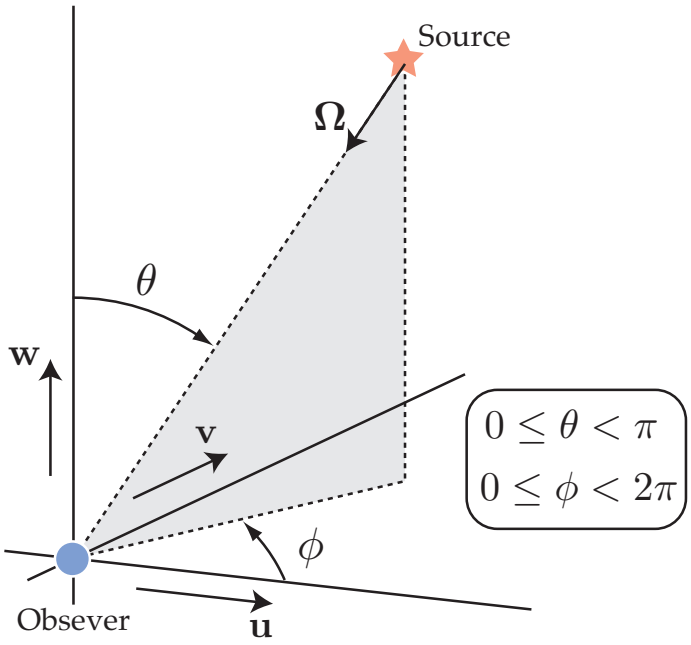

Figure 2.2 A source of gravitational waves and an observer. The zenith angle θ and the azimuth angle ϕ of the srouce are shown. The unit spatial vector $\mathbf{\Omega}$ points to the observer from the source. The unit vector triad $\{\mathbf{u}, \mathbf{v}, \mathbf{w}\}$ represents the obsetver's coordinate system.

where $\dot{h}_{ab}$ means the partial derivative of h_{ab} with respect to the coordinate time t, and $\langle \ldots \rangle$ indicates an average over several wavelengths. The stress-energy carried by a gravitational wave cannot be localized inside a single wavelength, but one can define the amount of the stress-enegy contained in a certain macroscopic area. Also the energy density can be decomposed as

$$\rho_{\rm gw} = \int_0^\infty \tilde{\rho}_{\rm gw}(f)\, df \tag{2.35}$$

$$= \int_{-\infty}^\infty \frac{1}{2}\tilde{\rho}_{\rm gw}(|f|)\, df, \tag{2.36}$$

where $\tilde{\rho}_{\rm gw}(f)$ indicates the gravitational-wave energy density per unit frequency interval.

By tradition, the intensity of a stochastic background of gravitational waves is expressed as a normalized energy density spectrum per unit *logarithmic* frequency interval:

$$\Omega_{\rm gw}(f) \equiv \frac{1}{\rho_{\rm c}} \frac{d\rho_{\rm gw}(f)}{d\ln f} \tag{2.37}$$

$$= f \frac{1}{\rho_{\rm c}} \frac{d\rho_{\rm gw}(f)}{df}, \tag{2.38}$$

where the term $\rho_{\rm gw}(f)$, which is the cumulative energy density of gravitational waves included below f Hz, is defined as

$$\rho_{\rm gw}(f) \equiv \int_0^f \tilde{\rho}_{\rm gw}(f)\, df = \int_0^f \frac{d\rho_{\rm gw}(f)}{df}\, df \tag{2.39}$$

$$= \int_{-\infty}^{\ln f} \tilde{\rho}_{\rm gw}(\ln f)\; d(\ln f). \tag{2.40}$$

Note that $\tilde{\rho}_{\rm gw}(\ln f)$ indicates the gravitational-wave energy density per unit logarithmic frequency interval. The normalization term $\rho_{\rm c}$ in Eq.(2.37) is the critical energy density defined as

$$\rho_{\rm c} \equiv \frac{3H_0^2c^2}{8\pi G} \tag{2.41}$$

$$\simeq 1.69 \times 10^{-9} h_0^2 \;\; {\rm J/m^3}, \tag{2.42}$$

where H_0 is the Hubble constant:

$$H_0 = h_0 \times 100 \;\; {\rm km/s/Mpc} \tag{2.43}$$

$$\simeq h_0 \times 3.241 \times 10^{-18} \;\; {\rm /s}, \tag{2.44}$$

here h_0 represents the experimental uncertainty in the Hubble constant. There are some estimates for the value of h_0; for example, one finds $h_0 \simeq 0.73$ using the WMAP data [43, 44].

With these expressions, the (total) gravitational-wave energy density $\rho_{\rm gw}$ [defined in Eq.(2.34)] is written as

$$\rho_{\rm gw} = \rho_{\rm gw}(f=\infty) = \int_0^\infty \tilde{\rho}_{\rm gw}(f)\, df. \tag{2.45}$$

The (total) normalized energy density of gravitational waves, which is defined as

$$\Omega_{\rm gw} \equiv \frac{\rho_{\rm gw}}{\rho_{\rm c}}, \tag{2.46}$$

is also written as

$$\Omega_{\rm gw} = \int_0^\infty \frac{\tilde{\rho}_{\rm gw}(f)}{\rho_{\rm c}}\, df = \int_0^\infty \tilde{\Omega}_{\rm gw}(f)\, df \tag{2.47}$$

$$= \int_0^\infty \frac{\Omega_{\rm gw}(f)}{f}\, df = \int_{-\infty}^\infty \tilde{\Omega}_{\rm gw}(\ln f)\, d(\ln f), \tag{2.48}$$

where $\Omega_{\rm gw}(f)$ and $\tilde{\Omega}_{\rm gw}(\ln f)$ both indicate the normalized energy density spectrum of gravitational waves per unit logarithmic frequency interval [see Eq.(2.37)]. This complication (for example, see Ref. [45]) arises from the traditional definition and notation of "$\Omega_{\rm gw}(f)$", which should be written as "$\tilde{\Omega}_{\rm gw}(\ln f)$" or something. Nevertheless, we will follow the traditional definition (2.37) in the remaining of this paper.

2.2.3 Effective amplitude spectrum density

The energy density of a gravitational-wave background $\Omega_{\rm gw}(f)$, is related to the experimentally measurable quantities as follows.

Here we introduce a quantity $h_{\rm rms}(f)$, which is called the one-sided effective amplitude spectrum density per unit frequency interval, and is defined as

$$\left\langle \tilde{h}^*_A(f;\mathbf{\Omega})\tilde{h}_{A'}(f';\mathbf{\Omega}')\right\rangle = \frac{1}{2}h^2_{\rm rms}(|f|)\delta(f-f')\frac{\delta^2(\mathbf{\Omega},\mathbf{\Omega}')}{4\pi}\delta_{AA'} \tag{2.49}$$

where $\langle\ldots\rangle$ represents an ensemble average. Then $h_{\rm rms}(f)$ is related to $\Omega_{\rm gw}(f)$ in the following form [35]:

$$\Omega_{\rm gw}(f) = \frac{4\pi^2}{3H_0^2}f^3h^2_{\rm rms}(f), \tag{2.50}$$

as shown later in this subsection. The normalized energy density $\Omega_{\rm gw}(f)$ is often represented in the following form:

$$h_0^2\Omega_{\rm gw}(f) = \frac{4\pi^2}{3}\frac{1}{(H_0/h_0)^2}f^3h^2_{\rm rms}(f) \tag{2.51}$$

$$\simeq 1.25\times10^{36}\left(\frac{f}{1\,\mathrm{Hz}}\right)^3 h^2_{\rm rms}(f) \tag{2.52}$$

$$\simeq 7.2\times10^{19}\left(\frac{f}{100\,\mathrm{MHz}}\right)^3\left(\frac{h_{\rm rms}(f)}{7.6\times10^{-21}}\right)^2, \tag{2.53}$$

so that one can avoid the uncertainty h_0 in the Hubble constant.

Now let us verify Eq.(2.50). Assume that the average over several wavelengths in Eq.(2.34) is, for the stochastic background, the same as a time average at a certain point, and the time average corresponds to the ensemble average [35]. From Eq.(2.33), the time derivative of h_{ab} is

$$\dot{h}_{ab}(t,\mathbf{X}) = \sum_{A=+,\times}\int_{-\infty}^{\infty}df\int_\Omega d\mathbf{\Omega}\ (\mathrm{i}2\pi f)\,h_A(f;\mathbf{\Omega})\,\mathrm{e}^{\mathrm{i}2\pi f(t-\mathbf{\Omega}\cdot\mathbf{X}/c)}e^A_{ab}(\mathbf{\Omega}). \tag{2.54}$$

The ensemble average of the square of the both side yields

$$\begin{aligned}\left\langle \dot{h}_{ab}(t,\mathbf{X})\dot{h}^{ab}(t,\mathbf{X})\right\rangle =& \sum_A\sum_{A'}\int_{-\infty}^{\infty}df\int_{-\infty}^{\infty}df'\int_\Omega d\mathbf{\Omega}\int_{\Omega'}d\mathbf{\Omega}'\\ &(2\pi f)(2\pi f')\langle h^*_A(f;\mathbf{\Omega})h_A(f';\mathbf{\Omega}')\rangle\,2\delta^{AA'}\\ &\mathrm{e}^{-\mathrm{i}2\pi(f-f')t}\,\mathrm{e}^{\mathrm{i}2\pi(f\mathbf{\Omega}-f'\mathbf{\Omega}')\cdot\mathbf{X}/c},\end{aligned} \tag{2.55}$$

where

$$e^A_{ab}(\mathbf{\Omega})e^{A'\,ab}(\mathbf{\Omega}) = 2\delta^{AA'}. \tag{2.56}$$

Substituting the above relation into Eq.(2.34) yields

$$\frac{c^2}{32\pi G}\sum_A\sum_{A'}\left\langle \tilde{h}_A^*(f;\mathbf{\Omega})\tilde{h}_{A'}(f';\mathbf{\Omega}')\right\rangle 2\delta^{AA'}(2\pi)^2 ff'\,\mathrm{e}^{-\mathrm{i}2\pi(f-f')t}\,\mathrm{e}^{\mathrm{i}2\pi(f\mathbf{\Omega}-f'\mathbf{\Omega}')\cdot\mathbf{X}/c}$$
$$=\frac{1}{2}\tilde{\rho}_{\mathrm{gw}}(|f|)\delta(f-f')\frac{\delta^2(\mathbf{\Omega},\mathbf{\Omega}')}{4\pi}, \tag{2.57}$$

where

$$\delta^2(\mathbf{\Omega},\mathbf{\Omega}')\equiv\delta(\phi-\phi')\delta(\cos\theta-\cos\theta') \tag{2.58}$$

and $4\pi=\int_\Omega d\mathbf{\Omega}\int_{\Omega'}d\mathbf{\Omega}'\delta^2(\mathbf{\Omega},\mathbf{\Omega}')$ is a normalization constant. Then one finds

$$\left\langle \tilde{h}_A^*(f;\mathbf{\Omega})\tilde{h}_{A'}(f';\mathbf{\Omega}')\right\rangle=\frac{32\pi G}{c^2}\frac{1}{(2\pi f)^2}\frac{1}{2}\tilde{\rho}_{\mathrm{gw}}(|f|)\delta(f-f')\frac{\delta^2(\mathbf{\Omega},\mathbf{\Omega}')}{4\pi}\frac{\delta_{AA'}}{4} \tag{2.59}$$
$$=\frac{G}{4\pi^2c^2}\frac{\tilde{\rho}_{\mathrm{gw}}(|f|)}{f^2}\delta(f-f')\delta^2(\mathbf{\Omega},\mathbf{\Omega}')\delta_{AA'}. \tag{2.60}$$

Substituting the relation:

$$\tilde{\rho}_{\mathrm{gw}}(f)=\rho_{\mathrm{c}}\frac{\Omega_{\mathrm{gw}}(f)}{f}, \tag{2.61}$$

which is derived from Eq.(2.38) and Eq.(2.39), into Eq.(2.60) yields the following form [46]:

$$\left\langle \tilde{h}_A^*(f;\mathbf{\Omega})\tilde{h}_{A'}(f';\mathbf{\Omega}')\right\rangle=\frac{3H_0^2}{32\pi^3}\frac{\Omega_{\mathrm{gw}}(|f|)}{|f|^3}\delta(f-f')\delta^2(\mathbf{\Omega},\mathbf{\Omega}')\delta_{AA'}. \tag{2.62}$$

Thus $\Omega_{\mathrm{gw}}(f)$ is explicitly related to $\langle h_A^*(f;\mathbf{\Omega})h_{A'}(f';\mathbf{\Omega}')\rangle$, and Eq.(2.50) is verified.

Chapter 3

Synchronous recycling interferometer

In this chapter, a synchronous recycling interferometer is introduced, then its response and sensitivity to gravitational waves is described.

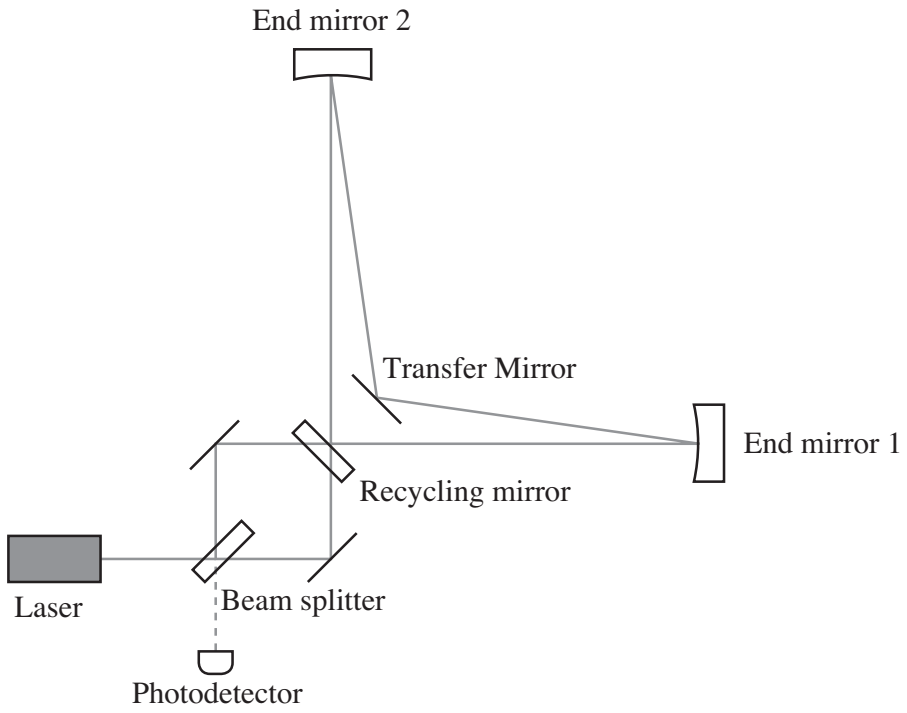

Figure 3.1 Schematic view of a synchronous recycling interferometer. A recycling cavity is formed by a recycling mirror (RM), a transfer mirror (TM), and two end mirrors (EM1 and EM2). A Sagnac part is formed by a beamsplitter (BS), the recycling cavity, and two steering mirrors. PD at the antisymmetric port represents a photodetector.

3.1 Optical configuration

A schematic view of a synchronous recycling interferomer is illustrated in Figure 3.1. The laser interferometer consists of two parts: a four-mirror ring cavity (hereafter recycling cavity) and a Sagnac interferometer (Sagnac part). The recycling cavity is formed by a recycling mirror (RM), a transfer mirror (TM), and two end mirrors (EM1 and EM2). The Sagnac part is formed by a beamsplitter (BS), a compound mirror (i.e. recycling cavity itself), and two steering mirrors.

The laser light enters the interferometer from the symmetric port of the Sagnac part. Then the light beam is divided into two directions with the BS before each beam is resonant the recycling cavity, where one of the beams is circulating in counter-clockwise (CCW) direction, while the other is circulating in clockwise (CW) direction.

The reflected light beam from the recycling cavity is recombined at the BS. Owing to the Sagnac part, the two beams experience the same optical paths in opposite directions, and interfere destructively at the antisymmetric port, so this port is also called "dark port". By contrast, if gravitatinoal waves at a specific frequency are incident on the interferometer, (in particular the recycling cavity), a part of the light leaks to the dark port. Therefore we can detect such a gravitatinoal wave by observing the dark port.

3.2 Recycling cavity response to gravtational waves

This section describes that gravitational waves shift the phase of the laser light and the amount of the phase shift is amplified in the recycling cavity.

Again the recycling cavity is a four-mirror ring cavity (see Figure 3.2), which is formed by a recycling mirror (RM), a transfer mirror (TM), end mirror 1 (EM1) and end mirror 2 (EM2). Here the amplitude reflectances of the TM, EM1, and EM2 are referred to as r_{t}, r_1, r_2, respectively. For the RM, the amplitude reflectance inside the recycling cavity is referred to as $+r_{\mathrm{r}}$, while the amplitude reflectance outside the recycling cavity is $-r_{\mathrm{r}}$; the transmittcace of the RM is t_{r}. When the distance between the RM and EM1 is L, the round-trip length of the recycling cavity is $4L$. In the remaining of this chapter, we assume that the two beams are resonant simultaneously in the recycling cavity, following the same optical paths but in opposite directions: CCW (RM→EM1→TM→EM2→RM) and CW (RM→EM2→TM→EM1→RM).

3.2.1 Phase shift of light

Assume that a gravitational wave with plus polarization is propagating in the vertical direction to the recycling cavity; in other words, set x, y-coordinate axes as shown

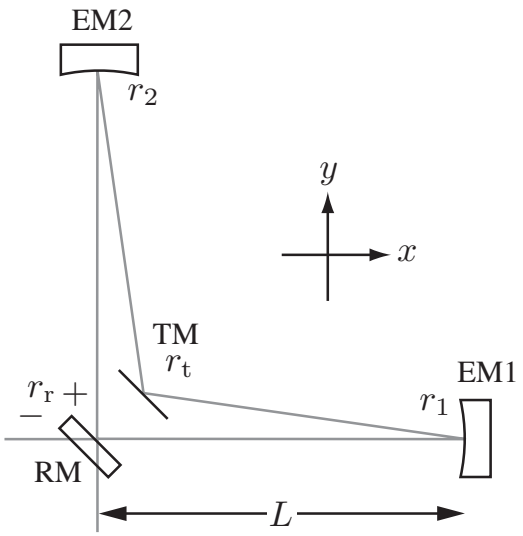

Figure 3.2 Recycling cavity.

in Figure 3.2, and z-axis perpendicular to this page, and then assume that a gravitational wave with plus polarization is propagating along the z-axis, in the $-z$ direction. Then the spacetime element [see Eq.(2.1)] in the TT gauge is written as

$$ds^2 = -c^2dt^2 + (1 + h(t))\,dx^2 + (1 - h(t))\,dy^2 + dz^2, \tag{3.1}$$

where $h(t)$ is the spacetime strain by the gravitational wave. The light beam follows the path $ds^2 = 0$; for the beam along x-axis,

$$ds^2 = -c^2dt^2 + (1 + h(t))\,dx^2 = 0, \tag{3.2}$$

while for the beam along y-axis,

$$ds^2 = -c^2dt^2 + (1 - h(t))\,dy^2 = 0. \tag{3.3}$$

Fisrt, consider the light beam along x-axis. Eq.(3.2) is transformed into

$$\frac{c\,dt}{\sqrt{1 + h(t)}} = dx. \tag{3.4}$$

The left-hand side can be reduced to

$$\left(1 - \tfrac{1}{2}h(t)\right)\,dt = dx/c, \tag{3.5}$$

owing to $|h(t)| \ll 1$. The integration of the both sides such that the light beam travels in a round trip of x direction gives

$$\int_{t-\Delta t_x}^{t} \left(1 - \frac{1}{2}h(t)\right)\,dt = \int_0^{2L} \frac{dx}{c} = \frac{2L}{c}, \tag{3.6}$$

where Δt_x is a time interval during which the light travels. Then the time interval is written as

$$\Delta t_x = \frac{2L}{c} + \frac{1}{2}\int_{t-\Delta t_x}^{t} h(t)\,dt \tag{3.7}$$

$$\simeq \frac{2L}{c} + \frac{1}{2}\int_{t-2L/c}^{t} h(t)\,dt. \tag{3.8}$$

In the same manner, the time interval during which the light travels in a round trip of y direction is

$$\Delta t_x \simeq \frac{2L}{c} - \frac{1}{2}\int_{t-2L/c}^{t} h(t)\,dt. \tag{3.9}$$

As a whole, the total round-trip time interval for the light beam in CCW is written as

$$\Delta t = \frac{4L}{c} + \frac{1}{2}\left\{\int_{t-4L/c}^{t-2L/c} - \int_{t-2L/c}^{t}\right\} h(t)\,dt. \tag{3.10}$$

Then the phase shift arising from the one round trip with gravitational waves is $\phi_1(t) = \Omega_0 \Delta t$, that is,

$$\phi_1(t) = \frac{4\Omega_0 L}{c} + \frac{\Omega_0}{2}\left\{\int_{t-4L/c}^{t-2L/c} - \int_{t-2L/c}^{t}\right\} h(t)\,dt. \tag{3.11}$$

In the same manner, the phase shift arising from the two round trips in CCW is written as

$$\phi_2(t) = \frac{8\Omega_0 L}{c} + \frac{\Omega_0}{2}\left\{\int_{t-8L/c}^{t-6L/c} - \int_{t-6L/c}^{t-4L/c} + \int_{t-4L/c}^{t-2L/c} - \int_{t-2L/c}^{t}\right\} h(t)\,dt. \tag{3.12}$$

Repeating the process, one can find the following equation:

$$\phi_n(t) = \frac{4n\Omega_0 L}{c} + \frac{\Omega_0}{2}\sum_{k=1}^{n}\left\{\int_{t-\frac{4L}{c}k}^{t-\frac{4L}{c}(k-\frac{1}{2})} - \int_{t-\frac{4L}{c}(k-\frac{1}{2})}^{t-\frac{4L}{c}(k-1)}\right\} h(t)\,dt \tag{3.13}$$

for the phase shift arising from the n-times round trips in CCW. Substituting the Fourier transformation of $h(t)$:

$$h(t) = \int_{-\infty}^{\infty} \tilde{h}(f) \mathrm{e}^{\mathrm{i}2\pi f t}\,df, \tag{3.14}$$

then

$$\phi_n(t) = \frac{4n\Omega_0 L}{c} + \frac{\Omega_0}{2}\int_{-\infty}^{\infty} -\tilde{h}(f)\,\frac{1}{\omega}\tan\left(\tfrac{L\omega}{c}\right)\left(1 - \mathrm{e}^{-\mathrm{i}\frac{4L\omega}{c}n}\right)\mathrm{e}^{\mathrm{i}2\pi f t}\,df, \tag{3.15}$$

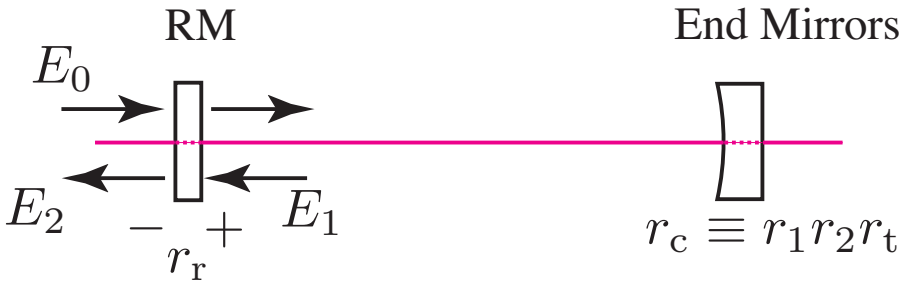

Figure 3.3 Fabry-Perot cavity equivalent to the recycling cavity.

where ω means $2\pi f$. Note that $\tilde{h}(f) = \tilde{h}^*(-f)$. In the right-hand side of Eq.(3.15), the second term (integration) represents the phase shift by gravitational waves; note that the first term represents the net round-trip phase (i.e. a phase evolution of light arising from the n-times round trips in the recycling cavity) and is nothing to do with gravitational waves.

3.2.2 Response of the recycling cavity

Now define a compound reflectance:

$$r_\mathrm{c} \equiv r_1 r_2 r_\mathrm{t}. \tag{3.16}$$

Then one can find the recycling cavity is similar to a Fabry-Perot cavity formed by two mirrors with amplitude reflectances r_r and r_c, respectively (see Figure 3.3). Consider that the light field entering the recycling cavity is written as $E_0 \mathrm{e}^{\mathrm{i}\Omega_0 t}$. Then the light field resonat in the recycling cavity is

$$E_1 = t_\mathrm{r} r_\mathrm{c} \mathrm{e}^{-\mathrm{i}\phi_1} E_0 + t_\mathrm{r} r_\mathrm{r} {r_\mathrm{c}}^2 \mathrm{e}^{-\mathrm{i}\phi_2} E_0 + \ldots \tag{3.17}$$

$$= t_\mathrm{r} r_\mathrm{c} \sum_{n=1}^{\infty} \left(r_\mathrm{r} r_\mathrm{c}\right)^{n-1} \mathrm{e}^{-\mathrm{i}\phi_n} E_0. \tag{3.18}$$

Witout gravitational waves,

$$\phi_n = 4nL\Omega_0/c = 2k\pi \quad (k \in \mathbb{Z}) \tag{3.19}$$

leads to $\exp(-\mathrm{i}\phi_n) = 1$ for all n, and thus

$$E_1 = \frac{t_\mathrm{r} r_\mathrm{c}}{1 - r_\mathrm{r} r_\mathrm{c}} E_0. \tag{3.20}$$

This equation is valid for both of the light beams resonant in the recycling cavity circulating in CCW and CW.

In case with gravitational waves, one can calculate the light field inside the recycling cavity by substituting Eq.(3.15) into Eq.(3.18) Note that the magnitude of the second

term in the right-hand side of Eq.(3.15) is relatively smaller than unity, so one can use the approximation

$$\exp(-\mathrm{i}\phi_n) \simeq \mathrm{e}^{-\mathrm{i}\frac{4\Omega_0 L}{c}n}\left\{1 - \mathrm{i}\frac{\Omega_0}{2}\int_{-\infty}^{\infty} -\tilde{h}(f)\,\frac{1}{\omega}\tan\left(\tfrac{L\omega}{c}\right)\left(1-\mathrm{e}^{-\mathrm{i}\frac{4L\omega}{c}n}\right)\mathrm{e}^{\mathrm{i}2\pi ft}\,df\right\}. \tag{3.21}$$

Then one finds the following relation for the CCW beam,

$$E_1 = \frac{t_\mathrm{r} r_\mathrm{c}}{1 - r_\mathrm{r} r_\mathrm{c}} E_0\{1 - \mathrm{i}\delta\phi(t)\}, \tag{3.22}$$

where the phase shift $\delta\phi(t)$ is written as

$$\delta\phi(t) = \int_{-\infty}^{\infty} \tilde{h}(f) H_\mathrm{sync}(f)\mathrm{e}^{\mathrm{i}2\pi ft}\,df. \tag{3.23}$$

The function $H_\mathrm{sync}(f)$, which is written as

$$H_\mathrm{sync}(f) = -\mathrm{i}\frac{\nu_0}{f}\frac{2\sin^2(\omega L/c)}{1 - r_\mathrm{r} r_\mathrm{c}\mathrm{e}^{-\mathrm{i}4\omega L/c}}\mathrm{e}^{-\mathrm{i}2\omega L/c}, \tag{3.24}$$

is the frequency response function of the recycling cavity to gravitational waves ($\omega = 2\pi f$). Note that $H_\mathrm{sync}(f) = H^*_\mathrm{sync}(-f)$. The term $\delta\phi(t)$ in Eq.(3.22) is a real number[1], so the equation states that the light beam is phase-modulated in the recycling cavity by gravitational waves.

In the same manner, one can find the following relation for the CW beam,

$$E_1 = \frac{t_\mathrm{r} r_\mathrm{c}}{1 - r_\mathrm{r} r_\mathrm{c}} E_0\{1 + \mathrm{i}\delta\phi(t)\}, \tag{3.25}$$

but the sign of the phase shift is reversed (opposite) with respect to Eq.(3.22).

3.2.3 Reflection from the recycling cavity

We will extract gravitational-wave signals from the light beam reflected from the recycling cavity. The reflected light $E_2\mathrm{e}^{\mathrm{i}\Omega_0 t}$ and the incident light $E_0\mathrm{e}^{\mathrm{i}\Omega_0 t}$ are related as follows:

$$E_2 = -r_\mathrm{r}E_0 + {t_\mathrm{r}}^2 r_\mathrm{c}\mathrm{e}^{-\mathrm{i}\phi_1}E_0 + {t_\mathrm{r}}^2{r_\mathrm{c}}^2 r_\mathrm{r}\mathrm{e}^{-\mathrm{i}\phi_2}E_0 + \ldots \tag{3.26}$$

$$= -r_\mathrm{r}E_0 + {t_\mathrm{r}}^2 r_\mathrm{c}\sum_{n=1}^{\infty}(r_\mathrm{r}r_\mathrm{c})^{n-1}\mathrm{e}^{-\mathrm{i}\phi_n}E_0, \tag{3.27}$$

[1] It can be shown using the relations: $\tilde{h}(f) = \tilde{h}^*(-f)$ and $H_\mathrm{sync}(f) = H^*_\mathrm{sync}(-f)$.

where ϕ_n is already defined in Eq.(3.15). Without gravitational waves, the relation Eq.(3.19) leads to $\exp(-\mathrm{i}\phi_n) = 1$ for all n, then the amplitude reflectance is

$$r_{\mathrm{reso}} = \frac{E_2}{E_0} = -r_{\mathrm{r}} + \frac{{t_{\mathrm{r}}}^2 r_{\mathrm{c}}}{1 - r_{\mathrm{r}} r_{\mathrm{c}}} \tag{3.28}$$

$$= \frac{-r_{\mathrm{r}} + ({r_{\mathrm{r}}}^2 + {t_{\mathrm{r}}}^2) r_{\mathrm{c}}}{1 - r_{\mathrm{r}} r_{\mathrm{c}}} \tag{3.29}$$

This equation is valid for both of the light beams circulating in CCW and CW in the recycling cavity.

In the same manner as Eq.(3.22), substituting Eq.(3.15) into Eq.(3.27) yields

$$r_{\mathrm{ccw}}(t) = \frac{E_2}{E_0} = r_{\mathrm{reso}} - \mathrm{i}\delta r(t), \tag{3.30}$$

where r_{ccw} is the amplitude reflectance of the recycling cavity, for the light incident on the cavity to be resonant in CCW. Here the term $\delta r(t)$ is defined as

$$\delta r(t) = \frac{{t_{\mathrm{r}}}^2 r_{\mathrm{c}}}{1 - r_{\mathrm{r}} r_{\mathrm{c}}} \delta\phi(t) \tag{3.31}$$

$$= \frac{{t_{\mathrm{r}}}^2 r_{\mathrm{c}}}{1 - r_{\mathrm{r}} r_{\mathrm{c}}} \int_{-\infty}^{\infty} \tilde{h}(f) H_{\mathrm{sync}}(f) \mathrm{e}^{\mathrm{i}2\pi f t}\, df. \tag{3.32}$$

In the same manner, the amplitude reflectance for the CW light is written as

$$r_{\mathrm{cw}}(t) = r_{\mathrm{reso}} + \mathrm{i}\delta r(t). \tag{3.33}$$

3.3 Recombine in the Sagnac part

The light component induced by gravitational wave can be extracted by the recombination at the BS in the Sagnac part (see Figure 3.4). Again the Sagnac part is formed by a beam splitter (BS), two steering mirrors (M1 and M2), and the compound mirror (i.e. the recycling cavity itself). Assume that the optics of the Sagnac part is aligned so that one round-trip path (BS→M1→RM→M2→BS) and the other round-trip path (BS→M2→RM→M1→BS) are completely overlapped. Then if the splitting ratio of the BS is 50/50 and the interferometer is set in a non-rotational frame, all the incident light to the Sagnac part is eventually reflected into the symmetric port (SP, or "bright port"), while the antisymmetric port (AP, or "dark port", "null port") is held on a dark fringe. On the other hand, if there is a difference between the lengths of the optical round-trip paths in the Sagnac part, a part of the incident light, which is proportional to the difference, will leak to the dark port[2].

[2] For example, the "Sagnac effect" arises from the rotation of the interferometer. This phenomenon is applied to a laser gyro in these days.

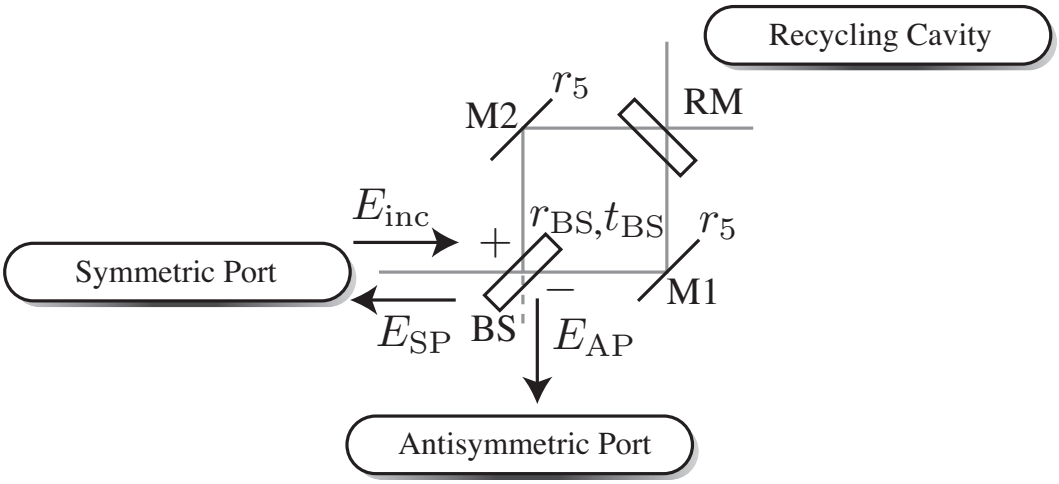

Figure 3.4 Sagnac interferometer part.

In Figure 3.4, r_5 is the amplitude reflectance of the M1 and M2[3], and $r_{\rm BS}$, $t_{\rm BS}$ are the amplitude reflectance and transmittance of the BS, respectively; the reflectance on the laser-entry side (or symmetric port) of the BS is referred to as $+r_{\rm BS}$, while the reflectance on the other side (or antisymmetric port) is $-r_{\rm BS}$.

When the light field $E_{\rm inc}e^{i\Omega_0 t}$ enters the synchronous recycling interferometer through the symmetric port, the light field that leaks to the antisymmetric port, $E_{\rm AP}e^{i\Omega_0 t}$, is written as

$$E_{\rm AP}(t) = E_{\rm inc}\left\{{t_{\rm BS}}^2\, r_{\rm cw}(t-2l/c) - {r_{\rm BS}}^2\, r_{\rm ccw}(t-2l/c)\right\} {r_5}^2 e^{-i\varphi_0} \tag{3.34}$$

$$= E_0 \Delta_{\rm BS}\, r_{\rm reso} {r_5}^2 e^{-i\varphi_0} + iE_{\rm inc}\left({t_{\rm BS}}^2 + {r_{\rm BS}}^2\right)\delta r(t-2l/c){r_5}^2 e^{-i\varphi_0}, \tag{3.35}$$

where $\varphi_0 = 4\Omega_0 l/c$ is a round-trip phase in the Sagnac interferometer ($4l$ is its round-trip length); $\Delta_{\rm BS}$ is defined as

$$\Delta_{\rm BS} \equiv {t_{\rm BS}}^2 - {r_{\rm BS}}^2. \tag{3.36}$$

As described in the previous subsection, gravitational waves modulate the phase of the light circulating in the recycling cavity. For simplicity, assume that a plus-polarized monochromatic gravitational wave

$$h(t) = h\cos(2\pi\nu_{\rm g} t) \tag{3.37}$$

is propagating in the vertical direction to the recycling caivty. Then the Fourier components of that gravitational wave [see Eq.(3.14)] is written as

$$\tilde{h}(f) = \frac{h}{2}\,\delta(f-\nu_{\rm g}) + \frac{h}{2}\,\delta(f+\nu_{\rm g}). \tag{3.38}$$

[3] Here we assume that M1 and M2 have the same reflectances, because only the product of these reflectances appear in the following calculation.

Substituting Eq.(3.38) into Eq.(3.35) via Eq.(3.32) yields

$$E_{\mathrm{AP}} = E_{\mathrm{inc}}\mathrm{e}^{-\mathrm{i}\varphi_0}\left(a_0 + a_1\mathrm{e}^{\mathrm{i}\omega_{\mathrm{g}}t} + a_{-1}\mathrm{e}^{-\mathrm{i}\omega_{\mathrm{g}}t}\right), \tag{3.39}$$

where $\omega_{\mathrm{g}} \equiv 2\pi\nu_{\mathrm{g}}$, and

$$a_0 = {r_5}^2\Delta_{\mathrm{BS}}\, r_{\mathrm{reso}}, \tag{3.40}$$

$$a_1 = \mathrm{i}({r_{\mathrm{BS}}}^2 + {t_{\mathrm{BS}}}^2){r_5}^2\frac{h}{2}\frac{{t_{\mathrm{r}}}^2 r_{\mathrm{c}}}{1 - r_{\mathrm{r}}r_{\mathrm{c}}}H_{\mathrm{sync}}(f)\mathrm{e}^{-\mathrm{i}\varphi_1}, \tag{3.41}$$

$$a_{-1} = \mathrm{i}({r_{\mathrm{BS}}}^2 + {t_{\mathrm{BS}}}^2){r_5}^2\frac{h}{2}\frac{{t_{\mathrm{r}}}^2 r_{\mathrm{c}}}{1 - r_{\mathrm{r}}r_{\mathrm{c}}}H_{\mathrm{sync}}(-f)\mathrm{e}^{\mathrm{i}\varphi_1} \tag{3.42}$$

$$= -a_1^*. \tag{3.43}$$

Here $\varphi_1 = 2\omega_{\mathrm{g}}l/c$ is the half round-trip phase in the Sagnac part.

3.4 Shot-noise-limited strain sensitivity

In Eq.(3.39), a_0 is a real number, while $a_1\mathrm{e}^{\mathrm{i}\omega_{\mathrm{g}}t} + a_{-1}\mathrm{e}^{-\mathrm{i}\omega_{\mathrm{g}}t}$ is a imaginary number; therefore the light field at the dark port can be stated as "phase-modulated light", if $\Delta_{\mathrm{BS}} \neq 0$ (i.e. $a_0 \neq 0$). Even though $\Delta_{\mathrm{BS}} \neq 0$, we cannot extract any signals that are linear to the amplitude of gravitatoinal waves, because the intensity of a phase-modulated light on average is constant. The practical scheme for the signal extraction is described in the next chapter. In the remaining of this chapter, the shot-noise-limited strain sensitivity of the synchronous recycling interferometer to gravitational waves is calculated in the ideal case — the homodyne detection scheme.

The homodyne detection scheme is the procedure described as follows. First, assume $\Delta_{\mathrm{BS}} = 0$, thus $a_0 = 0$. Then introduce an optical local oscillator (LO) at the dark port; the LO is a light field with the same frequency as the incident light to the interferometer, but is out of phase with the incident light by 90° so as to be amplitude-modulated by the gravitational-wave signals: a_1 and a_{-1}. Now let us express the LO by $E_{\mathrm{LO}}\mathrm{e}^{\mathrm{i}\Omega_0 t}$. Then the light field at the dark port is written as

$$E_{\mathrm{AP}} = E_{\mathrm{LO}}\mathrm{e}^{-\mathrm{i}\varphi_0} + E_{\mathrm{inc}}\mathrm{e}^{-\mathrm{i}\varphi_0}\left(a_1\mathrm{e}^{\mathrm{i}\omega_{\mathrm{g}}t} + a_{-1}\mathrm{e}^{-\mathrm{i}\omega_{\mathrm{g}}t}\right). \tag{3.44}$$

If the relative phase is set to

$$\arg\left(E_{\mathrm{LO}}/E_{\mathrm{inc}}\right) = -\pi/2, \tag{3.45}$$

then the time-averaged intensity of the light at the dark port, $\bar{P}_{\mathrm{AP}} \equiv k|E_{\mathrm{AP}}|^2$ (k is a proportional constant, for example 1/2), is written as

$$\bar{P}_{\mathrm{AP}} \simeq \bar{P}_{\mathrm{LO}} + 2\sqrt{\bar{P}_{\mathrm{LO}}\bar{P}_{\mathrm{inc}}}\,\mathrm{Im}\left[2\,a_1\mathrm{e}^{\mathrm{i}\omega_{\mathrm{g}}t}\right]. \tag{3.46}$$

The photodiode at the dark port creates the photocurrent

$$i_{\mathrm{AP}} = \eta\, e\, \frac{\bar{P}_{\mathrm{AP}}}{\hbar\,\Omega_0} \tag{3.47}$$

$$= \frac{\eta\, e}{\hbar\,\Omega_0}\left(\bar{P}_{\mathrm{LO}} + 2\sqrt{\bar{P}_{\mathrm{LO}}\bar{P}_{\mathrm{inc}}}\mathrm{Im}\left[2\,a_1 \mathrm{e}^{\mathrm{i}\omega_{\mathrm{g}}t}\right]\right) \tag{3.48}$$

$$= i_{\mathrm{dc}} + i_{\mathrm{sig}}(t), \tag{3.49}$$

where η is the quantum efficiency of the photodiode (i.e. η is the electron counts per unit photon); $e \simeq 1.60 \times 10^{19}\,\mathrm{C}$ is the electron charge (elementary charge); $\hbar \simeq 1.05 \times 10^{-34}\,\mathrm{m^2\,kg/s}$ is the reduced Planck constant (or, the Dirac constant). Now one can find

$$\mathrm{Im}\left[2\,a_1 \mathrm{e}^{\mathrm{i}2\pi\nu_{\mathrm{g}}t}\right] = ({r_{\mathrm{BS}}}^2 + {t_{\mathrm{BS}}}^2){r_5}^2\frac{h}{2}\frac{{t_{\mathrm{r}}}^2 r_{\mathrm{c}}}{1 - r_{\mathrm{r}}r_{\mathrm{c}}}\,\mathrm{Re}\left[2H_{\mathrm{sync}}(\nu_{\mathrm{g}})\mathrm{e}^{-\mathrm{i}\varphi_1}\mathrm{e}^{\mathrm{i}2\pi\nu_{\mathrm{g}}t}\right]. \tag{3.50}$$

From Eq.(3.38), the signal current is

$$i_{\mathrm{sig}}(t) = \frac{\eta\, e}{\hbar\,\Omega_0}2\sqrt{\bar{P}_{\mathrm{LO}}\bar{P}_{\mathrm{inc}}}({r_{\mathrm{BS}}}^2 + {t_{\mathrm{BS}}}^2){r_5}^2\int_{-\infty}^{\infty}\tilde{h}(f)G_{\mathrm{sync}}(f)\mathrm{e}^{-\mathrm{i}\varphi_1}\mathrm{e}^{\mathrm{i}2\pi ft}\,df, \tag{3.51}$$

where

$$G_{\mathrm{sync}}(f) \equiv \frac{{t_{\mathrm{r}}}^2 r_{\mathrm{c}}}{1 - r_{\mathrm{r}}r_{\mathrm{c}}}H_{\mathrm{sync}}(f) \tag{3.52}$$

is the frequency response function of the synchronous recycling interferometer to gravitational waves. The magnitude of the response function is written as

$$|G_{\mathrm{sync}}(f)| = |{r_{\mathrm{reso}}}'|\frac{\nu_0}{f}\frac{2\sin^2(\pi f/(2\nu_{\mathrm{FSR}}))}{\sqrt{1 + N^2\sin^2(\pi f/\nu_{\mathrm{FSR}})}}, \tag{3.53}$$

where $\nu_{\mathrm{FSR}} \equiv c/(4L)$ is the free-spectral range of the recycling cavity; $|{r_{\mathrm{reso}}}'| = {t_{\mathrm{r}}}^2 r_{\mathrm{c}}/(1 - r_{\mathrm{r}}r_{\mathrm{c}})^2$ is here called the synchronous recycling factor[4]; N is the folding number (number of circulation) of the light in the recycling cavity written as

$$N = \frac{2\sqrt{r_{\mathrm{r}}r_{\mathrm{c}}}}{1 - r_{\mathrm{r}}r_{\mathrm{c}}} \tag{3.54}$$

$$\simeq \frac{2}{\pi}\mathcal{F}, \tag{3.55}$$

where $\mathcal{F}$ is the finesse of the recycling cavity.

The one-sided amplitude spectrum density[5] of the shot noise in the photocurrent is

$$i_{\mathrm{shot}} = \sqrt{2\,e\,i_{\mathrm{dc}}} \tag{3.56}$$

$$= \sqrt{2\,e\,\frac{\eta\, e\bar{P}_{\mathrm{LO}}}{\hbar\,\Omega_0}} \tag{3.57}$$

[4] ${r_{\mathrm{reso}}}'$ is defined later in Eq.(4.14).

[5] More strictly, it is the square root of the one-sided power spectrum density per unit frequency interval.

in the unit of $\mathrm{A}/\sqrt{\mathrm{Hz}}$. Dividing this shot noise i_{shot} by the conversion factor [see Eq.(3.51)]

$$\frac{\tilde{i}_{\mathrm{sig}}(f)}{\tilde{h}(f)} = \frac{\eta\, e}{\hbar\,\Omega_0} 2\sqrt{\bar{P}_{\mathrm{LO}}\bar{P}_{\mathrm{inc}}}\,({r_{\mathrm{BS}}}^2 + {t_{\mathrm{BS}}}^2){r_5}^2 G_{\mathrm{sync}}(f)\mathrm{e}^{-\mathrm{i}\varphi_1}, \tag{3.58}$$

then the *shot-noise-limited strain sensitivity*, which is the amplitude spectrum density of the spacetime strain corresponding to the shot noise, is written as

$$h_{\mathrm{shot}}(f) = \sqrt{\frac{2\hbar\Omega_0}{\eta\bar{P}_{\mathrm{inc}}}}\,\frac{1}{2\,|G_{\mathrm{sync}}|}\,\frac{1}{({r_{\mathrm{BS}}}^2 + {t_{\mathrm{BS}}}^2){r_5}^2} \tag{3.59}$$

in the unit of $\mathrm{strain}/\sqrt{\mathrm{Hz}}$. The noise $h_{\mathrm{shot}}(f)$ is minimized for gravitational waves at $\nu_{\mathrm{g}} = \nu_{\mathrm{FSR}}$, where the response function $|G_{\mathrm{sync}}(f)|$ is maximized, and its value is

$$|G_{\mathrm{sync}}(f = \nu_{\mathrm{FSR}})| = 2|{r_{\mathrm{reso}}}'|\frac{\nu_0}{\nu_{\mathrm{FSR}}}, \tag{3.60}$$

where we assume $r_{\mathrm{BS}} = t_{\mathrm{BS}} = 1/\sqrt{2}$ and $r_5 = 1$ for simplicity. Note that if $r_{\mathrm{c}} = 1$ then $|{r_{\mathrm{reso}}}'| \simeq N \simeq 2\mathcal{F}/\pi$.

The value of the synchronous recycling factor $|{r_{\mathrm{reso}}}'|$ is different whether the recycling cavity is overcoupled ($r_{\mathrm{c}} > r_{\mathrm{r}}$) or undercoupled ($r_{\mathrm{r}} > r_{\mathrm{c}}$), regardless of the same finesse. If r_{c} is fixed then $|{r_{\mathrm{reso}}}'|$ is maximized at the critical coupling ($r_{\mathrm{r}} = r_{\mathrm{c}}$). If r_{r} is fixed then $|{r_{\mathrm{reso}}}'|$ is a monotonic increasing function of r_{c}, and maximized at $r_{\mathrm{c}} = 1$. Figure 3.5 shows plots of the synchoronous recycling factor $|{r_{\mathrm{reso}}}'|$ against the intensity reflectance of the RM ($R_{\mathrm{r}} \equiv {r_{\mathrm{r}}}^2$) for some fixed values of $R_{\mathrm{c}}^{1/3} \equiv {r_{\mathrm{c}}}^{2/3}$, each of which is attached to a respective plot. Here $R_{\mathrm{c}}^{1/3} \equiv {r_{\mathrm{c}}}^{2/3} = (r_1 r_2 r_{\mathrm{t}})^{2/3}$ corresponds to an average reflectance for TM, EM1, and EM2. The dashed curve represents critical coupling state. The area underneath the dashed curve (shaded reigion) represents under coupling state. The dashed curve follows the maximums of the plots. Note that $|{r_{\mathrm{reso}}}'|$ decreases with increased R_{c} when the recycling cavity is undercoupled[6], even though the finesse increases.

The response function $|G_{\mathrm{sync}}(\nu_{\mathrm{FSR}})|$ is $2|{r_{\mathrm{reso}}}'|$ times larger than that of Michelson inteferometer [see Eq.(A.22)]. The synchronous enhancement term $|{r_{\mathrm{reso}}}'|$ is the benefit of using the synchronous recycling interferometer. The other term '2' is from the configuration of the recycling cavity; even if the RM is removed (i.e. $N = 1$ if $r_{\mathrm{c}} = 1$), the recycling cavity integrates the effect of a gravitational wave at ν_{FSR} during one period, but the Michelson interferometer integrates it during at most only a half period.

[6] This situation (critical coupling) tends to occur in the recycling cavity because losses in the three mirrors decrease R_{c}, while the front mirror's reflectance is affected by only one mirror.

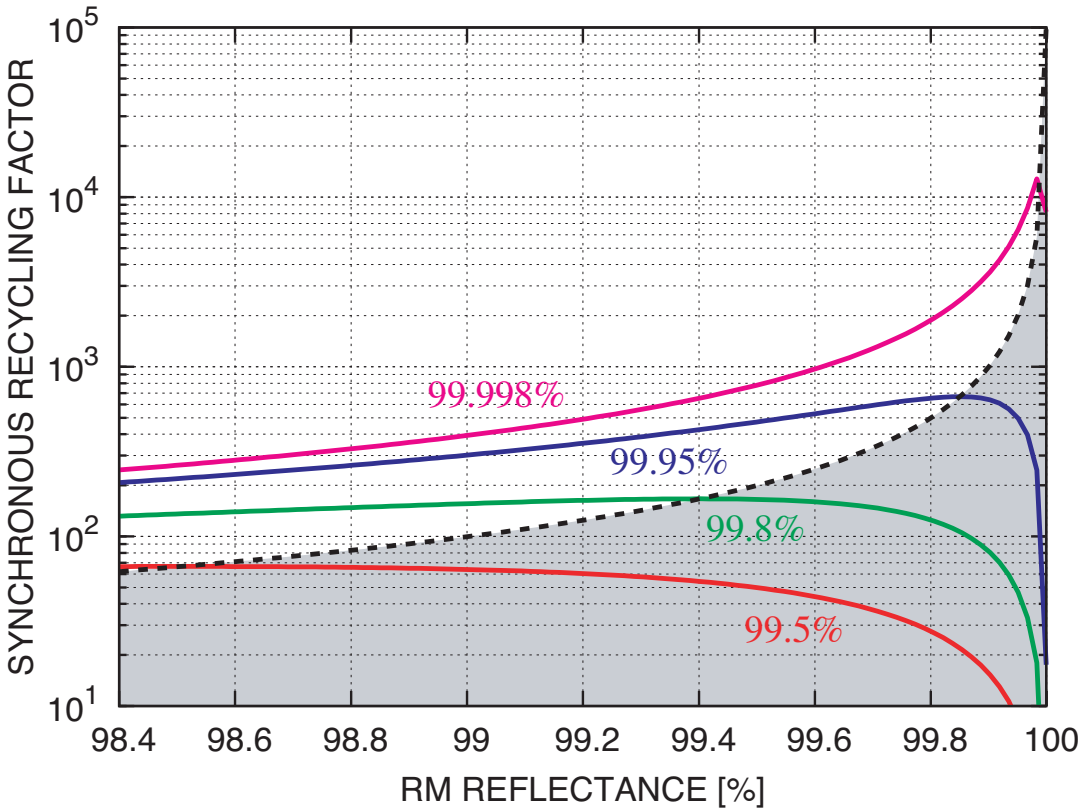

Figure 3.5 Variations of synchronous recycling factor $|r_{\mathrm{reso}}{}'|$ with respect to the (power) reflectance of RM. The horizontal and vertical axes represent R_{r} and $|r_{\mathrm{reso}}{}'|$, respectively. The number attached to each curve represents an averaged reflectance of EM1, EM2, and TM: $R_{\mathrm{c}}^{1/3} = (r_1 r_2 r_{\mathrm{t}})^{2/3}$. The dashed curve is the case of critical coupling: $R_{\mathrm{r}} = R_{\mathrm{c}}$. The shaded region represents the area of under coupling condition.

As a whole, the minimum output noise (corresponding to the shot noise) of the synchronous recycling interferometer tuned to a gravitational wave at ν_{g} is written as

$$h_{\mathrm{shot}}(\nu_{\mathrm{g}}) = \sqrt{\frac{2\hbar\Omega_0}{\eta \bar{P}_{\mathrm{inc}}}} \frac{\nu_{\mathrm{g}}}{4\nu_0} \frac{1}{|r_{\mathrm{reso}}{}'|} \tag{3.61}$$

in the unit of strain/$\sqrt{\mathrm{Hz}}$. A direct interpretation of Eq (3.61) is that the sensitivity can be improved infinitely by increasing $|r_{\mathrm{reso}}{}'|$ in principle.

Figure 3.6 shows the shot-noise-limited strain sensitivity of the synchronous recycling interferometer tuned to gravitational waves at $\nu_{\mathrm{g}} = 100$ MHz. The horizontal axis represents the frequency of gravitational waves. The vertical axis represents the output noise corresponding to amplitude of gravitational waves (square root of one-sided power spectrum density per unit frequency interval). The parameters used for the plot is listed in Table 3.1. At the observation frequency (100 MHz), one finds

Table 3.1 Parameters assumed in Figure 3.6.

Index	Parameters	Values
$\bar{P}_{\mathrm{inc}}$	Intensity of the light source	0.5 W
$\nu_0 = c/\lambda_0$	Frequency of the light source	$c/(1064\,\mathrm{nm})$ Hz
η	Quantum efficiency of the photodiode	1
$\nu_{\mathrm{FSR}} = c/(4L)$	Center frequency of the observation	100 MHz
r_{r}	Reflectance of the RM (amplitude)	$\sqrt{99.992\%}$
t_{r}	Transmittance of the RM (amplitude)	$\sqrt{1-{r_{\mathrm{r}}}^2}$
$r_{\mathrm{c}} \equiv r_1 r_2 r_{\mathrm{t}}$	Compound reflectance (amplitude)	$\sqrt{(99.998\%)^3}$

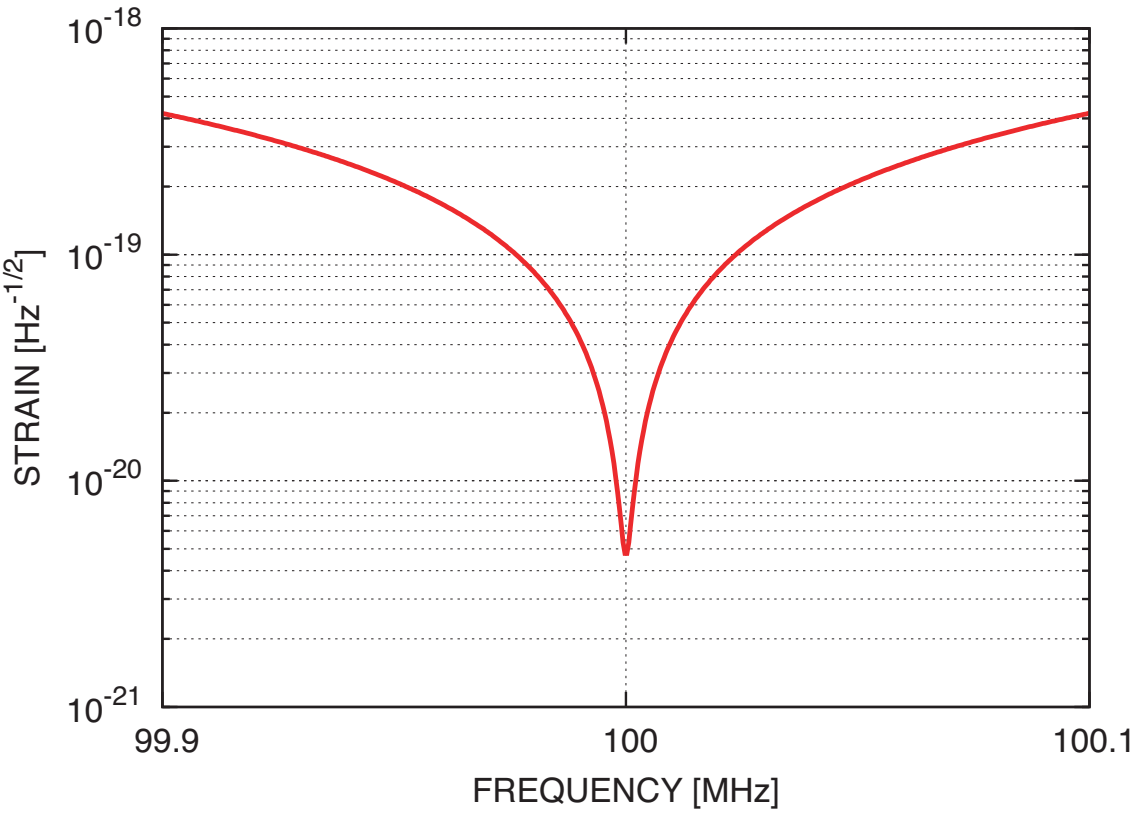

Figure 3.6 Shot-noise-limited strain sensitivity of a synchronous recycling interferometer (tuned at 100 MHz) is calculated. The parameters in 3.1 are used for the calculation. The sensitivity at 100 MHz is calculated to be 4.7×10^{-21} $\mathrm{Hz}^{-1/2}$.

$h_{\rm shot} \simeq 4.7 \times 10^{-21}$ strain/$\sqrt{\rm Hz}$. The finesse of the recycling cavity is $\mathcal{F} \simeq 4.5 \times 10^4$. For a Michleson interferometer with the same light source, the shot-noise-limited strain sensitivity at 100 MHz is about 1.5×10^{-16} strain/$\sqrt{\rm Hz}$; we are able to go beyond that limit, using the synchrous recycling interferometer.

3.5 All-sky averaged response

For the detection of a stochastic background, we have to consider gravitational waves coming from all the directions into the interferometer. Now the size of the interferometer is comparable to the target wavelength of gravitational waves[7], thus we should not use the low-frequency approximation [48].

Consider that there are spatial points $\mathbf{X}_i$ (position vector) and $\mathbf{X}_j$, and the distance between them is L. The phase evolution of light during the light travels from $\mathbf{X}_i$ to $\mathbf{X}_j$ is (for example, see Refs. [49, 50])

$$\phi_{ij}(t) = \frac{\Omega_0 L}{c} + \frac{\Omega_0}{2}\int_0^{L/c} h_{\mathbf{n}_{ij}}[t - (L + \mathbf{e}_z \cdot \mathbf{X}_i)/c + (1 - \mathbf{e}_z \cdot \mathbf{n}_{ij})t']\, dt', \tag{3.62}$$

where $\mathbf{n}_{ij} = (\mathbf{X}_j - \mathbf{X}_i)/L$, and $h_{\mathbf{n}_{ij}}(t)$ is a strain along the direction $\mathbf{n}_{ij}$, that is,

$$h_{\mathbf{n}_{ij}}(t) = \mathsf{h}(t) : (\mathbf{n}_{ij} \otimes \mathbf{n}_{ij}), \tag{3.63}$$

where[8]

$$\mathsf{h}(t) = \{h_{ab}\} = h_+(t)\mathsf{e}^+ + h_\times(t)\mathsf{e}^\times, \tag{3.64}$$

$$h_{ab}(t) = \sum_{A=+,\times} h_A(t)\, e^A_{ab}. \tag{3.65}$$

Now assume that the spatial origin of an observer's frame is at the RM. Then define $\mathbf{u}$ and $\mathbf{v}$ as unit vectors directed to the EM1 and EM2, respectively, from the RM. In other words, the EM1 is located at $L\mathbf{u}$, and the EM2 is located at $L\mathbf{v}$.

From Eq.(3.62), the phase evolution of the light during one round trip in the $\mathbf{u}$-direction is:

$$\begin{aligned}\Phi_{\mathbf{u}}(t) &\equiv \phi_{-L\mathbf{u}}(t) + \phi_{L\mathbf{u}}(t - L/c) \\ &= \frac{2\Omega_0 L}{c} + \frac{\Omega_0}{2}\int_0^{L/c} h_{\mathbf{u}}\left[t - 2L/c + (1 - \mathbf{e}_z \cdot \mathbf{u})t'\right] \\ &\qquad + h_{\mathbf{u}}\left[t + (t' - L/c)(1 + \mathbf{e}_z \cdot \mathbf{u})\right]\, dt'.\end{aligned} \tag{3.66}$$

Expand $h_{\mathbf{u}}(t)$ into the Fourier components

$$h_{\mathbf{u}}(t) = \int_{-\infty}^{\infty} \tilde{h}_{\mathbf{u}}(f)\, \mathrm{e}^{2\pi \mathrm{i} f t}\, df, \tag{3.67}$$

[7] The similar treat is needed in LISA [13, 47].

[8] The operator " : " is for contraction of tensors.

then

$$\Phi_{\mathbf{u}}(t) = \frac{2\Omega_0 L}{c} + \frac{\Omega_0 L}{c}\int_{-\infty}^{\infty} \tilde{h}_{\mathbf{u}}(f) P_{\mathbf{u}}(f)\, \mathrm{e}^{-2\mathrm{i}\pi f L/c}\, \mathrm{e}^{2\pi \mathrm{i} f t}\, df, \tag{3.68}$$

where

$$\begin{aligned} P_{\mathbf{u}}(f) =& \frac{1}{2}\Big\{ \mathrm{sinc}\left[\pi f \tfrac{L}{c}(1 - \mathbf{e}_z \cdot \mathbf{u})\right] \mathrm{e}^{-\mathrm{i}\pi f \frac{L}{c}(1+\mathbf{e}_z\cdot\mathbf{u})} \\ &+ \mathrm{sinc}\left[\pi f \tfrac{L}{c}(1 + \mathbf{e}_z \cdot \mathbf{u})\right] \mathrm{e}^{+\mathrm{i}\pi f \frac{L}{c}(1-\mathbf{e}_z\cdot\mathbf{u})} \Big\}. \end{aligned} \tag{3.69}$$

Note that $P_{\mathbf{u}}(-f) = P^*_{\mathbf{u}}(f)$ and $P_{-\mathbf{u}}(f) = P^*_{\mathbf{u}}(f)$. In the same manner,

$$\Phi_{\mathbf{v}}(t) = \frac{2\Omega_0 L}{c} + \frac{\Omega_0 L}{c}\int_{-\infty}^{\infty} \tilde{h}_{\mathbf{v}}(f) P_{\mathbf{v}}(f)\, \mathrm{e}^{-2\mathrm{i}\pi f L/c}\, \mathrm{e}^{2\pi \mathrm{i} f t}\, df, \tag{3.70}$$

where $P_{\mathbf{v}}(f)$ has the same form as $P_{\mathbf{u}}(f)$ in which $\mathbf{u}$ is replaced by $\mathbf{v}$.

The one round-trip phase in the recycling cavity in CW is

$$\Phi^{\mathrm{cw}}_1(t) = \Phi_{\mathbf{u}}(t) + \Phi_{\mathbf{v}}(t - 2L/c) \tag{3.71}$$

$$= \frac{4\Omega_0 L}{c} + \frac{\Omega_0 L}{c}\int_{-\infty}^{\infty} \tilde{H}^{\mathrm{cw}}(f)\, \mathrm{e}^{-\mathrm{i}2\pi f \frac{2L}{c}}\, \mathrm{e}^{\mathrm{i}2\pi f t}\, df, \tag{3.72}$$

where

$$\tilde{H}^{\mathrm{cw}}(f) = \tilde{h}_{\mathrm{u}}(f) P_{\mathrm{u}}(f) \mathrm{e}^{+\mathrm{i}2\pi f \frac{L}{c}} + \tilde{h}_{\mathrm{v}}(f) P_{\mathrm{v}}(f) \mathrm{e}^{-\mathrm{i}2\pi f \frac{L}{c}} \tag{3.73}$$

$$= \tilde{\mathsf{h}}(f) : \left\{ (\mathbf{u}\otimes\mathbf{u}) P_{\mathbf{u}}(f) \mathrm{e}^{+\mathrm{i}2\pi f \frac{L}{c}} + (\mathbf{v}\otimes\mathbf{v}) P_{\mathbf{v}}(f) \mathrm{e}^{-\mathrm{i}2\pi f \frac{L}{c}} \right\} \tag{3.74}$$

The last equation is derived from Eq.(3.63). The phase evolutions after the n round trips is

$$\Phi^{\mathrm{cw}}_n(t) = \sum_{k=1}^{n} \Phi_{\mathbf{u}}[t - 4(k-1)L/c] + \Phi_{\mathbf{v}}[t - (4(k-1)+2)L/c] \tag{3.75}$$

$$= \sum_{k=1}^{n} \Phi^{\mathrm{cw}}_1(t - 4(k-1)L/c) \tag{3.76}$$

$$= \frac{4n\Omega_0 L}{c} + \frac{\Omega_0 L}{c}\int_{-\infty}^{\infty} \tilde{H}^{\mathrm{cw}}(f) \frac{1 - \mathrm{e}^{-\mathrm{i}\frac{4L\omega}{c}n}}{2\mathrm{i}\sin\frac{2\omega L}{c}}\, \mathrm{e}^{\mathrm{i}2\pi f t}\, df. \tag{3.77}$$

In the same manner as Eq.(3.21), the phase shift by gravitational waves corresponding to Eq.(3.23) is calculated (in CW) as

$$E_1 = \frac{t_{\mathrm{r}} r_{\mathrm{c}}}{1 - r_{\mathrm{r}} r_{\mathrm{c}}} E_0 (1 - \mathrm{i}\delta\Phi^{\mathrm{cw}}(t)). \tag{3.78}$$

Then

$$\delta\Phi^{\mathrm{cw}}(t) = \int_{-\infty}^{\infty} \tilde{\mathsf{h}}(f) : \mathsf{H}^{\mathrm{cw}}_{\mathrm{sync}}(f)\, \mathrm{e}^{\mathrm{i}2\pi f t}\, df, \tag{3.79}$$

where the detector tensor is defined as (in CCW)

$$\mathsf{H}^{\mathrm{cw}}_{\mathrm{sync}}(f) = \frac{\Omega_0 L}{c}\frac{1}{1-r_{\mathrm{r}}r_{\mathrm{c}}\mathrm{e}^{-\mathrm{i}2\pi f/\nu_{\mathrm{FSR}}}}\mathrm{e}^{-\mathrm{i}2\pi f\frac{2L}{c}}\times \\ \left\{(\mathbf{u}\otimes\mathbf{u})P_{\mathbf{u}}(f)\mathrm{e}^{+\mathrm{i}2\pi f\frac{L}{c}} + (\mathbf{v}\otimes\mathbf{v})P_{\mathbf{v}}(f)\mathrm{e}^{-\mathrm{i}2\pi f\frac{L}{c}}\right\} \tag{3.80}$$

In the same manner, the one round-trip in CCW is

$$\Phi_1^{\mathrm{ccw}}(t) = \Phi_{\mathbf{v}}(t) + \Phi_{\mathbf{u}}(t-2L/c). \tag{3.81}$$

If we define $\delta\Phi^{\mathrm{ccw}}$ as

$$E_1 = \frac{t_{\mathrm{r}}r_{\mathrm{c}}}{1-r_{\mathrm{r}}r_{\mathrm{c}}}E_0(1-\mathrm{i}\delta\Phi^{\mathrm{ccw}}(t)), \tag{3.82}$$

then

$$\delta\Phi^{\mathrm{ccw}}(t) = \int_{-\infty}^{\infty}\tilde{\mathsf{h}}(f):\mathsf{H}^{\mathrm{ccw}}_{\mathrm{sync}}(f)\,\mathrm{e}^{\mathrm{i}2\pi ft}\,df, \tag{3.83}$$

where

$$\mathsf{H}^{\mathrm{ccw}}_{\mathrm{sync}}(f) = \frac{\Omega_0 L}{c}\frac{1}{1-r_{\mathrm{r}}r_{\mathrm{c}}\mathrm{e}^{-\mathrm{i}2\pi f/\nu_{\mathrm{FSR}}}}\mathrm{e}^{-\mathrm{i}2\pi f\frac{2L}{c}}\times \\ \left\{(\mathbf{u}\otimes\mathbf{u})P_{\mathbf{u}}(f)\mathrm{e}^{-\mathrm{i}2\pi f\frac{L}{c}} + (\mathbf{v}\otimes\mathbf{v})P_{\mathbf{v}}(f)\mathrm{e}^{+\mathrm{i}2\pi f\frac{L}{c}}.\right\} \tag{3.84}$$

Now redefine

$$r_{\mathrm{ccw}}(t) = r_{\mathrm{reso}} - \mathrm{i}\delta r_{\mathrm{ccw}}(t), \tag{3.85}$$
$$r_{\mathrm{cw}}(t) = r_{\mathrm{reso}} - \mathrm{i}\delta r_{\mathrm{cw}}(t). \tag{3.86}$$

Then the second term of Eq.(3.35) is written as

$$\mathrm{i}E_{\mathrm{inc}}\left(-{t_{\mathrm{BS}}}^2\delta r_{\mathrm{cw}}(t-2l/c) + {r_{\mathrm{BS}}}^2\delta r_{\mathrm{ccw}}(t-2l/c)\right){r_5}^2\mathrm{e}^{-\mathrm{i}\varphi_0}. \tag{3.87}$$

For simplicity, we assume $r_{\mathrm{BS}} = t_{\mathrm{BS}} = 1/\sqrt{2}$, then the term $\delta r(t)$ in Eq.(3.35) can be replaced by $(-\delta r_{\mathrm{cw}}(t)+\delta r_{\mathrm{ccw}}(t))/2$. Therefore the response tensor of the synchronous recycling interferometer, corresponding to $G_{\mathrm{sync}}(f)$ defined in Eq.(3.52), is written as

$$\mathsf{G}_{\mathrm{sync}}(f;\boldsymbol{\Omega}) = \frac{{t_{\mathrm{r}}}^2 r_{\mathrm{c}}}{1-r_{\mathrm{r}}r_{\mathrm{c}}}\frac{-\mathsf{H}^{\mathrm{cw}}_{\mathrm{sync}}(f;\boldsymbol{\Omega}) + \mathsf{H}^{\mathrm{ccw}}_{\mathrm{sync}}(f;\boldsymbol{\Omega})}{2} \tag{3.88}$$
$$= \frac{{t_{\mathrm{r}}}^2 r_{\mathrm{c}}}{1-r_{\mathrm{r}}r_{\mathrm{c}}}H_{\mathrm{sync}}(f)\,\mathsf{D}(f;\boldsymbol{\Omega}) \tag{3.89}$$
$$= G_{\mathrm{sync}}(f)\,\mathsf{D}(f;\boldsymbol{\Omega}), \tag{3.90}$$

where the *reduced* detector tensor[9] is written as

$$\mathsf{D}(f;\mathbf{\Omega}) \equiv \frac{(\mathbf{u}\otimes\mathbf{u})P_{\mathbf{u}}(f) - (\mathbf{v}\otimes\mathbf{v})P_{\mathbf{v}}(f)}{2\,\mathrm{sinc}\left[\frac{\pi}{2}\frac{f}{\nu_{\mathrm{FSR}}}\right]}. \tag{3.91}$$

In the low frequency limit ($f \to 0$),

$$\mathsf{D}(f:\mathbf{\Omega}) \simeq \frac{1}{2}\left(\mathbf{u}\otimes\mathbf{u} - \mathbf{v}\otimes\mathbf{v}\right). \tag{3.92}$$

Now consider

$$\tilde{\mathsf{h}}(f;\mathbf{\Omega}) : \mathsf{D}(f;\mathbf{\Omega}) = \left[\tilde{h}_+(f;\mathbf{\Omega})\,\mathsf{e}^+(\mathbf{\Omega}) + \tilde{h}_\times(f;\mathbf{\Omega})\,\mathsf{e}^\times(\mathbf{\Omega})\right] : \mathsf{D}(f;\mathbf{\Omega}) \tag{3.93}$$

$$= \tilde{h}_+(f;\mathbf{\Omega})D^+(f;\mathbf{\Omega}) + \tilde{h}_\times(f;\mathbf{\Omega})D^\times(f;\mathbf{\Omega}) \tag{3.94}$$

$$= \sum_{A=+,\times} \tilde{h}_A(f;\mathbf{\Omega})D^A(f;\mathbf{\Omega}), \tag{3.95}$$

where

$$D^+(f;\mathbf{\Omega}) \equiv \mathsf{e}^+(\mathbf{\Omega}) : \mathsf{D}(f;\mathbf{\Omega}), \tag{3.96}$$

$$D^\times(f;\mathbf{\Omega}) \equiv \mathsf{e}^\times(\mathbf{\Omega}) : \mathsf{D}(f;\mathbf{\Omega}). \tag{3.97}$$

Then the interferometer located at $\mathbf{X}_i$ outputs a raw voltage signal:

$$v_i(t) = \zeta_0 \sum_A \int_\Omega d\mathbf{\Omega} \int_{-\infty}^{\infty} df\, \tilde{h}_A(f;\mathbf{\Omega})G_{\mathrm{sync}}(f)D^A(f;\mathbf{\Omega})\; \mathrm{e}^{\mathrm{i}2\pi f(t-\mathbf{\Omega}\cdot\mathbf{X}_i/c)} \tag{3.98}$$

$$= \int_{-\infty}^{\infty} \tilde{v}_i(f)\,\mathrm{e}^{\mathrm{i}2\pi f t}\,df, \tag{3.99}$$

where ζ_0 represents a net transimpedance, with which the photocurrent at the dark port is converted into the raw voltage signal. When the raw signal is reduced by (practical) response function $\zeta_0\, G_{\mathrm{sync}}(f)$ in the frequency domain, the reduced signal $s_i(t)$ has a unit of strain amplitude:

$$s_i(t) = \sum_A \int_\Omega d\mathbf{\Omega} \int_{-\infty}^{\infty} df\, \tilde{h}_A(f;\mathbf{\Omega})D^A(f;\mathbf{\Omega})\; \mathrm{e}^{\mathrm{i}2\pi f(t-\mathbf{\Omega}\cdot\mathbf{X}_i/c)} \tag{3.100}$$

$$= \int_{-\infty}^{\infty} \tilde{s}_i(f)\,\mathrm{e}^{\mathrm{i}2\pi f t}\,df, \tag{3.101}$$

where

$$\tilde{s}_i(f) = \frac{1}{\zeta_0}\,\frac{\tilde{v}_i(f)}{G_{\mathrm{sync}}(f)} \tag{3.102}$$

$$= \sum_A \int_\Omega d\mathbf{\Omega}\, \tilde{h}_A(f;\mathbf{\Omega})D^A(f;\mathbf{\Omega})\,\mathrm{e}^{-\mathrm{i}2\pi f\mathbf{\Omega}\cdot\mathbf{X}_i/c}. \tag{3.103}$$

[9] The term "reduced" is attached so that one can distinguish $\mathsf{D}(f;\mathbf{\Omega})$ defined here from the "detector tensor" defined in Ref. [48].

The strain sensitivity (or strain noise) $h_{\rm sn}(f)$, which is the amplitude spectrum density of the spacetime strain corresponding to the interferometer output, is defined as

$$\langle \tilde{s}_i^*(f)\tilde{s}_i(f')\rangle \equiv \frac{1}{2}h_{\rm sn}^2(|f|)\delta(f-f'). \tag{3.104}$$

The strain sensitivity is one of the indicators to express the performance (i.e. amount of noises) of the interferometer. In the previous discussion, we already introduce the shot-noise-limited strain sensitivity $h_{\rm shot}(f)$; if one assumes that the shot noise dominates the interferometer output, $h_{\rm sn}(f) \simeq h_{\rm shot}(f)$, or

$$\langle \tilde{s}_i^*(f)\tilde{s}_i(f')\rangle \simeq \frac{1}{2}h_{\rm shot}^2(|f|)\delta(f-f'). \tag{3.105}$$

From Eq.(2.49), one finds

$$\begin{aligned}\langle \tilde{s}_i^*(f)\tilde{s}_i(f')\rangle =& \sum_A \sum_{A'} \int_\Omega d\mathbf{\Omega} \int_{\Omega'} d\mathbf{\Omega}' \\ & \left\langle \tilde{h}_A^*(f;\mathbf{\Omega})\tilde{h}_{A'}(f';\mathbf{\Omega}')\right\rangle \mathrm{e}^{+\mathrm{i}2\pi f \mathbf{X}_i\cdot\mathbf{\Omega}/c}\,\mathrm{e}^{-\mathrm{i}2\pi f' \mathbf{X}_j\cdot\mathbf{\Omega}'/c} \\ & \left[D^A(f;\mathbf{\Omega})\right]^* D^{A'}(f';\mathbf{\Omega}') \qquad (3.106)\\ =& \frac{1}{2}h_{\rm rms}^2(|f|)\delta(f-f')\frac{2}{5}\gamma_0(f), \qquad (3.107)\end{aligned}$$

where $\gamma_0(f)$ is

$$\gamma_0(f) = \frac{5}{8\pi}\sum_A \int_{\mathbf{\Omega}} d\mathbf{\Omega}\, \left[D^A(f;\mathbf{\Omega})\right]^* D^A(f;\mathbf{\Omega}), \tag{3.108}$$

which corresponds to the *reduced* overlap reduction function[10] defined in Eq.(6.32) for the co-aligned and co-located interferometers. The factor $5/(8\pi)$ is a normalization constant. In the low-frequency limit ($f \to 0$), $\gamma_0(f)$ goes to unity.

As a result, the strain sensitivity is related to the effective amplitude spectrum density as follows:

$$h_{\rm rms}(f) = \sqrt{\frac{5}{2}}\frac{1}{\sqrt{\gamma_0(f)}}\,h_{\rm sn}(f). \tag{3.109}$$

At 100 MHz, a numerical integration yields $\gamma_{0|100\ \rm MHz} \simeq 0.934$, thus

$$\begin{aligned}h_{\rm rms|100\ MHz} &\simeq 1.63\, h_{\rm sn|100\ MHz} \qquad (3.110)\\ &\simeq 7.6\times 10^{-21}\left(\frac{h_{\rm sn|100\,MHz}}{4.7\times 10^{-21}}\right)\ \mathrm{strain}/\sqrt{\mathrm{Hz}}\,. \qquad (3.111)\end{aligned}$$

[10] The term "reduced" is attached so that one can distinguish $\gamma_{12}(f)$ defined in Eq.(6.32) from the "overlap reduction function" defined in Ref. [48].

In terms of $\Omega_{\rm gw}(f)$ in Eq.(2.50), one finds

$$\Omega_{\rm gw}(f) = \frac{10\pi^2}{3H_0^2} f^3 \frac{1}{\gamma_0(f)} h_{\rm sn}^2(f). \tag{3.112}$$

In the low-frequency limit, $\gamma_0(f)$ goes to unity, thus one finds

$$\Omega_{\rm gw}(f) = \frac{10\pi^2}{3H_0^2} f^3 h_{\rm sn}^2(f), \tag{3.113}$$

which corresponds to the relation used for the background searches with LIGO (for example, see Refs. [51, 52, 34]).

Chapter 4

Signal extraction schemes

This chapter describes signal extraction schemes of (a) required signals for controlling the interferometer at its operation point and (b) desired signals induced by gravitational waves.

Our synchronous recycling interferometer has only one degree of freedom to be controlled: the relative fluctuation between the length of the recycling cavity and the wavelength of the laser light. In order that the laser light is stably resonant in the recycling cavity, the relative fluctuation or *error* must be well suppressed. The significant contribution to the error is in the low-frequency region, for example, due to the seismic noise or the acoustic noise. The error is suppress by a feedback control based on the Pound-Drever-Hall technique [53]. Note that the Sagnac part protects the antisymmetric port from length fluctuations in low frequency without controlling.

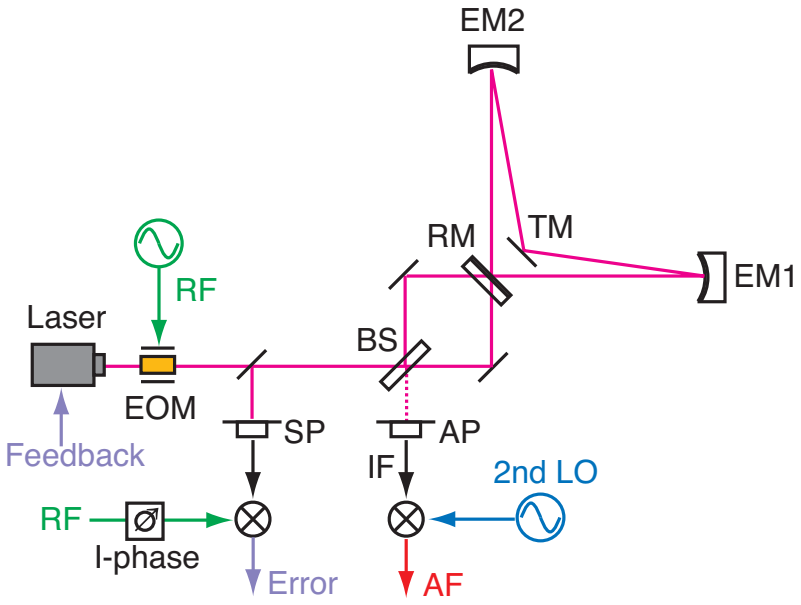

Figure 4.1 Schematic view of the signal extraction from the synchronous recycling interferometer.

The signal induced by gravitational waves at a specific frequency appears at the antisymmetric port or *dark port*. The spacetime strain carried by gravitational waves will modulate the phase of the light in the recycling cavity. In the Fourier space (i.e. frequency domain, see Figure 4.3), the modulation introduces *signal sidebands* spaced by the modulation frequency around the resonant light (against the sidebands, this component is called *carrier*). The Sagnac part distills the signal sidebands contained in the light reflected from the recycling cavity so that the signal sidebands appear at the dark port, and thus we can detect gravitational waves by observing the signal sidebands there.

4.1 Recycling cavity error signal

4.1.1 Relative phase fluctuation

When the relative fluctuation is well suppressed, the laser light is stably resonant in the recycling cavity.

With the Pound-Drever-Hall technique [53], we can relatively stabilize the frequency (or wavelength) of the laser light with respect to the length of the recycling cavity. In other words, the wavelength of the laser light is controlled to satisfy

$$4L = n\lambda_0, \tag{4.1}$$

where $\lambda_0 \simeq 1064$ nm is the wavelength, $4L \simeq 3$ m is the round-trip length of the recycling cavity, and n is a non-negative integer. In terms of the laser frequency, it is

$$\nu_0 = n\nu_{\mathrm{FSR}}, \tag{4.2}$$

where ν_0 is the frequency of the laser light, and $\nu_{\mathrm{FSR}} \equiv c/(4L)$ is the free-spectral range of the recycling cavity. In terms of the round-trip phase, it is

$$\phi = 2\pi\frac{\nu_0}{\nu_{\mathrm{FSR}}} = 2\pi n. \tag{4.3}$$

The so-called "relative phase fluctuation" is the fluctuation of the term of the left-hand side. Note that the relative phase ϕ fluctuates when either or both of ν_0 and L fluctuate.

4.1.2 Induction of the radio-frequency sidebands

Consider that the laser light field $E_0 e^{i\Omega_0 t}$, where $\Omega_0 = 2\pi\nu_0$, is phase-modulated with a modulation depth of β and a modulation frequency of $f_{\mathrm{RF}} = \omega_{\mathrm{m}}/(2\pi)$ before the light is incident on the interferometer (see Figure 4.1). Then the incident light

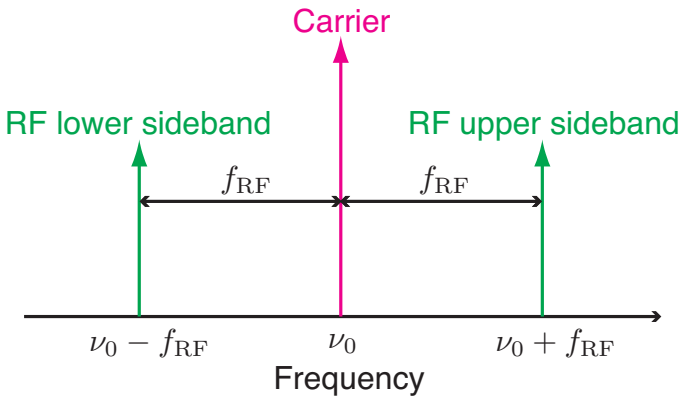

Figure 4.2 Laser light with the phase modulation at f_{RF} is illustrated in the frequency space. ν_0 is the physical frequency of the laser light source (or the carrier frequency). Upper and lower (first order) RF sidebands appear at $\nu_0 + f_{\mathrm{RF}}$ and $\nu_0 - f_{\mathrm{RF}}$, respectively

field E_{inc} is

$$E_{\mathrm{inc}} = E_0 \exp\left[\mathrm{i}\beta\cos(\omega_{\mathrm{m}}t)\right] \tag{4.4}$$

$$= E_0 \sum_{n=-\infty}^{\infty} \mathrm{i}^n J_n(\beta)\mathrm{e}^{\mathrm{i}n\omega_{\mathrm{m}}t}, \tag{4.5}$$

where $J_n(\beta)$ represents a n-th order Bessel function, which satisfies

$$J_{-n}(\beta) = (-1)^n J_n(\beta). \tag{4.6}$$

Eq.(4.5) reduces to

$$E_{\mathrm{inc}} \simeq J_0(\beta)E_0 + \mathrm{i}J_1(\beta)E_0\mathrm{e}^{\mathrm{i}\omega_{\mathrm{m}}t} + \mathrm{i}J_1(\beta)\mathrm{e}^{-\mathrm{i}\omega_{\mathrm{m}}t} \tag{4.7}$$

in the region of $\beta \ll 1$, where

$$J_0(\beta) \simeq 1, \tag{4.8}$$

$$J_1(\beta) \simeq \beta/2. \tag{4.9}$$

Thus the phase-modulated light has (about) three colors: carrier at ν_0, RF (radio-frequency) upper sideband at $\nu_0 + f_{\mathrm{RF}}$, and RF lower sideband at $\nu_0 - f_{\mathrm{RF}}$ (see Figure 4.2).

4.1.3 Response of the recycling cavity to the relative phase fluctuation

Now let us investigate the response of the recycling cavity to the relative phase fluctuation. The amplitude reflectance of the recycling cavity is

$$r_{\rm cav}(\Phi) \equiv -r_{\rm r} + \frac{{t_{\rm r}}^2 r_{\rm c} {\rm e}^{-{\rm i}\Phi}}{1 - r_{\rm r} r_{\rm c} {\rm e}^{-{\rm i}\Phi}}, \tag{4.10}$$

where $\Phi = 4\Omega_0 L/c$ is the round-trip phase of the recycling cavity. The derivative of $r_{\rm cav}(\Phi)$ with respect to Φ is

$$\begin{aligned} {r_{\rm cav}}'(\Phi) &\equiv \frac{\partial}{\partial \Phi} r_{\rm cav}(\Phi) & (4.11)\\ &= \frac{-{\rm i}{t_{\rm f}}^2 r_{\rm c} {\rm e}^{-{\rm i}\Phi}}{(1 - r_{\rm r} r_{\rm c} {\rm e}^{-{\rm i}\Phi})^2}. & (4.12) \end{aligned}$$

When the laser light is resonant in the cavity, the relative phase satisfies $\Phi = 2\pi k$ (k is a non-negative integer), and then

$$\begin{aligned} r_{\rm reso} &= -r_{\rm r} + \frac{{t_{\rm r}}^2 r_{\rm c}}{1 - r_{\rm r} r_{\rm c}}, & (4.13)\\ {r_{\rm reso}}' &= \frac{-{\rm i}{t_{\rm r}}^2 r_{\rm c}}{(1 - r_{\rm r} r_{\rm c})^2}. & (4.14) \end{aligned}$$

In these expressions, $r_{\rm reso}$ is a real number, and ${r_{\rm reso}}'$ is a imaginary number. Note that $|{r_{\rm reso}}'| \gg 1$ is called synchronous recycling factor in the previous chapter.

When the laser light is anti-resonant, the relative phase satisfies $\Phi = (2\pi + 1)k$ (k is a non-negative integer), and then

$$\begin{aligned} r_{\rm anti} &= -r_{\rm r} - \frac{{t_{\rm r}}^2 r_{\rm c}}{1 + r_{\rm r} r_{\rm c}}, & (4.15)\\ {r_{\rm anti}}' &= \frac{{\rm i}{t_{\rm r}}^2 r_{\rm c}}{(1 + r_{\rm r} r_{\rm c})^2}. & (4.16) \end{aligned}$$

In these expressions, they reduce to $r_{\rm anti} \simeq -1$ and ${r_{\rm anti}}' \simeq 0{\rm i}$, respectively.

Now illuminate the interferometer with the light field of Eq.(4.7). At the symmetric port, the backword light field $E_{\rm SP}$ is

$$E_{\rm SP} = E_0 \left(s_0 + s_1 {\rm e}^{{\rm i}\omega_{\rm m} t} + s_{-1} {\rm e}^{-{\rm i}\omega_{\rm m} t}\right) {\rm e}^{-{\rm i}\varphi_0}, \tag{4.17}$$

where

$$s_0 = J_0(\beta) 2 r_{\rm BS} t_{\rm BS} r_5^2 \, r_{\rm reso}, \tag{4.18}$$

$$s_1 = \mathrm{i} J_1(\beta) 2 r_{\rm BS} t_{\rm BS} r_5^2 \, r_{\rm anti} \mathrm{e}^{-\mathrm{i}\varphi_{\rm m}}, \tag{4.19}$$

$$s_{-1} = \mathrm{i} J_1(\beta) 2 r_{\rm BS} t_{\rm BS} r_5^2 \, r_{\rm anti} \mathrm{e}^{+\mathrm{i}\varphi_{\rm m}} \tag{4.20}$$

$$= -s_1^*. \tag{4.21}$$

The phase term $\varphi_{\rm m} = 4 l \omega_{\rm m}/c$ arises from the one round trip of RF sidebands in the Sagnac part.

The photocurrent at the symmetric port contains

$$i_{\rm SP1}(t) = \frac{\eta \, e \, \bar{P}_0}{\hbar \, \Omega_0} 2 \mathrm{Re} \left[\left(s_0 s_{-1}^* + s_1 s_0^* \right) \mathrm{e}^{\mathrm{i}\omega_{\rm m} t} \right], \tag{4.22}$$

In the Fourier frequency domain, $i_{\rm SP1}$ corresponds to the $f_{\rm RF}$ component of the photocurrent.

The photocurrent $i_{\rm SP1}$ is converted into a voltage signal and then demodulated to the baseband signal. The net transimpedance for the conversion and demodulation process is

$$\zeta \equiv g_{\rm dem} Z_{\rm pd} \frac{\eta \, e \, \bar{P}_0}{\hbar \, \Omega_0}, \tag{4.23}$$

where $Z_{\rm pd}$ is the transimpedance of the photodetector, and $g_{\rm dem}$ is the gain of the demodulator circuit (including the gain of the preamp of the double balanced mixer and so on). After the demodulation, we obtain the baseband signal

$$v = \zeta \frac{1}{\Delta t} \int_{t-\Delta t}^{t} 2 \mathrm{Re} \left[\left(s_0 s_{-1}^* + s_1 s_0^* \right) \mathrm{e}^{\mathrm{i}\omega_{\rm m} t} \right] \cos(\omega_{\rm m} t + \gamma) \, dt \tag{4.24}$$

$$\simeq \zeta \, \mathrm{Re} \left[\left(s_0 s_{-1}^* + s_1 s_0^* \right) \mathrm{e}^{-\mathrm{i}\gamma} \right], \tag{4.25}$$

where γ is a demodulation phase. The term $1/\Delta t$ corresponds to the cut-off frequency of the low-pass filter after the double balanced mixer. The term $\left(s_0 s_{-1}^* + s_1 s_0^* \right)$ comes out of the integral because the term is almost constant within the time interval of Δt, despite $\Delta t > 1/f_{\rm RF}$.

For simplicity, put $\varphi_{\rm m} = 0$. Then the demodulation phase $\gamma = 0$ is called I-phase (in phase), and $\gamma = \pi/2$ is called Q-phase (quadrature phase). The I-phase (demodulated) signal and the Q-phase signal are

$$v_{\rm I} = \zeta \, \mathrm{Re} \left[s_0 s_{-1}^* + s_1 s_0^* \right], \tag{4.26}$$

$$v_{\rm Q} = \zeta \, \mathrm{Im} \left[s_0 s_{-1}^* + s_1 s_0^* \right], \tag{4.27}$$

respectively. Substituting Eqs.(4.18), (4.19), and (4.20) yields

$$v_{\rm I} = v_{\rm Q} = 0. \tag{4.28}$$

Thus both of the signals vanish at the operation point of the recycling cavity. When the relative phase Φ fluctuates around the operation point $\Phi = 2\pi n$, the I-phase signal responds to the fluctuation as

$$\frac{\partial v_{\mathrm{I}}}{\partial \Phi} = \zeta \,\mathrm{Re}\left[(s_0'^{*} - s_0')s_1\right] \tag{4.29}$$

$$= \zeta \, 2J_0(\beta)J_1(\beta)\frac{{t_{\mathrm{r}}}^2 r_{\mathrm{c}}}{(1 - r_{\mathrm{r}} r_{\mathrm{c}})^2}, \tag{4.30}$$

where $r_{\mathrm{anti}} \simeq -1, {r_{\mathrm{anti}}}' \simeq 0\mathrm{i}$ are used and $r_{\mathrm{BS}} = t_{\mathrm{BS}} = 1/\sqrt{2},\ r_5 = 1$ are assumed. On the other hand, the Q-phase signal does not respond:

$$\frac{\partial v_{\mathrm{Q}}}{\partial \Phi} = \zeta \,\mathrm{Im}\left[(s_0'^{*} - s_0')s_1\right] \tag{4.31}$$

$$= 0. \tag{4.32}$$

Thus we find that the signal required for controlling the degree of freedom Φ, or *error signal*, comes from the I-phase signal at the symmetric port.

4.2 Signal sideband downconversion

This section describes the signal extraction scheme of gravitational waves. This scheme is used in the actual experiment described in the next chapter. The achievable sensitivity with the scheme is also described.

4.2.1 Overview of the downconversion scheme

The original signal at around ν_{FSR} ($\simeq 100\,\mathrm{MHz}$) is too fast to be sampled with an available data acquisition system. Thus we develop a scheme to convert the original signal into an electrical signal in the audio frequency range (see Figure 4.5). We reuse the RF sidebands at $\nu_0 \pm f_{\mathrm{RF}}$ (hereafter 1st LO), which are also used as the optical local oscillators for extracting the error signal from the recycling cavity (see previous section).

Consider a gravitational wave at the frequency of f_{GW} ($\simeq \nu_{\mathrm{FSR}}$). Then it produces signal sidebands at $\nu_0 \pm f_{\mathrm{GW}}$ around the carrier at ν_0 in the recycling cavity (see Figure 4.3). The signal sidebands appears at the dark port due to the discrimation by the Sagnac interferometer part. At the same time, the 1st LOs at $\nu_0 \pm f_{\mathrm{RF}}$ appear at the dark port if the BS has unequal splitting ratio: $\Delta_{\mathrm{BS}} \neq 0$ (see Figure 4.4). The beat between the 1st LO and the signal sidebands produces a photocurrent at $f_{\mathrm{IF}} = f_{\mathrm{GW}} - f_{\mathrm{RF}}$ at the photodetector in the dark port (see Figure 4.5). The photodetector is designed to have a resonance at $\nu_{\mathrm{FSR}} - f_{\mathrm{RF}}$ such that the signal-to-noise ratio of the photocurrent is improved. The signal is mixed with an electrical LO (2nd LO) at $f_{\mathrm{LO2}} = \nu_{\mathrm{FSR}} - f_{\mathrm{RF}} - \Delta f/2$ and then low-pass filterd. As a whole, the gravitational-wave signal at f_{GW} is downconverted to an elecrical signal at $f_{\mathrm{AF}} =$

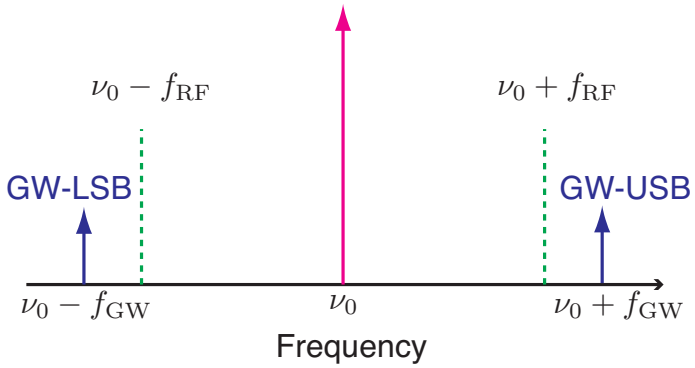

Figure 4.3 Light field in the recycling cavity with a gravitational wave at f_{GW} is illustrated in the frequency space. The gravitational wave induces signal sidebands around the carrier. The upper and lower signal sidebands appear at $\nu_0 + f_{\mathrm{GW}}$ and $\nu_0 - f_{\mathrm{GW}}$, respectively.

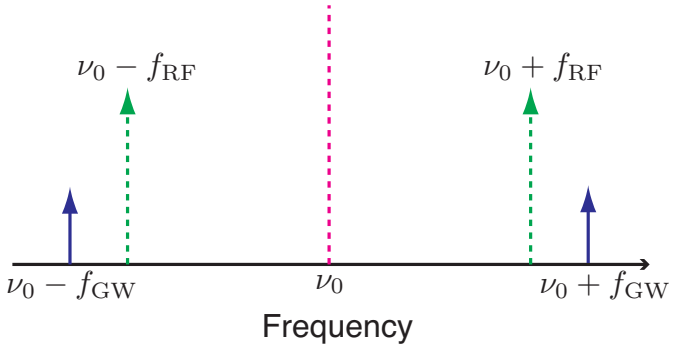

Figure 4.4 Light field at the antisymmetric port (AP), where RF sidebands (and carrier) appear if $\Delta_{\mathrm{BS}} \neq 0$, as well as GW signal sidebands.

$\nu_{\mathrm{FSR}} - f_{\mathrm{GW}} + \Delta f/2$. Note that the original signals at $f_{\mathrm{GW}} = \nu_{\mathrm{FSR}} - \Delta f/2$ and $\nu_{\mathrm{FSR}} + \Delta f/2$ are converted to the electrical signals at 0 Hz and Δf Hz, respectively.

4.2.2 Calculations

Consider that the inteferometer is illuminated by the light field Eq.(4.7). Then the light field at the AP is

$$E_{\mathrm{AP}} = E_0 \left(a_0 + a_1 \mathrm{e}^{\mathrm{i}\omega_{\mathrm{g}} t} + a_{-1} \mathrm{e}^{-\mathrm{i}\omega_{\mathrm{g}} t} + b_1 \mathrm{e}^{\mathrm{i}\omega_{\mathrm{m}} t} + b_{-1} \mathrm{e}^{-\mathrm{i}\omega_{\mathrm{m}} t}\right) \mathrm{e}^{-\mathrm{i}\varphi_0}, \tag{4.33}$$

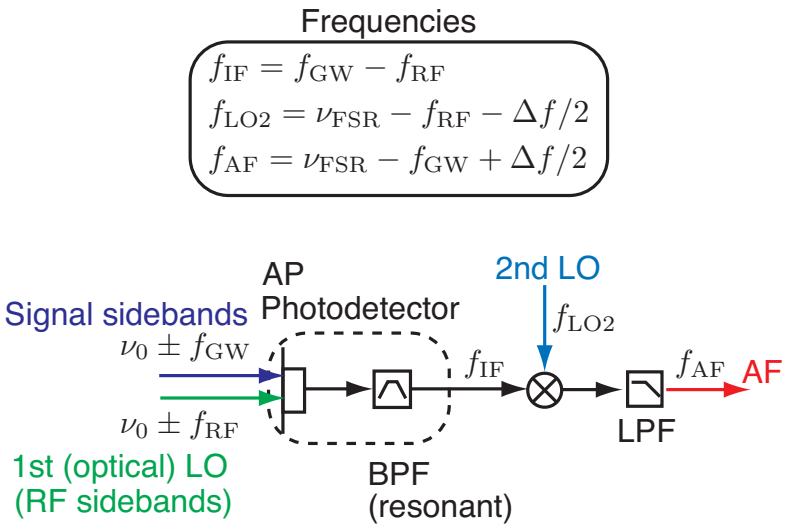

Figure 4.5 Schematic view of the downconversion of the gravitational-wave signal at the antisymmetric port (AP).

where

$$a_0 = J_0(\beta)\, {r_5}^2 \Delta_{\rm BS}\, r_{\rm reso}, \tag{4.34}$$

$$a_1 = {\rm i} J_0(\beta)\, ({r_{\rm BS}}^2 + {t_{\rm BS}}^2) {r_5}^2 \frac{h}{2} G_{\rm sync}(\omega_{\rm g}) {\rm e}^{-{\rm i}\varphi_1}, \tag{4.35}$$

$$a_{-1} = -a_1^*, \tag{4.36}$$

$$b_1 = {\rm i} J_1(\beta)\, \Delta_{\rm BS}\, {r_5}^2 r_{\rm anti} {\rm e}^{-{\rm i}\varphi_{\rm m}}, \tag{4.37}$$

$$b_{-1} = -b_1^*. \tag{4.38}$$

From the relation $\bar{P}_{\rm AP} = k|E_{\rm AP}|^2$, the photocurrent is

$$i_{\rm AP} \simeq \frac{\eta\, e \bar{P}_0}{\hbar\, \Omega_0} \left\{ (|a_0|^2 + 2|b_1|^2) + 4{\rm Re}\left[a_1 b_1^* {\rm e}^{{\rm i}(\omega_{\rm g} - \omega_{\rm m})t} \right] + \dots \right\} \tag{4.39}$$

$$= i_{\rm AP0} + i_{\rm AP1}(t) + \dots, \tag{4.40}$$

where $i_{\rm AP1}(t)$ is the photocurrent signal caused by gravitational waves. The angular frequency of the photocurrent is downconverted to

$$\omega_{\rm if} \equiv \omega_{\rm g} - \omega_{\rm m}, \tag{4.41}$$

where they satisfy $\omega_{\rm m} < \omega_{\rm g}$. Then one finds

$$i_{\rm AP1}(t) = \frac{\eta e \bar{P}_0}{\hbar \Omega_0} 4 J_0(\beta) J_1(\beta)\, ({r_{\rm BS}}^2 + {t_{\rm BS}}^2)\, r_5^4 \Delta_{\rm BS} r_{\rm anti} \frac{h}{2} {\rm Re}\left[G_{\rm sync}(\omega_{\rm if} + \omega_{\rm m}) {\rm e}^{-{\rm i}(\varphi_1 - \varphi_{\rm m})} {\rm e}^{{\rm i}\omega_{\rm if} t} \right]. \tag{4.42}$$

Now assume a monochromatic gravitational wave, then

$$i_{\rm AP1}(t) = i_{\rm AP1} \cos(\omega_{\rm if} t + \phi_{\rm if}). \tag{4.43}$$

The conversion coefficient between the gravitational waves and the photocurrent is

$$\left|\frac{i_{\mathrm{AP1}}(\omega_{\mathrm{if}})}{h(\omega_g)}\right| = \frac{\eta e\bar{P}_0}{\hbar\Omega_0} 2J_0(\beta)J_1(\beta)\left({r_{\mathrm{BS}}}^2 + {t_{\mathrm{BS}}}^2\right) r_5^4 |\Delta_{\mathrm{BS}}||r_{\mathrm{anti}}|\,|G_{\mathrm{sync}}(\omega_{\mathrm{if}}+\omega_{\mathrm{m}})| \quad (4.44)$$

Note that the original gravitational waves has an angular frequency of ω_{g}, but the corresponding photocurrent has an angular frequency of ω_{if}.

The (angular) frequency component of the shot noise, which contributes to the noises in the interferometer output, is also ω_{if}, not ω_{g}. The shot noise is flat in the frequency space (white spectrum), thus

$$i_{\mathrm{shot}} = \sqrt{2ei_{\mathrm{AP0}}} \quad (4.45)$$

$$= \sqrt{2e\frac{\eta e\bar{P}_0}{\hbar\Omega_0}(|a_0|^2 + 2|b_1|^2)} \quad (4.46)$$

$$= r_5^2|\Delta_{\mathrm{BS}}|\sqrt{2e\frac{\eta e\bar{P}_0}{\hbar\Omega_0}(J_0^2(\beta){r_{\mathrm{reso}}}^2 + 2J_1^2(\beta){r_{\mathrm{anti}}}^2)} \quad (4.47)$$

in the unit of $\mathrm{A}/\sqrt{\mathrm{Hz}}$. From Eq.(4.44), the contributions from the shot noise is

$$h_{\mathrm{shot}}(\omega_{\mathrm{g}}) = \sqrt{\frac{2\hbar\Omega_0}{\eta\bar{P}_0}}\,\frac{\sqrt{2}}{2|G_{\mathrm{sync}}(\omega_{\mathrm{g}})|}\,\frac{1}{f(\beta)}\,\frac{1}{r_5^2({r_{\mathrm{BS}}}^2 + {t_{\mathrm{BS}}}^2)}, \quad (4.48)$$

where

$$f(\beta) = \sqrt{\frac{2J_0(\beta)^2J_1(\beta)^2{r_{\mathrm{anti}}}^2}{J_0^2(\beta){r_{\mathrm{reso}}}^2 + 2J_1^2(\beta){r_{\mathrm{anti}}}^2}} \quad (4.49)$$

is called the penalty factor. The beamsplitter asymmetries Δ_{BS} are in the numerator and denominator, thus they are cancelled out. If it satisfies ${r_{\mathrm{BS}}}^2 + {t_{\mathrm{BS}}}^2 = 1$, the signal-to-noise ratio does not decrease whatever Δ_{BS} is (except for zero, in principle).

In the ideal situation described in Eq.(3.59), the condition $r_{\mathrm{BS}} = t_{\mathrm{BS}}$ is required for the maximum signal-to-noise ratio. On the other hand, with the signal extraction scheme described here, the signal-to-noise ratio does not change even if $r_{\mathrm{BS}} = 1, t_{\mathrm{BS}} = 0$. In fact, a photodetector can accept a limited amout of light, thus Δ_{BS} should not be so large. On the other hand, if Δ_{BS} is too small, the desired signal is obscured by various noises: the undesirable light, the thermal noise inherent in the photodetector, and so on.

The penalty factor $f(\beta)$ ranges from 0 to 1. For example, the penalty factor of the Michelson interferometer controlled with the frontal modulation scheme (or Schnupp modulation scheme [54]) is $f(\beta) \simeq |J_0(\beta)|$ as described in Eq.(A.38). This factor satisfies $f(\beta) \to 1$ when $\beta \to +0$. On the other hand for the penalty factor of our scheme, only when the recycling cavity is nearly the critical coupling ($r_{\mathrm{reso}} \simeq 0$), it would be $f(\beta) \simeq |J_0(\beta)|$.

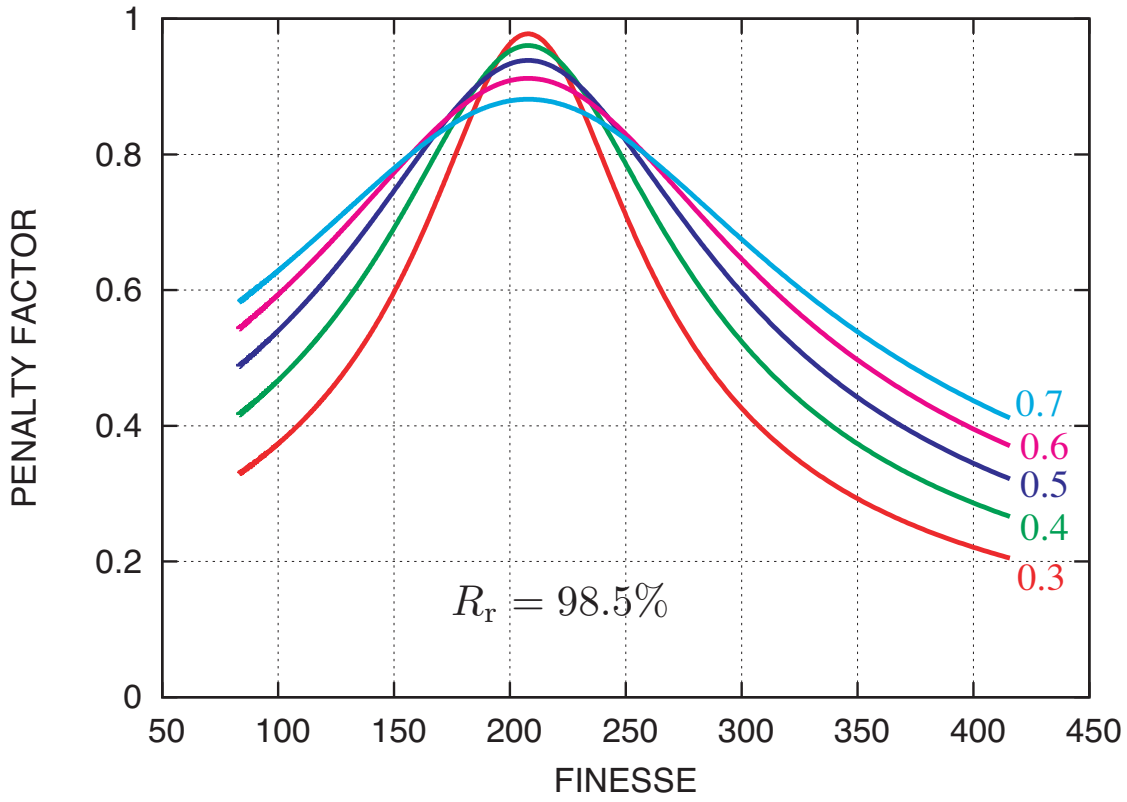

Figure 4.6 Penalty factor $f(\beta)$ of our scheme with respect to the finesse of the recycling cavity. The vertical axis represents $f(\beta)$, and the horizontal axis represents the finesse. The power reflectance of RM is fixed at $R_r = 98.5\%$. The number attaced to each curve is the modulation depth β.

Figure 4.6 shows penalty factor $f(\beta)$ of our scheme with respect to the finesse of the recycling cavity. The power reflectance of RM is fixed at $R_r = 98.5\%$, which is the nominal value of the RM used now. The number attaced to each curve is the modulation depth β. When $R_r = 98.5\%$, the finesse of $\mathcal{F} \simeq 208$ corresponds to the critical coupling condition, where $f(\beta)$ approches unity if β is small. On the other hand, the finesse is outside of that region, $f(\beta)$ gets larger when β increases.

For example, if $r_r = \sqrt{0.985}$, finesse 130 requires $r_c \simeq \sqrt{0.967}$. It corresponds to ${r_c}^{2/3} = 98.89\%$[1] (the averaged amplitude reflectance of EM1, EM2, and TM). Under the condition, $f(\beta)$ is plotted with respect to β in Figure 4.7. $f(\beta)$ gets the maximam at $\beta \simeq 0.75$ or 0.8. The red curve is the penalty factor of frontal modulation scheme (for comparison).

Even if $f = 1$ is achieved, Eq.(4.48) is $\sqrt{2}$ times worse than the ideal strain sensitivity in Eq.(3.59). This is because a part of photocurrent at $(\omega_g + \omega_m)$ is filtered out by the resonant circuits build in the photodetector, and that corresponds to that the

[1] Nominal value is about $99.x\%$.

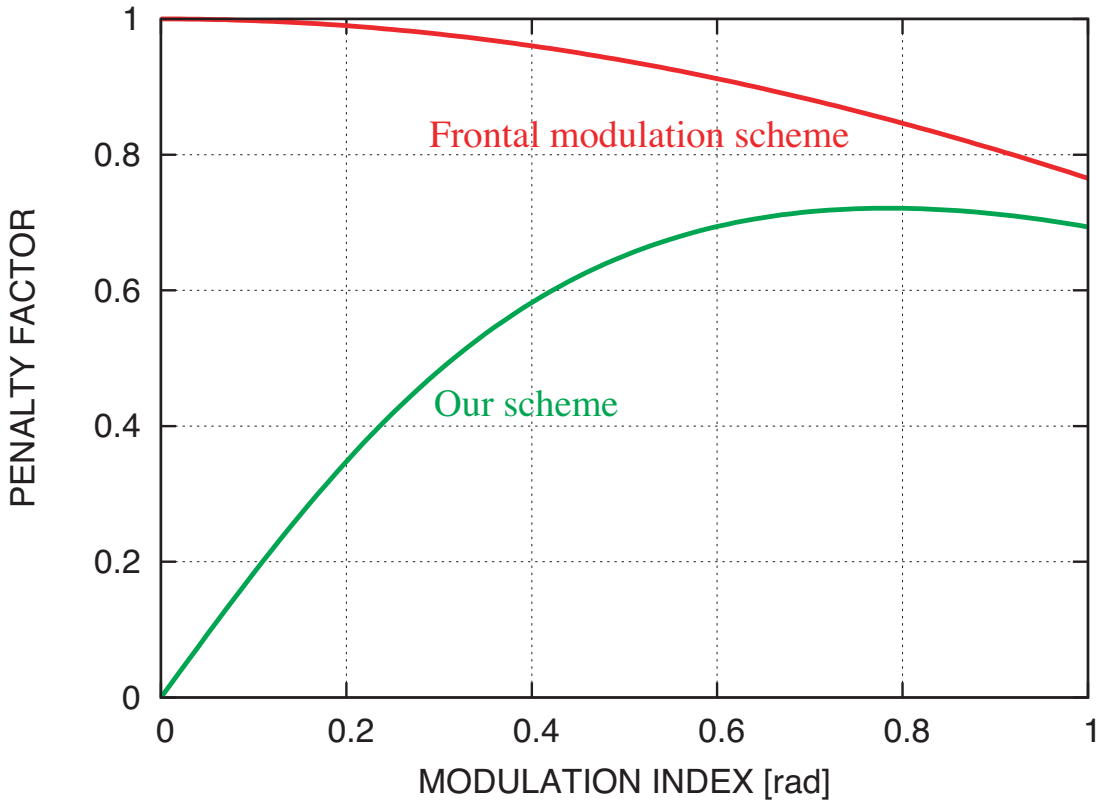

Figure 4.7 Comparison of penalty factors $f(\beta)$ between the frontal modulation scheme and our scheme. The horizontal axis represents $f(\beta)$, and the vertical axis represents the modulation depth β. For the calculation, the power reflectance of the RM is fixed at $R_{\mathrm{r}} = 98.5\%$ and the finesse of the recycling cavity is fixed at 130. Note that the frontal modulation scheme can not be used for the signal extraction of synchronous recycling interferometer.

Table 4.1 Parameters used for the illustrations in Figure 4.8

Index	Parameters	Values
$\bar{P}_{\mathrm{inc}}$	Intensity of the laser source	0.5 W
η	Quantum efficieny	1
$\nu_0 = c/\lambda_0$	Frequency of the laser souce	$c/(1064\,\mathrm{nm})$ Hz
$\nu_{\mathrm{FSR}} = c/(4L)$	Center frequency of the observation	100 MHz
r_{r}	Reflectance of the RM (amplitude)	$\sqrt{0.985}$
t_{r}	Transmittance of the RM (amplitude)	$\sqrt{1-{r_{\mathrm{r}}}^2}$
$r_{\mathrm{c}} \equiv r_1 r_2 r_{\mathrm{t}}$	Compound reflectance (amplitude)	$\sqrt{0.967}$
β	modulation depth	0.75 and 0.3
$1-({r_{\mathrm{BS}}}^2+{t_{\mathrm{BS}}}^2)$	Intensity loss at the BS	0
r_5	Reflectance of M1 or M2 (amplitude)	1

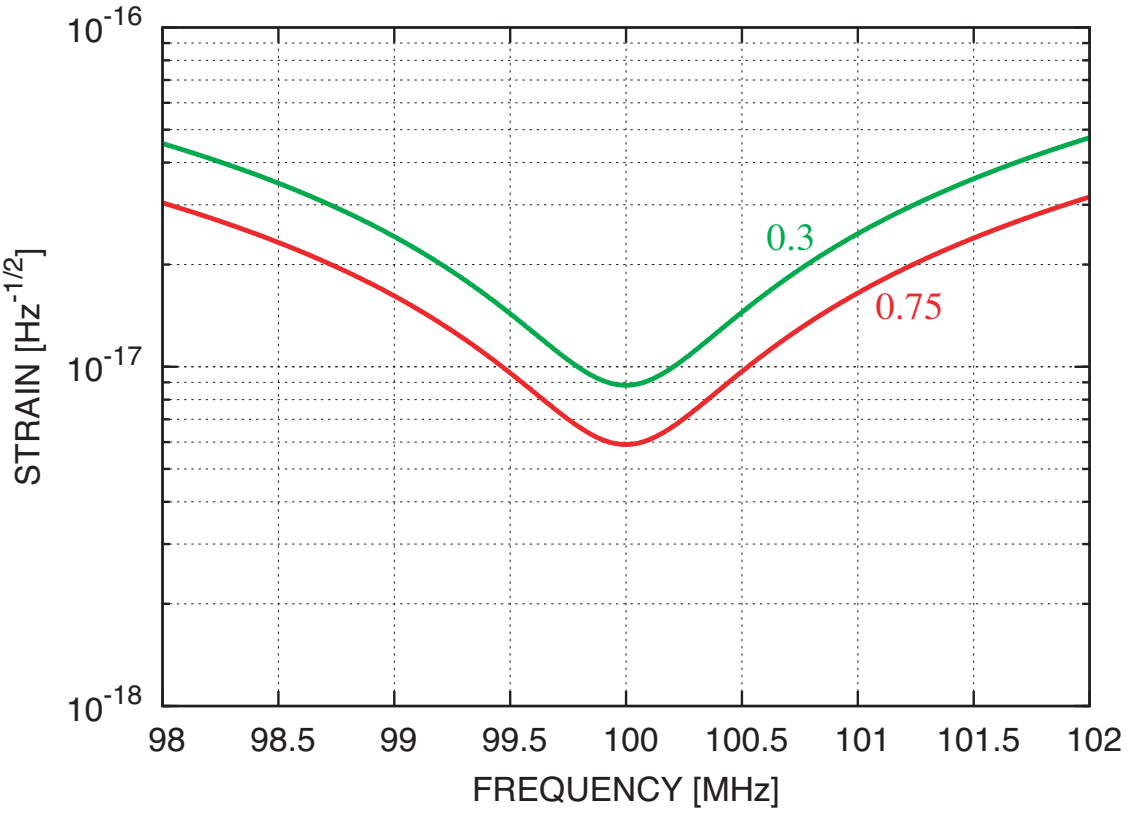

Figure 4.8 Calculation of the strain sensitivities for each modulation index β, which is attached to each curve. The interferometer has a resonance at 100 MHz, and a finesses of 130.

intensity of the incident light gets down to the half.

In the end, Figure 4.8 shows the possible strain sensitivities in the current experimental status. The vertical axis represents the strain sensitivity, and the horizontal axis represents the frequency of gravitational waves. Here assume that the inteferometer is tuned to have a resonant response to gravitational waves at 100 MHz. The parameters used in the calculation is shown in Table 4.1. If the modulation depth is 0.75, the possible strain sensitivity would be $h_{\rm sn} = 5.9 \times 10^{-18}\,{\rm strain}/\sqrt{\rm Hz}$. If the modulation depth is 0.3, the possible strain sensitvity is $h_{\rm sn} = 8.8 \times 10^{-18}\,{\rm strain}/\sqrt{\rm Hz}$. Note that the center frequency of the observation $\nu_{\rm FSR}$ is now decided from the measurements in the actual experiment. In addition, we could decide the center frequency with the absolute-length control [55, 56] (It will be included in the future works).

Chapter 5

Development of a detector for 100-MHz gravitational waves

5.1 Optical design of the gravitational-wave detector

We have developed a gravitational-wave detector that consists of two synchronous recycling interferometers. Figure 5.1 shows the optical design of the interferometric gravitational-wave detector. The two interferometers are hereafter referred to as IFO-1 and IFO-2, respectively. In Figure 5.1, the suffix attached to the name of each component indicates to which interferometer it belongs.

5.1.1 Overview of each interferometer

The two interferometers are constructed on a single optical table with size 2000 mm $\times$1200 mm. For each interferometer, the light source[1] is a neodymium-doped yttrium-aluminum-garnet (Nd:YAG) laser. The laser source emits a continuous infrared beam of wavelength 1064 nm and laser power 0.5 W. The quarter-wave plate (QWP) changes the polarization of the laser light from elliptic to linear; the half-wave plates (HWPs) rotate the polarization plane. The electro-optic phase modulator (EOM) is designed[2] to have a resonance at $f_{\mathrm{RF}} = 85.4\,\mathrm{MHz}$, and induces radio-frequency (RF) sidebands to the laser light. The modulation depth of the RF sidebands is about $\beta \simeq 0.38$ rad for each interferometer. A signal source[3] generates an 85.4-MHz sinusoidal signal, which is divided with a powersplitter, then the two signals are supplied to each interferometer. At each interferometer, the RF signal is again divided into two ways: one for the EOM and the other for a demodulator at

[1] InnoLight GmbH, Mephisto
[2] New Focus 4003
[3] Tektronix, AFG3102

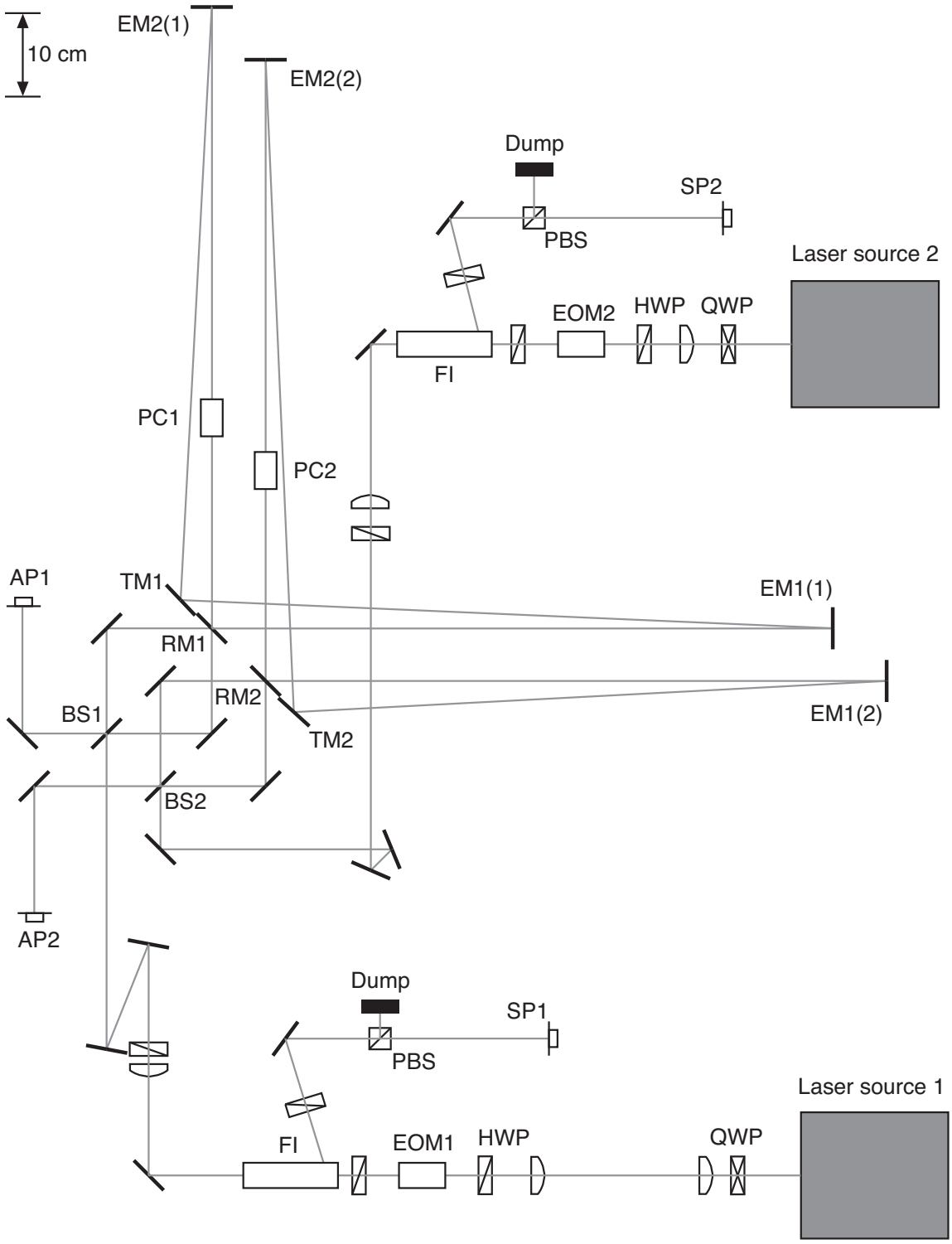

Figure 5.1 Optical design of the interferometric gravitational-wave detector, which consists of two interferometers: IFO-1 and IFO-2. The suffix attached to the name of each component shows to which interferometer it belongs.

the symmetric port (SP). The Faraday isolator (FI) protects the laser source from a backward light, then which is emitted to the symmetric port. At the symmetric port, the power of the light is reduced with a half-wave plate and a polarizing beamsplitter (PBS) so that the photodetector can accept the light without saturation.

The beamsplitter (BS) divides the laser light into two directions with almost the same intensity (nominal splitting ratio is 50%/50%). The recycling mirror (RM) is a partial reflector, which is designed[4] to have an power reflectance of (nominal) $98.5 \pm 0.5\%$. Each end mirror (EM1 or EM2) is a concave spherical mirror with radius of curvature of 1 m, while the transfer mirror (TM) is a flat mirror. The length between the RM and the EM1 (or EM2), which is referred to as the baseline length, is about $L = 75$ cm. The round-trip length of the recycling cavity is about 3 m (four times the baseline length, $4L$). Thus the interferometer has a maximum sensitivity to gravitational waves at $\nu_{\mathrm{FSR}} \equiv c/(4L) \simeq 100\,\mathrm{MHz}$.

The spacetime strain carried by gravitational waves will modulate the phase of the light resonant in the recycling cavity, and induce signal sidebands to the light at the modulation frequency. Then the signal sidebands are caught with a photodetector at the antisymmetric port (AP) or *dark port*. In order to calibrate the observed photocurrent to the corresponding amplitude of gravitational waves, we insert a Pockels cell (PC) in the recycling cavity, with which we can modulate the phase of the light at around 100 MHz to imitate the signal sidebands.

5.1.2 Spatial mode matching

For each interferometer, the laser source emits the light beam in a TEM00 spatial mode. On the other hand, the recycling cavity, as well as a usual Fabry-Perot cavity, has its own eigenmodes, in which a laser light can be stably resonant in the cavity. Thus one part of the incident light that matches one of the cavity eigenmodes is able to be resonant, while the other part is reflected at the entrance of the cavity then lost. In order to avoid such a loss, we set lenses to change the spatial mode of the laser so that it matches the cavity eigenmode.

Gaussian beam

Now assume that a laser beam is propagating in z-direction in a TEM00 mode (or Gaussian beam). Then we can characterize the beam mode with its complex radius of curvature $q(z)$ defined as follows: [57, 58]

$$\frac{1}{q(z)} \equiv \frac{1}{R(z)} - \mathrm{i}\frac{\lambda_0}{\pi w^2(z)}, \tag{5.1}$$

where $R(z)$ is the (physical) radius of curvature of the beam wavefront; λ_0 is the wavelength of the laser light; $w(z)$ is the spot size or the beam radius, where the laser

[4] Rocky Mountain Instrument Co.

power gets down to $1/e^2 \simeq 13.5\%$ of the laser power at the beam center. For the laser beam propagating in $+z$-direction, the sign of $R(z)$ is defined as follows: $R(z) < 0$ if $z < z_0$, and $R(z) > 0$ if $z_0 < z$, where z_0 is called beam waist. At the beam waist, the beam radius is minimized and the radius of curvature goes infinity, thus Eq.(5.1) is reduced to

$$\frac{1}{q_0} \equiv \frac{1}{q(z_0)} = -\mathrm{i}\frac{\lambda_0}{\pi w_0^2}, \tag{5.2}$$

where $w_0 \equiv w(z_0)$ is the smallest spot size, or beam waist radius. For a laser beam along z-direction, the parameter $q(z)$ changes as follows:

$$q(z) = q_0 + z - z_0. \tag{5.3}$$

The beam radius $w(z)$ and the radius of curvature $R(z)$ of the beam wavefront vary with respect to z as follows:

$$w(z) = w_0 \sqrt{1 + \frac{(z - z_0)^2}{{z_\mathrm{R}}^2}}, \tag{5.4}$$

$$R(z) = (z - z_0)\left[1 + \frac{{z_\mathrm{R}}^2}{(z - z_0)^2}\right], \tag{5.5}$$

where

$$z_\mathrm{R} \equiv \frac{\pi w_0^2}{\lambda_0} \tag{5.6}$$

is called the Rayleigh range [57]. When the beam passes a lens with a focal length of f at a position of z, then the parameter $q(z)$ changes as follows:

$$\frac{1}{q'(z)} = \frac{1}{q(z)} - \frac{1}{f}, \tag{5.7}$$

where the prime in the left-hand side indicates that the beam has a different TEM00 mode from $q(z)$ after it passes through the lens. The lens only changes the real part of $1/q(z)$; in other words, the lens changes the radius of curvature of the beam wavefront, but does not change the beam radius [see Eq.(5.1)].

Laser sources

For each laser source, Figure 5.2 shows the beam radii along two spatial orthogonal axes ($w_x(z)$ and $w_y(z)$ for horizontal and vertical, respectively) with respect to the distance z from the laser source. The upper graph shows the beam radius of the laser source in IFO-1. The lower graph shows the beam radius of the laser source in IFO-2. The filled marks represent the measurements, and the curves represent the fittings. From Eq.(5.4), each measurement is fitted to $w(z)$ via w_0 and z_0 (shown in Table 5.1). For each laser source, the measurements of the beam radius is different in x-direction and y-direction. Note that the position $z = 0$ represents the front wall of the laser head for each measurement.

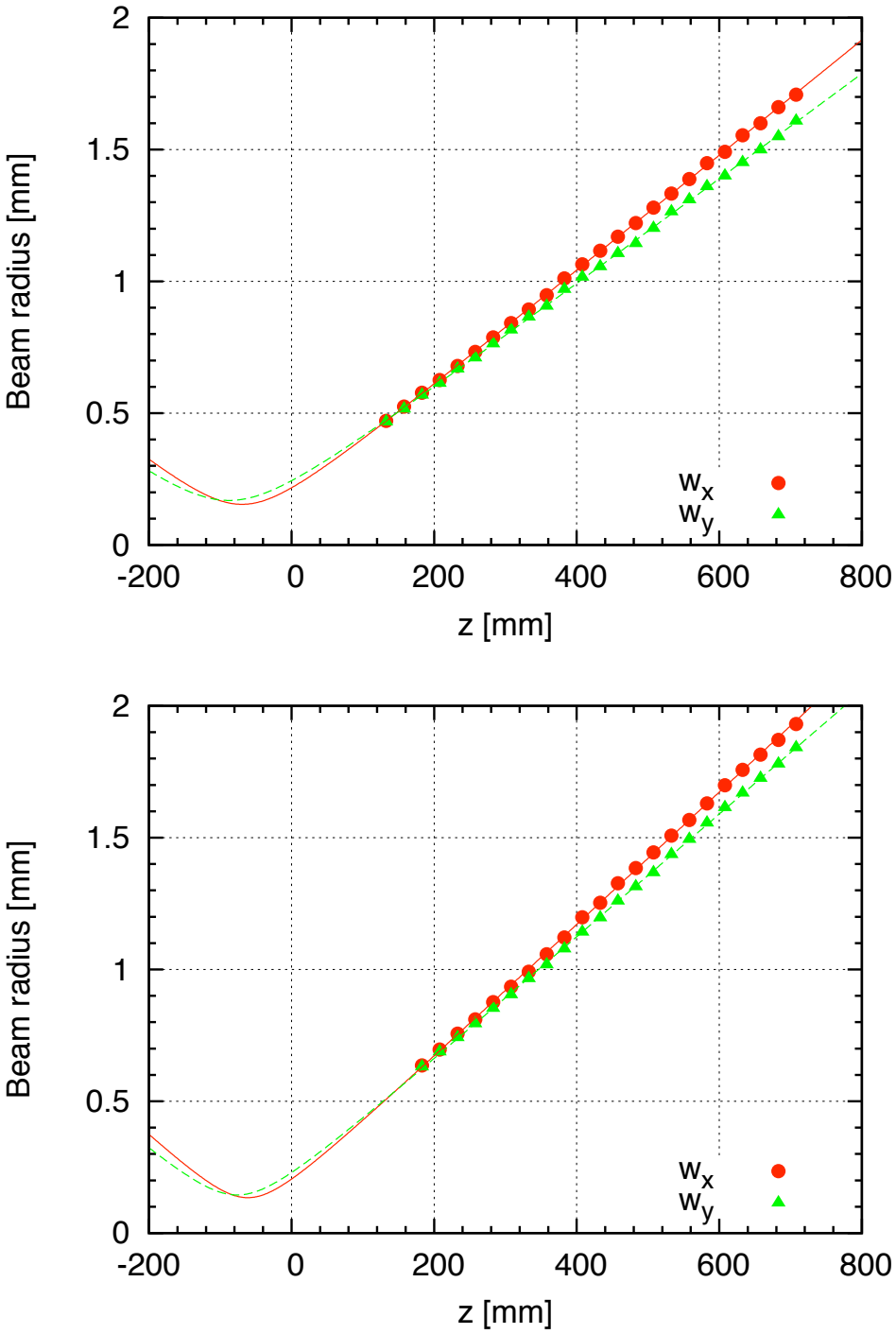

Figure 5.2 Beam radii of the laser sources: the upper for Laser source 1 and the lower for Laser source 2 (see Figure 5.1). For each laser source, red filled circles represent the measurements of $w_x(z)$, to which a solid red curve is fitted with Eq.(5.4), and solid green triangles represent the measurements of $w_y(z)$, to which a dashed green curve is also fitted with Eq.(5.4). For each measurement, the front wall of the laser head is at $z = 0$.

Table 5.1 Beam waists and beam radii of the laser sources

Laser source 1	x-direction (horizontal)	y-direction (vertical)
Beam waist radius w_0 (mm)	0.154190	0.168907
Beam waist position z_0 (mm)	−69.4837	−87.7472
Laser source 2	x-direction (horizontal)	y-direction (vertical)
Beam waist radius w_0 (mm)	0.134303	0.144666
Beam waist position z_0 (mm)	−61.3151	−76.2250

Table 5.2 Beam waist radii of the basic mode of the recycling cavity (design)

	w_{x0} (horizontal)	w_{y0} (vertical)
Path-1 (mm)	0.38625	0.38646
Path-2 (mm)	0.38556	0.38577

Geometric design of the recycling cavity

The geometric design of the recycling cavity is shown in Figure 5.3. The distance from the RM to the EM1 is $L_1 = 0.738$ m. The distance from the RM to the EM2 is also L_1. The path from the EM2 to the EM1 via the RM is hereafter called Path-1. Also, the path from the EM1 to the EM2 via the TM is hereafter called Path-2. The geometry is designed so that the laser beam is bent by 90° at the RM and the TM, because these mirrors are designed to have the highest reflectance for the incident angle of 45°. The distance from EM1 to EM2 via TM is $2L_2 = 2L_1 \cos 2\theta$. The clearance between the RM and the TM is 0.05 m, then the laser beam is bent by $2\theta \simeq 2.746°$ at the EMs. In order to avoid the Sagnac effect, we reduce the effective area enclosed by the laser beam by crossing the optical path [59]. In this case the area is $L_1^2 \sin^2 2\theta \simeq 12.5$ cm^2. The round-trip length is $2(L_1 + L_2) \simeq 2.95$ m, which corresponds to a resonant frequency of $\nu_{\rm FSR} \simeq 101.6$ MHz; this resonant frequency is determined to avoid known electromagnetic noises[5].

The beam waist radii of the basic mode (TEM00 mode) is calculated from Eqs.(C.12) and (C.13) for Path-1 and Path-2, respectively. They are shown in Table 5.2. The beam waist radii of the basic mode differs in x-direction (horizontal) and y-direction (vertical). Thus the radius of curvature R of each end mirror in Eqs.(C.12) and (C.13) is replaced by $R_x = R\cos\theta$ or $R_y = R/\cos\theta$ with respect to the directions (for example, see Ref. [60]). As a result, the beam waist radius of the

[5] We prepare a simple antenna with a one-turn coil to measure electromagnetic noises at around 100 MHz, $f_{\rm RF}$ and $f_{\rm demod}$. Today the frequency bandwidth at around 100 MHz is occupied by television broadcasts, and the bandwidth at around $f_{\rm RF}$ is occupied by FM radio (in Mitaka, Japan).

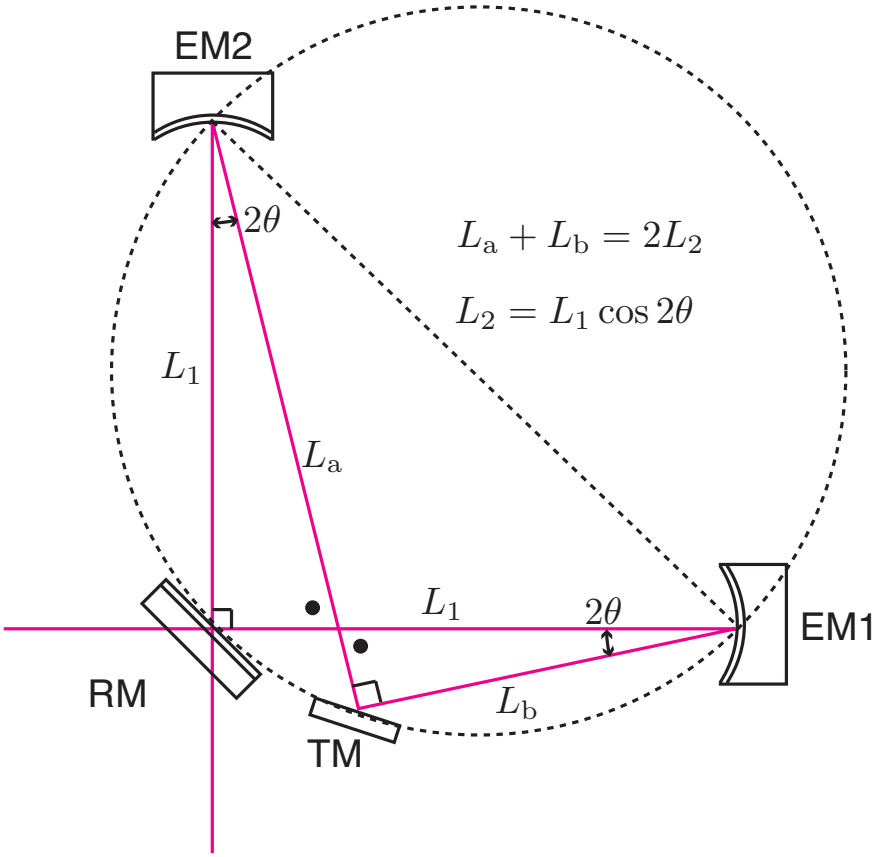

Figure 5.3 Design of the recycling cavity. The distance from the RM to the EM1 is $L_1 = 0.738$ m. The distance from the RM to the EM2 is also L_1. The clearance between the RM and the TM is 0.05 m. The distance from EM1 to EM2 via TM is $2L_2 = 2L_1 \cos 2\theta$. The laser beam is bent by 90° at the RM and the TM, and is bent by $2\theta \simeq 2.746°$ at the EMs. In order to avoid the Sagnac effect, the area enclosed by the laser beam is nearly zero by crossing the optical path. The round-trip length is $2(L_1 + L_2) \simeq 2.95$ m, which corresponds to $\nu_{\rm FSR} \simeq 101.6$ MHz.

basic mode is about 0.38 mm. Note that the beam waist of Path-1 is at the recycling mirror.

Mode matching

As shown in Figure 5.1, lenses are set so that the laser beam matches the cavity basic eigenmode. For each interferometer, Figure 5.4 shows the calculations of the radii of the laser beam with respect to the distance z from the laser source. The upper graph is for IFO-1, and the lower graph is for IFO-2. For each graph, the solid red curve represents the beam radius of x-direction $w_x(z)$, and the dashed green curve represents the beam radius of y-direction $w_y(z)$. The dash-dotted blue curve represents a beam mode with a waist radius of 0.385 mm, which corresponds to the basic mode of the recycling cavity (see Table 5.2). For IFO-1, the sets of the position

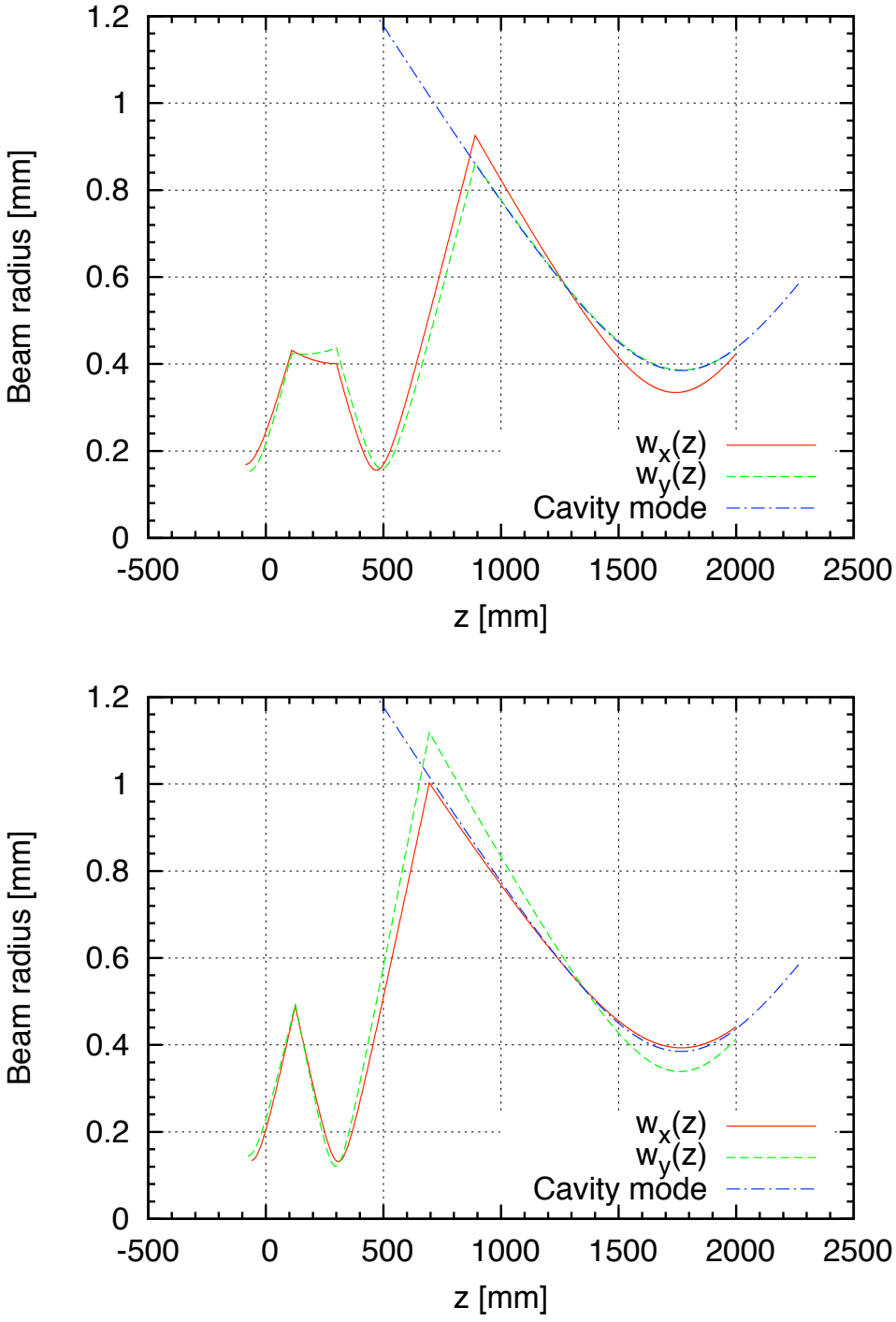

Figure 5.4 Variation of the beam radii in the interferometers: the upper for IFO-1 and the lower for IFO-2. For each interferometer, solid red curve represents the calculation of $w_x(z)$, dashed green curve represents the calculation of $w_y(z)$, and dash-doted blue curve represents the beam radius of the basic eigenmode of the recycling cavity.

z and focal length f of a lens for the calculation are [in mm]: $(z, f) = (110, 200)$, $(300, 200)$, and $(890, 300)$. For IFO-2, they are $(z, f) = (125, 100)$ and $(695, 300)$. The lenses are set in the interferometers based on these parameters.

Moreover, those lenses change the beam size so that the beam can pass through the Faraday isolator and EOM, which have small apertures (diameters of 3 mm and 2 mm, respectively). At each component, the laser beam is tuned to have a radius less than 1/3 of the aperture radius of the component. An aperture with radius of $\pi w(z)/2$ will pass $\sim 99\%$ of the TEM00 beam power. If the aperture radius is $\sim 2.3w(z)$, the aperture diffraction effect will be well suppressed (for example, see Ref. [57]).

5.2 Interferometer control system

For each interferometer, there is only one degree of freedom to be controlled: the relative phase fluctuation $\delta\Phi$ between the length of the recycling cavity and the frequency of the laser light. In order that the laser light is stably resonant in the recycling cavity, the relative phase fluctuation or error must be suppressed. Due to seismic noise or acoustic noise, the low-frequency components of the fluctuation is significant, and thus we suppress them by a feedback control based on the Pound-Drever-Hall technique [53]. On the other hand, the Sagnac part protects the antisymmetric port from length fluctuations in low frequency without controlling.

At the symmetric port of each interferometer, a photodetector with a resonant frequency of $f_{\rm RF} = 85.4$ MHz receives the light reflected from the interferometer. Then the photocurrent at around $f_{\rm RF}$ is demodulated by a local oscillator at $f_{\rm RF}$ into the baseband signal. The relative phase fluctuation or *error* causes the I-phase signal, which is proportional to the error, so it is called the error signal. Then the servo filters respond to the error signal and output feedback signals. The feedback signals are applied to the frequency actuators attached to the laser source. The actuators change the frequency of the laser light such that the relative phase error $\delta\Phi$ is suppressed; in other words, the laser frequency is stabilized with respect to the cavity length.

Figure 5.5 shows the block diagram of the feedback control loop of the laser-frequency stabilization. The open-loop transfer function of this control system is written as

$$G = -HF_1(F_{\rm pzt}A_{\rm pzt} + F_{\rm thr}A_{\rm thr}) \tag{5.8}$$

$$= G_{\rm pzt} + G_{\rm thr}, \tag{5.9}$$

$$G_{\rm pzt} \equiv -HF_1F_{\rm pzt}A_{\rm pzt}, \tag{5.10}$$

$$G_{\rm thr} \equiv -HF_1F_{\rm thr}A_{\rm thr}, \tag{5.11}$$

where H represents a response function of the interferometer to the (relative) laser-frequency fluctuation $\delta\nu$; $A_{\rm pzt}$ and $A_{\rm thr}$ represent laser-frequency actuators: a piezo actuator and a thermal actuator, respectively; F_1, $F_{\rm pzt}$, and $F_{\rm thr}$ represent servo fil-

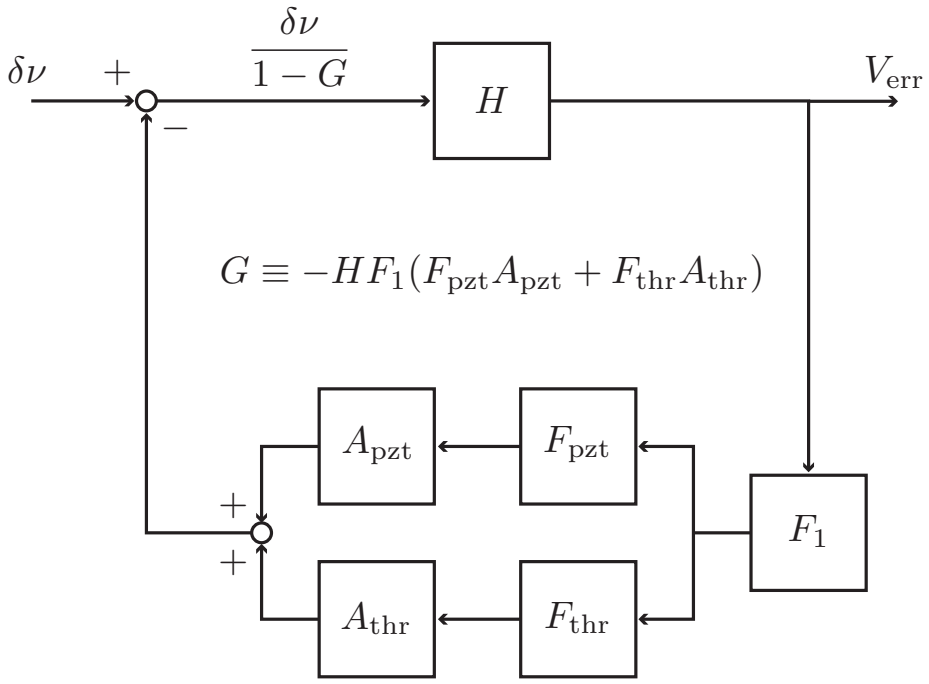

Figure 5.5 Block diagram of laser-frequency stabilization. H represents a response function of the recycling cavity to the relative fluctuation $\delta\nu$ between the laser frequency and the cavity length. $A_{\rm pzt}$ and $A_{\rm thr}$ represent laser-frequency actuators: a piezo actuator and a thermal actuator, respectively. F_1, $F_{\rm pzt}$, and $F_{\rm thr}$ represent servo filters' frequency response functions. The raw fluctuation $\delta\nu$ is suppressed to $\delta\nu/(1-G)$ in the control bandwidth, where G is open-loop transfer function. The residual fluctuation $\delta\nu/(1-G)$ causes the error signal $V_{\rm err} = H\,\delta\nu/(1-G)$.

ters' frequency response functions. The piezo actuator has a fast response (~ 100 kHz) to the fluctuation but has a small dynamic range (~ 1 MHz/V). The thermal actuator has a large dynamic range (~ 3 GHz) but has a slow response (~ 1 Hz). The raw fluctuation $\delta\nu$ is suppressed to $\delta\nu/(1-G)$ in the control bandwidth. Note that the residual fluctuation $\delta\nu/(1-G)$ again causes the error signal $V_{\rm err} = H\,\delta\nu/(1-G)$.

5.2.1 Open-loop transfer functions

For each interferometer, the open-loop transfer function is measured as shown in Figure 5.6. The upper graph is the Bode diagram of $G(f)$ for IFO-1, and the lower graph is for IFO-2. The red filled circles represent the measurements. The solid blue lines represent $G(f)$ estimated from Eqs.(5.12), (5.16), (5.18), and (5.19). For IFO-1, the unity-gain frequency is at ~ 8.2 kHz, where the phase margin is $\sim 64°$. For IFO-2, the unity-gain frequency is at ~ 5.97 kHz, where the phase margin is $\sim 65°$. For each graph, an inconsistency appears above 40 kHz between the measurements and the estimation. The reason would be that the estimation of the response function of

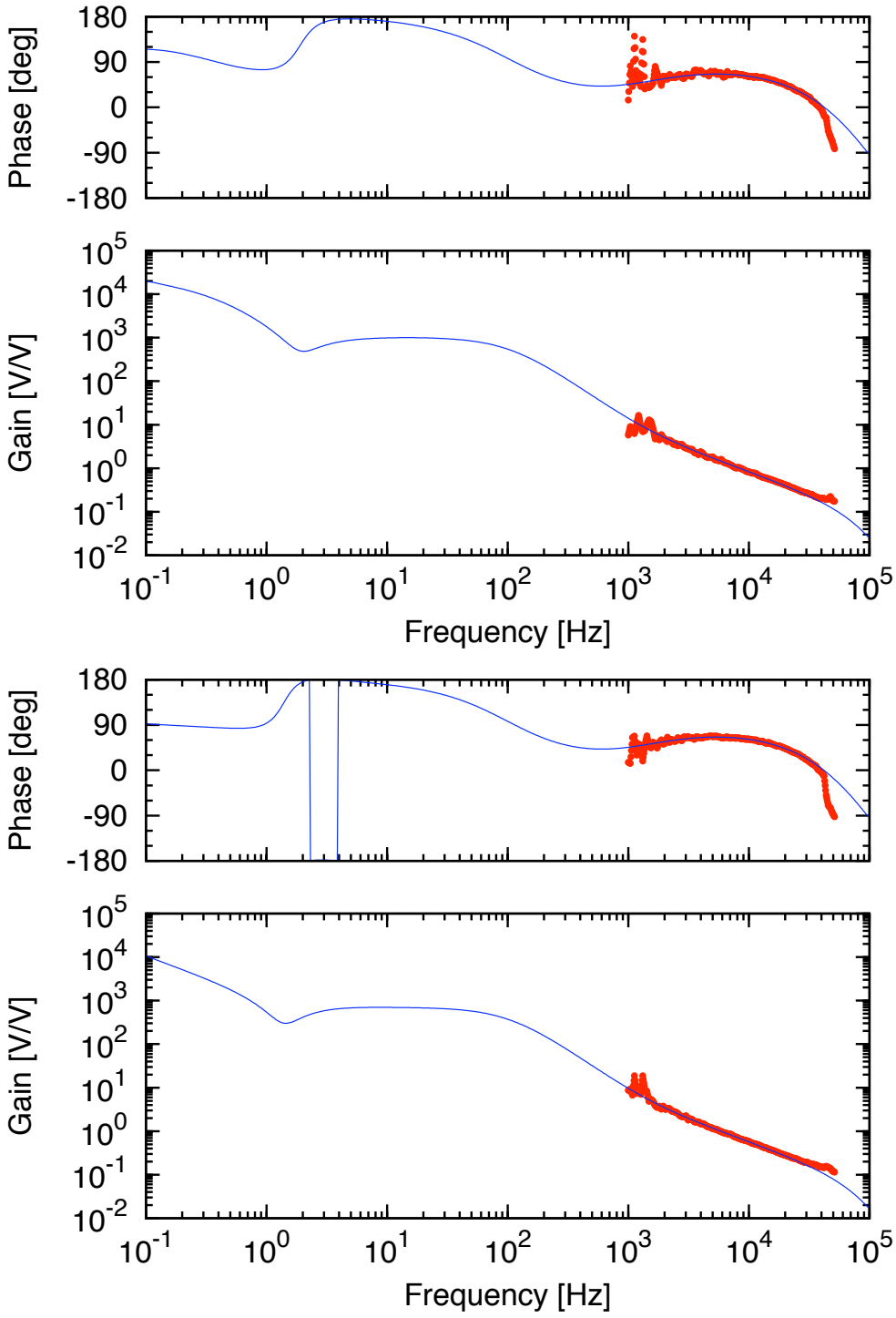

Figure 5.6 *Upper*: Bode diagram for the open-loop transfer function of IFO-1. Measurements (red filled circles) and fitting curves (blue solid) are shown. The unity-gain frequency is at ~ 8.2 kHz, where the phase margin is $\sim 64°$. *Lower*: Bode diagram for the open-loop transfer function of IFO-2. Measurements (red filled circles) and fitting curves (blue solid) are shown. The unity-gain frequency is at ~ 5.97 kHz, where the phase margin is $\sim 65°$.

the piezo actuator [see Eq.(5.16)] is failed in the high frequency region.

5.2.2 Interferometer response to the low-frequency fluctuations

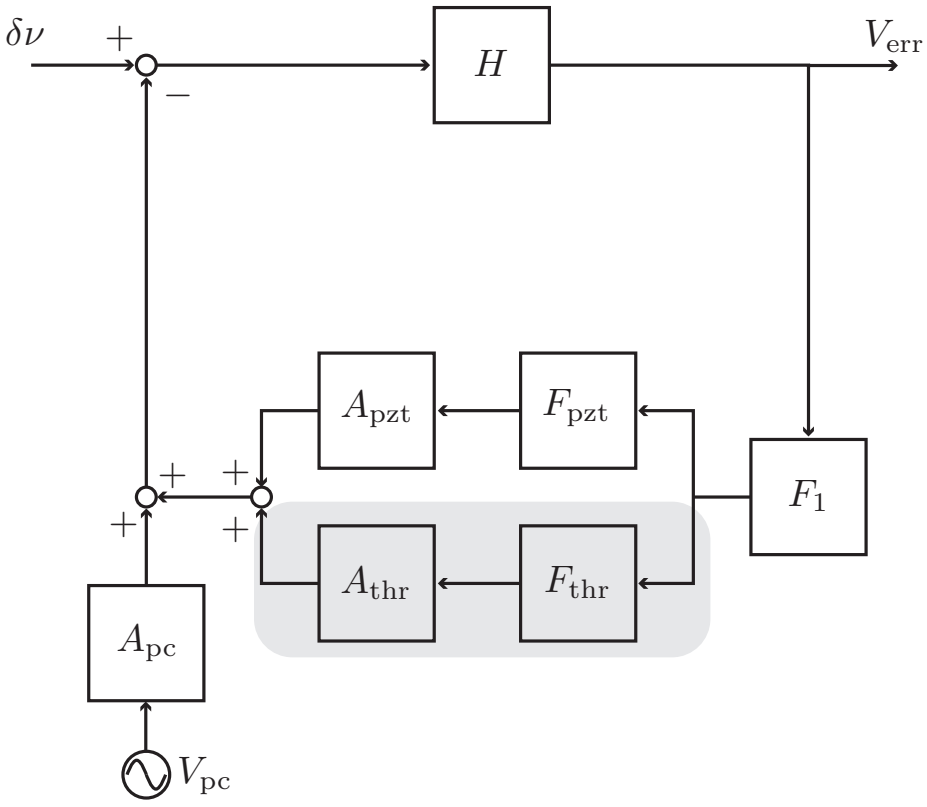

Figure 5.7 Block diagram for the estimation of interferometer response H. $A_{\rm pc}$ represents a modulation efficiency of the Pockels cell in the recycling cavity. The thermal servo (shaded region) does not contribute to the control at $f_{\rm cal}$ because the frequency is much higher than the control bandwidth of the thermal servo.

For each interferometer, the response function $H(f)$ to the low-frequency fluctuation $\delta\nu$ is estimated from the relation

$$H(f_{\rm cal}) = -\frac{1 - G(f_{\rm cal})}{A_{\rm pc}(f_{\rm cal})} \frac{V_{\rm err}(f_{\rm cal})}{V_{\rm pc}(f_{\rm cal})}, \tag{5.12}$$

where $A_{\rm pc}$ is the modulation efficiency of the Pockels cell in the cavity (see Figure 5.1); $V_{\rm pc}$ is an applied voltage to the Pockels cell; $f_{\rm cal}$ is the frequency of the applied voltage (see Figure 5.7). First, the sinusoidal calibration peak $V_{\rm pc}$ at $f_{\rm cal} = 3.16$ kHz is applied to the Pockels cell. The efficiency of the cell is $A_{\rm pc} \sim 8.5 \times 10^{-3}$ rad/V , which corresponds to $A_{\rm pc} \sim 0.135$ MHz/V, because the depth of the phase modulation

$\delta\phi$ is related to the frequency fluctuation $\delta\nu$ in the following form:

$$\frac{\delta\nu}{\nu_{\rm FSR}} = \frac{\delta\phi}{2\pi}. \tag{5.13}$$

From the measured ratio $V_{\rm err}/V_{\rm pc}$ at $f_{\rm cal}$, the response function H is estimated: 8.45×10^{-5} V/Hz for IFO-1, and 1.62×10^{-5} V/Hz for IFO-2. Because now the recycling cavity has such a low finesse that the FWHM (full width at half maximum) of the cavity spectrum is greater than 100 kHz, the response function H is considered to be a constant for the low-frequency fluctuation.

For later use, let us derive the response function H in the unit of m/V. The frequency fluctuation is related to the fluctuation of the cavity half-length $L_+ \equiv 2L$. in the following form:

$$\frac{\delta\nu}{\nu_0} = \frac{\delta L_+}{L_+}, \tag{5.14}$$

where ν_0 is the frequency of the laser light source, and δL_+ is the fluctuation of L_+. Note that the round-trip length of the recycling cavity is $4L$. Thus the response function H is estimated: 1.59×10^{10} V/m for IFO-1, and 3.05×10^{9} V/m for IFO-2.

5.2.3 Laser-frequency actuators

Piezo actuator efficiency

The higher frequency fluctuation is suppressed with the piezo servo. For each laser source, the efficiency of the piezo actuator at the (previously introduced) frequency $f_{\rm cal}$ is estimated from the following relation:

$$G(f_{\rm cal}) \simeq G_{\rm pzt}(f_{\rm cal}), \tag{5.15}$$

where the thermal servo does not contribute to the feedback control at $f_{\rm cal}$ because the frequency is much higher than the response bandwidth of the thermal actuator. The response function of the piezo actuator is estimated to be

$$A_{\rm pzt} = \frac{a_0^{\rm pzt}}{1 + {\rm i}f/100\ {\rm kHz}}, \tag{5.16}$$

where $a_0^{\rm pzt}$, which corresponds to piezo actuator efficiency at 0 Hz, is estimated to be 1.4 MHz/V for IFO-1, and 2.1 MHz/V for IFO-2. The nominal efficiency is about 1 MHz, which is consistent with the estimations. The cut off frequency of 100 kHz is nominal, and thus the correct order of the pole function is not clear. In fact, the estimation of the open-loop transfer function is failed in the high frequency region (see Figure 5.6).

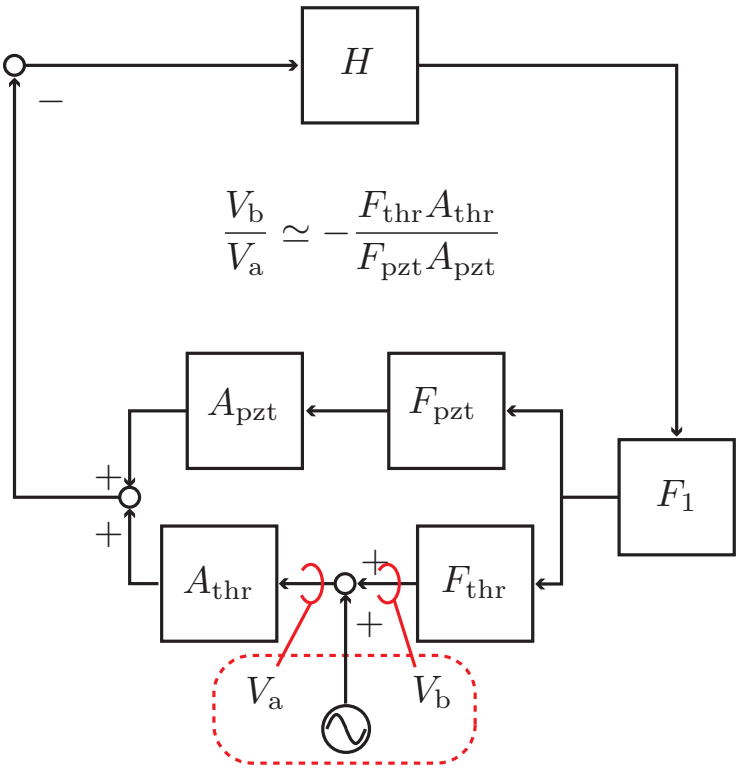

Figure 5.8 Measuring the response ratio of the thermal servo to the piezo servo.

Thermal actuator efficiency

The thermal actuator has a large dynamic range but slow response. The lower-frequency fluctuation is suppressed with the thermal servo. At the "crossover frequency", the thermal servo passes the feedback control to the piezo servo; in other words, the gain of the thermal servo equals the gain of the piezo servo at the frequency.

For each laser source, the efficiency of the thermal actuator at around the crossover frequency is estimated from measuring the ratio (see Figure 5.8)

$$\frac{G_{thr}}{1 - G_{pzt}} \simeq -\frac{G_{thr}}{G_{pzt}}. \tag{5.17}$$

The approximation in the above relation is valid at the low frequency region, where the gain of the piezo servo satisfies $|G_{pzt}| \gg 1$. The ratio is measured and shown in Figure 5.9. The upper graph is the Bode diagram of the ratio for IFO-1, and the lower graph is for IFO-2. For each graph, the red filled circles represent the measurement, and the solid blue lines represent the fittings at around the crossover frequency, where

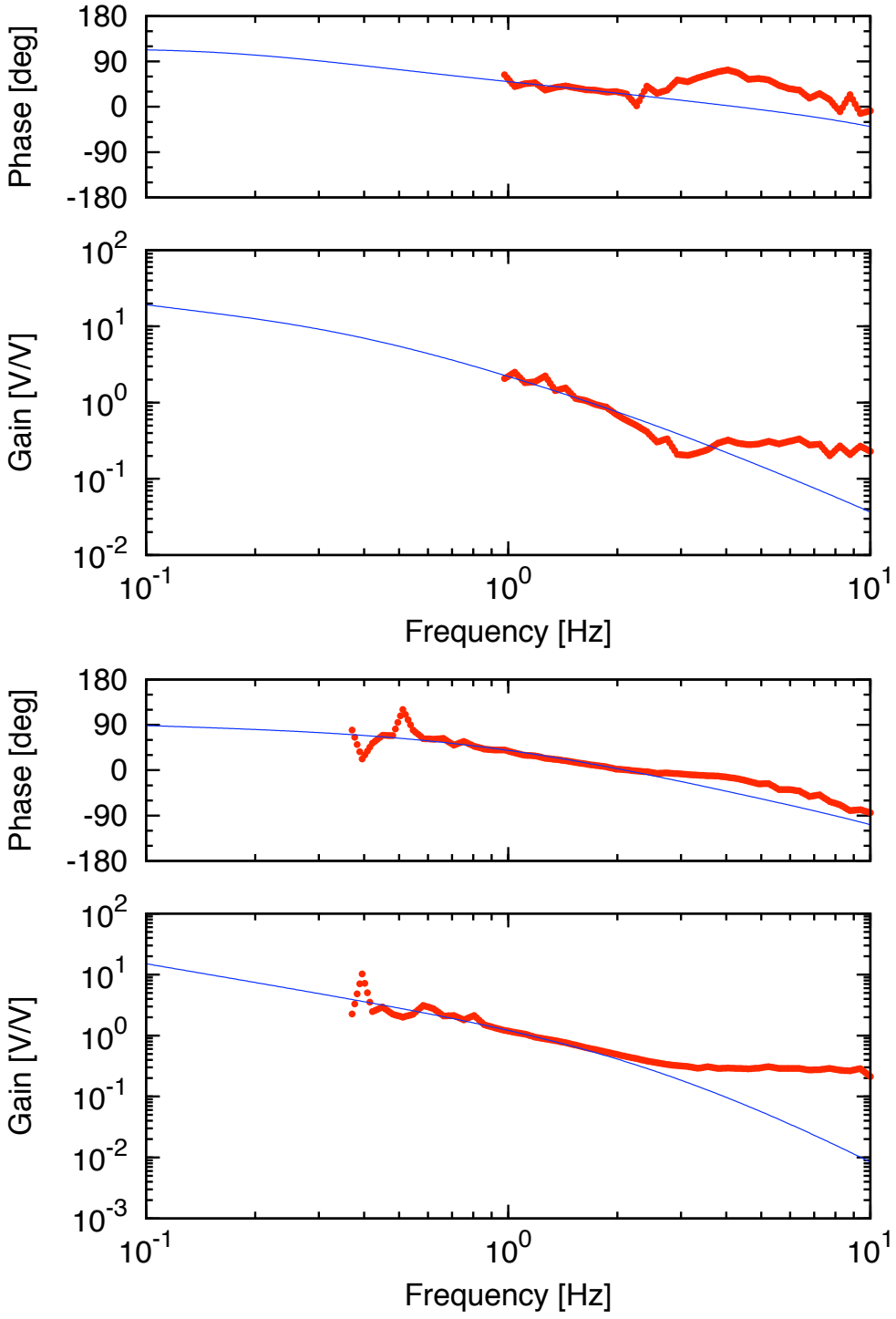

Figure 5.9 Bode diagrams for the relative response of the thermal servo to the piezo servo: $-F_{\rm thr}A_{\rm thr}/(F_{\rm pzt}A_{\rm pzt})$. Measured data (red filled circles) and fitting curves (blue solid) are shown. *Upper*: IFO-1. The crossover frequency is at $\sim$ 1.7 Hz, where the phase margin is $\sim 33^\circ$. *Lower*: IFO-2. The crossover frequency is at $\sim$ 1.14 Hz, where the phase margin is $\sim 28^\circ$.

the gain of the ratio is unity. The fitting results are:

$$A_{\mathrm{thr}(1)} = -3\ \mathrm{GHz}\ \frac{1}{1+\mathrm{i}f/0.22}\cdot\frac{1}{1+\mathrm{i}f/0.46-(f/1.07)^2} \tag{5.18a}$$

$$A_{\mathrm{thr}(2)} = -6.1\ \mathrm{GHz}\ \frac{1}{1+\mathrm{i}f/0.08}\cdot\frac{1}{1+\mathrm{i}f/0.63-(f/1.3)^2}\cdot\frac{1}{1+\mathrm{i}f/4} \tag{5.18b}$$

for IFO-1 and IFO-2, respectively. For IFO-1, the crossover frequency is at ~ 1.7 Hz, where the phase margin is $\sim 33°$. For IFO-2, the crossover frequency is at ~ 1.14 Hz, where the phase margin is $\sim 28°$. If the phase margin vanishes, no feedback controls work at the frequency. For the fast acquisition and stable lock of the feedback loop, the phase margin should range from about 30° to 60°. Those requirements are (almost) satisfied.

For each graph, the inconsistency appears above 2 Hz between the measurements and the estimation, but the thermal servo does not contribute to the open-loop transfer function in the frequency range. The estimation of the actuator efficiency at 0 Hz is also ambiguity. The nominal efficiency is about -3 GHz/V, which is consistent with the estimation for IFO-1, but two times smaller than the estimation for IFO-2.

5.2.4 Servo filters

For IFO-1, the Bode diagrams of the servo filters F_1, F_{pzt}, and F_{thr} is shown in Figures 5.10, 5.11, and 5.12, respectively. For IFO-2, the Bode diagrams of the servo filters F_1, F_{pzt}, and F_{thr} is shown in Figures 5.13, 5.14, and 5.15, respectively. For each figure, red filled circles represent the measurements, and solid blue curves represent the fittings with the following functions:

$$F_1(f) = g_1\cdot\left(\frac{1}{1+\mathrm{i}f/f_1}\right)^2\cdot\frac{1+\mathrm{i}f/f_{2\mathrm{L}}}{1+\mathrm{i}f/f_{2\mathrm{H}}} \tag{5.19a}$$

$$F_{\mathrm{pzt}}(f) = g_2\cdot\frac{1}{1+\mathrm{i}f/(Q_3 f_3)-(f/f_3)^2} \tag{5.19b}$$

$$F_{\mathrm{thr}}(f) = g_3\cdot\frac{1}{1+\mathrm{i}f/(Q_4 f_4)-(f/f_4)^2}\cdot\frac{1+\mathrm{i}f/f_{5\mathrm{L}}}{1+\mathrm{i}f/f_{5\mathrm{H}}}\cdot\frac{1+\mathrm{i}f/f_{6\mathrm{H}}}{1+\mathrm{i}f/f_{6\mathrm{L}}}, \tag{5.19c}$$

where the fitting parameters are shown in Table 5.3.

The filter F_1 compensates the phase retardation of the open-loop transfer function at the unity gain frequency. The filter F_{thr} compensates the phase retardation of the thermal servo relative to the piezo servo at the crossover frequency.

5.2.5 Displacement noises

For each interferometer, the residual fluctuation under the stabilization control is estimated from

$$\frac{\delta L_+}{1-G} = \frac{V_{\mathrm{err}}}{H}, \tag{5.20}$$

Table 5.3 Parameters for servo filters

	IFO-1	IFO-2
g_1	1.71488	3.45784
f_1	106.10 Hz	106.10 Hz
f_{2L}	1.383 kHz	1.383 kHz
f_{2H}	72.048 kHz	72.048 kHz
g_2	4.98303	5.97626
f_3	107.495 kHz	106.420 kHz
Q_3	0.660492	0.649667
g_3	−0.33333	−0.33333
f_4	20.2829 Hz	19.8218 Hz
Q_4	0.703407	0.706826
f_{5L}	1.06508 Hz	1.06323 Hz
f_{5H}	106.709 Hz	106.309 Hz
f_{6L}	9.90741 mHz	9.5176 mHz
f_{6H}	86.1823 mHz	83.0897 mHz

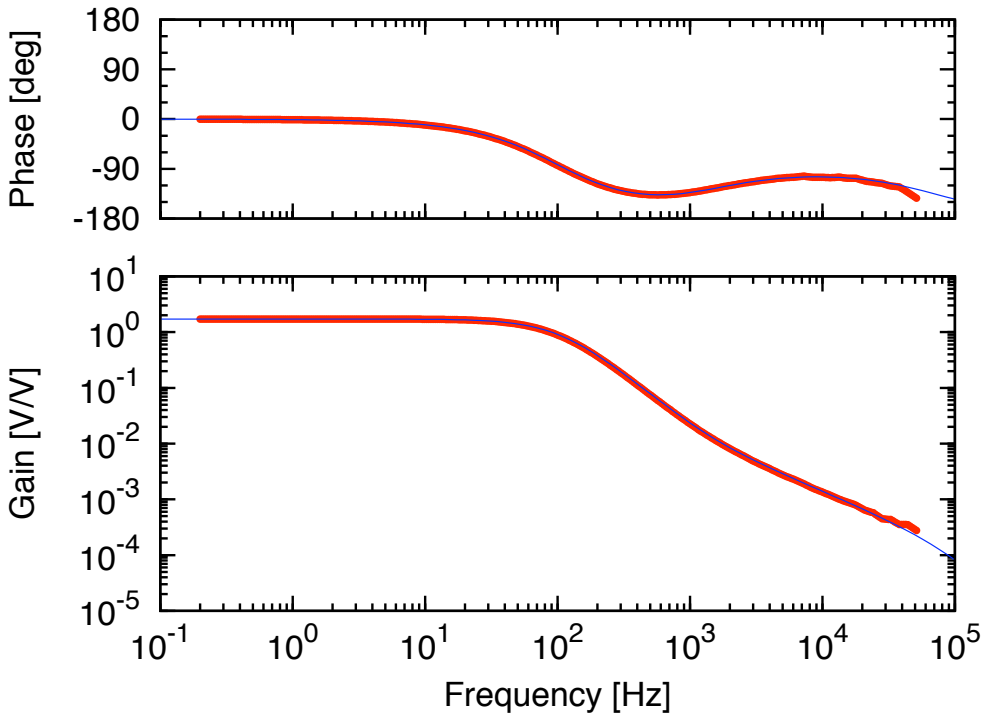

Figure 5.10 Bode diagram for the filter F_1 of IFO-1. Measured data (red filled circles) and fitting curves (blue solid) are shown.

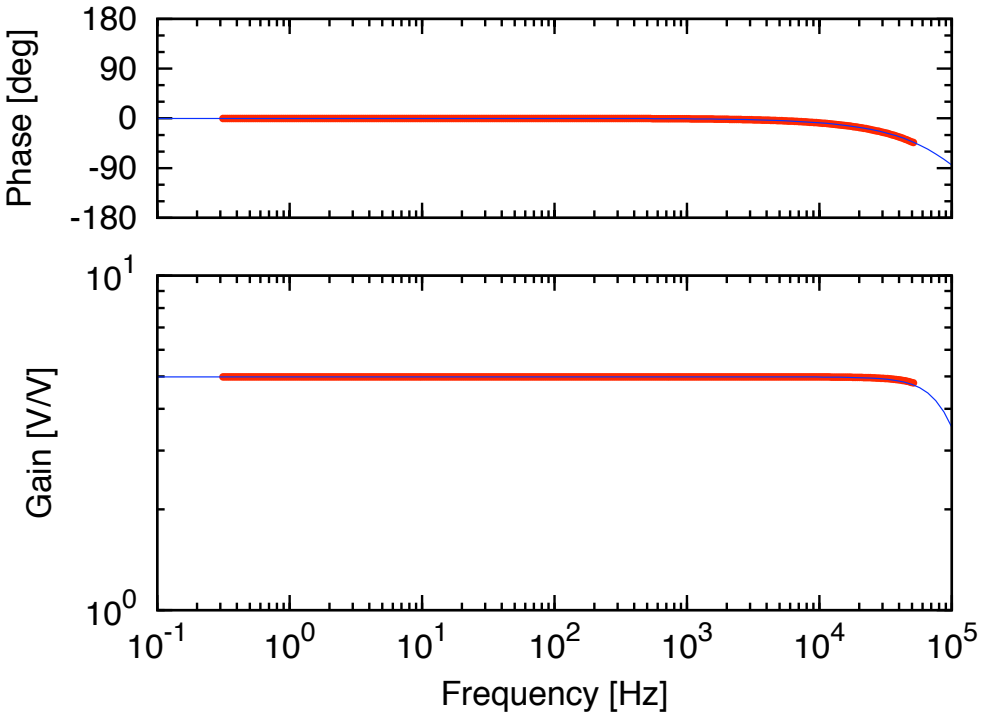

Figure 5.11 Bode diagram for the filter F_{pzt} of IFO-1. Measured data (red filled circles) and fitting curves (blue solid) are shown.

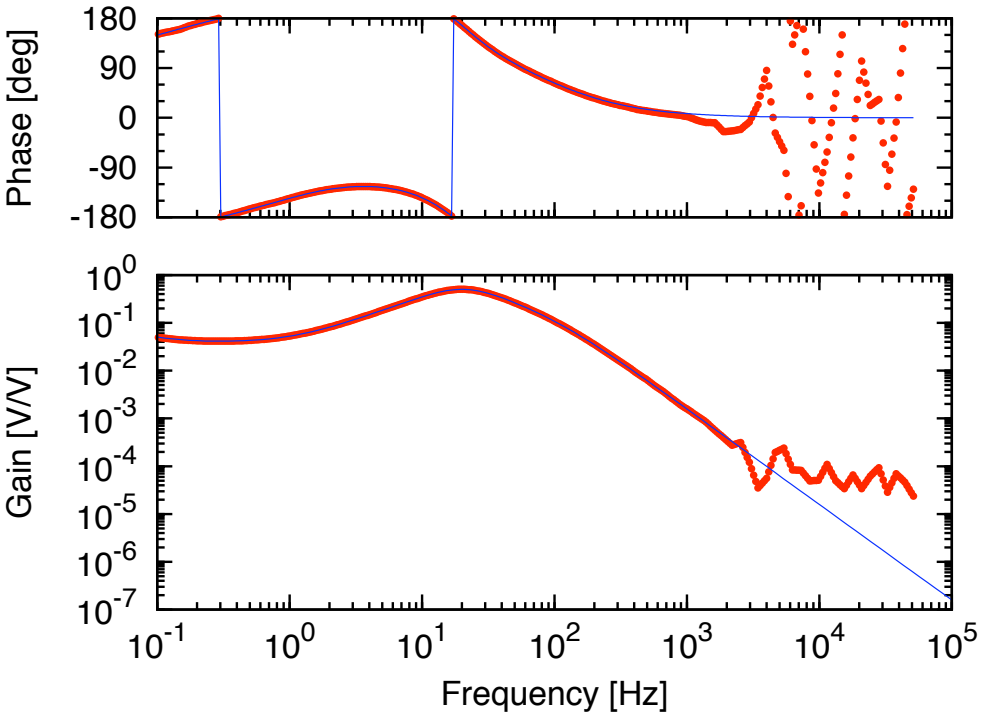

Figure 5.12 Bode diagram for the filter F_{thr} of IFO-1. Measured data (red filled circles) and fitting curves (blue solid) are shown.

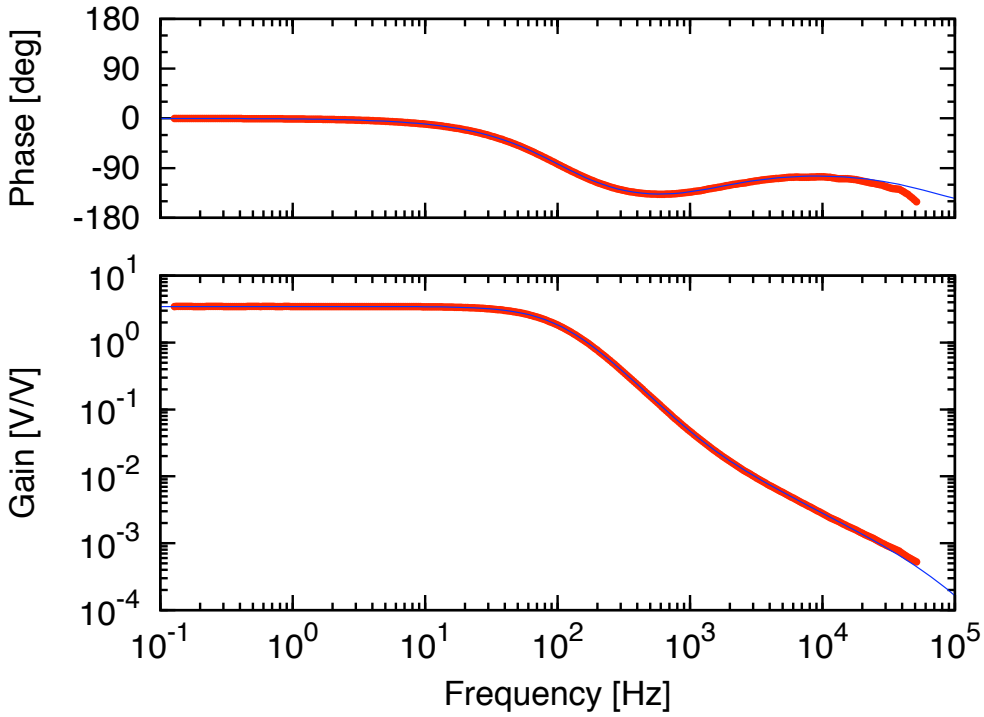

Figure 5.13 Bode diagram for the filter F_1 of IFO-2. Measured data (red filled circles) and fitting curves (blue solid) are shown.

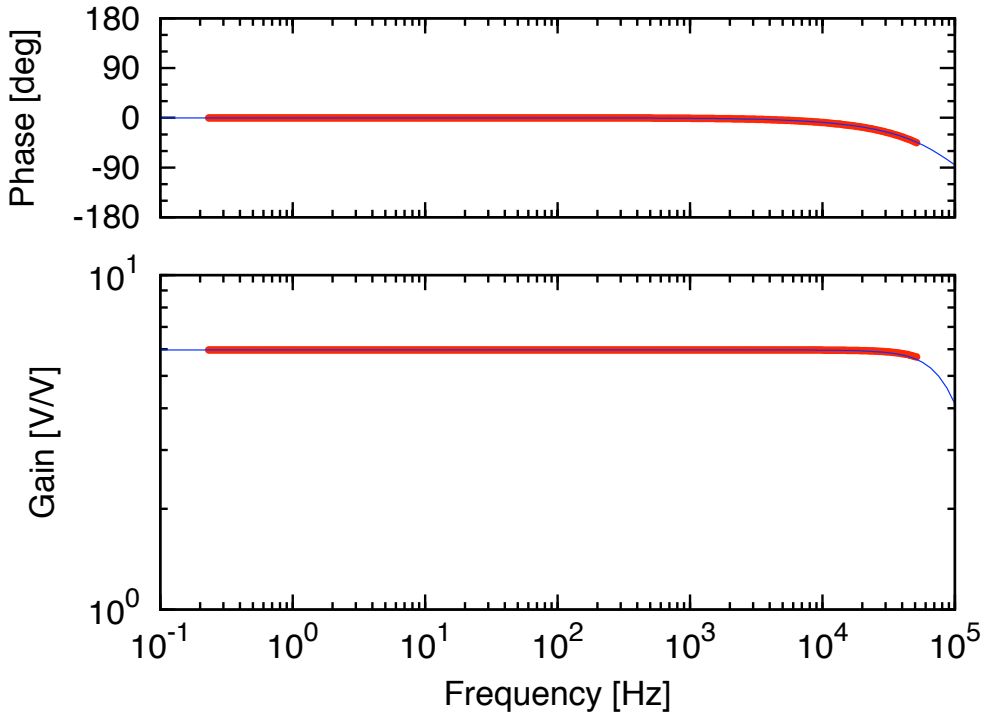

Figure 5.14 Bode diagram for the filter F_{pzt} of IFO-2. Measured data (red filled circles) and fitting curves (blue solid) are shown.

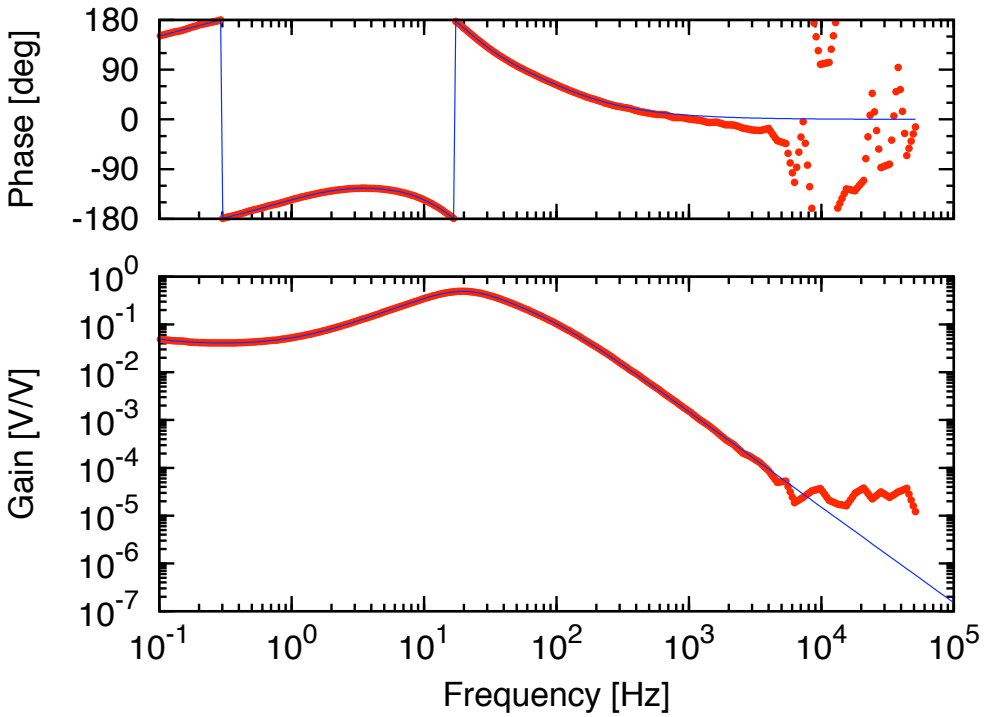

Figure 5.15 Bode diagram for the filter F_{thr} of IFO-2. Measured data (red filled circles) and fitting curves (blue solid) are shown.

where the left-hand side is the residual. The fluctuation is usually represented in the terms of displacement noise, which is the fluctuation of the half-way length L_+ of the cavity. Then δL_+ represents the raw displacement noise. The raw and residual displacement noises are shown in Figure 5.16. The solid red curve represents the residual noises, and the dashed blue curve represents the corresponding raw noises.

Because the both laser sources are the same model and the both interferometers are constructed on the same optical table, the estimation of the raw (free-running) displacement noise should be almost equal. Figure 5.17 shows the consistency of the raw displacement noises in IFO-1 (solid red curve) and IFO-2 (dashed blue curve). The inconsistency above 5 kHz would be from the difference of shot noise levels at the symmetric ports.

5.3 Calibration

We translate the output signals $V_{\mathrm{IF}}(f_{\mathrm{IF}})$ at the antisymmetric port of each interferometer into the corresponding gravitational waves $h(f_{\mathrm{GW}})$ with the Pockels cell in the recycling cavity (see Figure 5.1). The calibration factor required for this translation

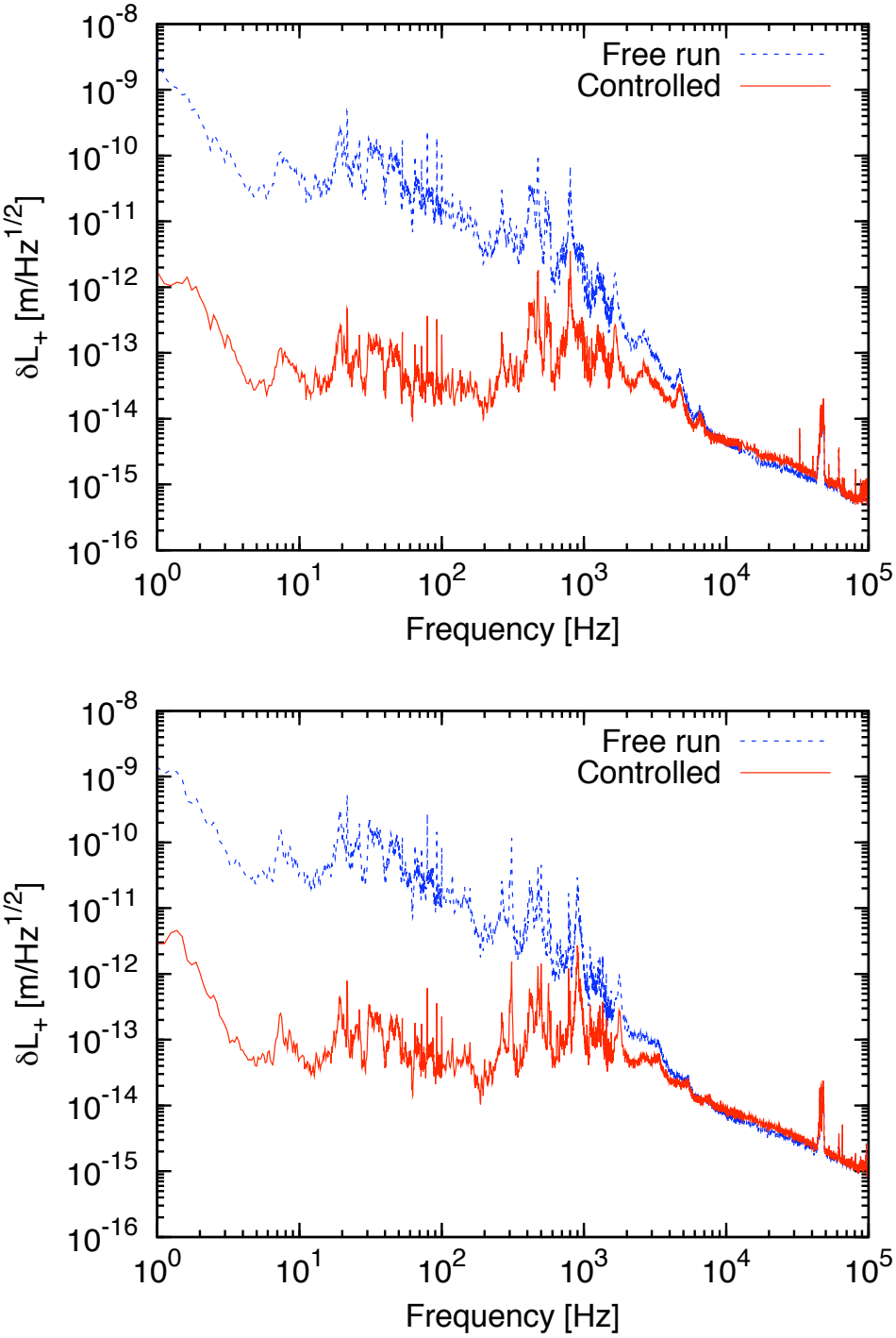

Figure 5.16 Displacement noises δL_+ in the interferometers. The solid red curve represents the residual noises with the stabilization, and the dashed blue curve represents the corresponding raw noises without the stabilization. The upper graph shows the measurements for IFO-1, and the lower graph for IFO-2.

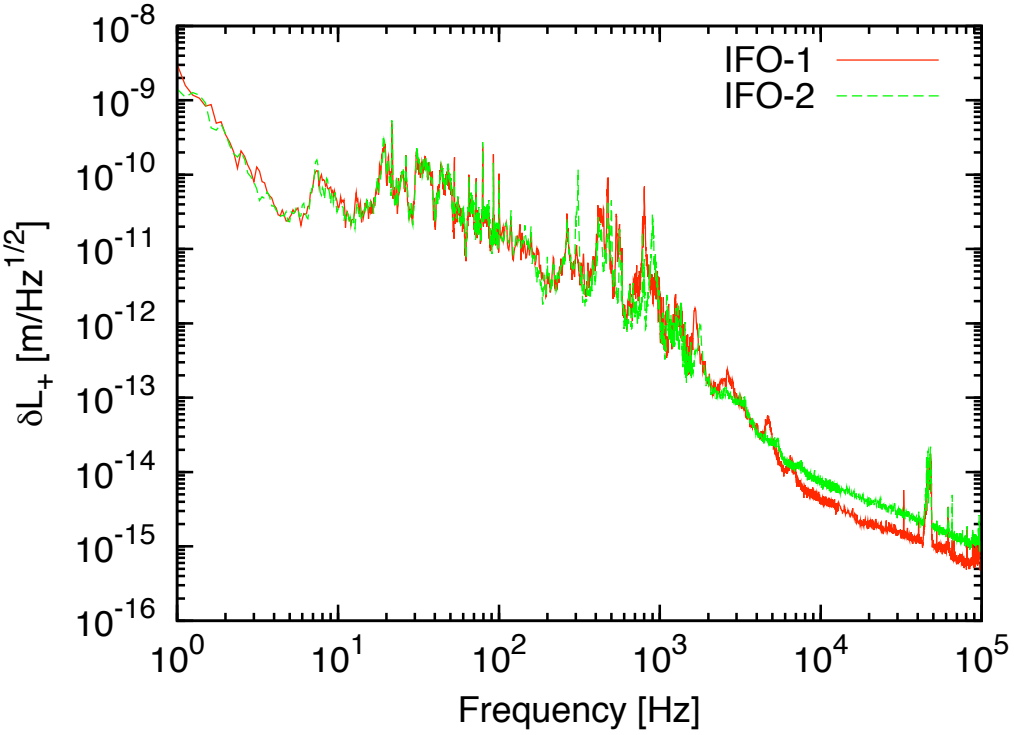

Figure 5.17 Raw displacement noises δL_+ in the interferometers. The solid red line represents the measurements for IFO-1, and the dashed green line for IFO-2.

is

$$\frac{V_{\rm IF}(f_{\rm IF})}{h(f_{\rm GW})} = \frac{V_{\rm IF}(f_{\rm IF})}{V_{\rm pc}(f_{\rm GW})} \cdot \frac{V_{\rm pc}(f_{\rm GW})}{\Gamma(f_{\rm GW})} \cdot \frac{\Gamma(f_{\rm GW})}{h(f_{\rm GW})} \tag{5.21}$$

$$= \frac{V_{\rm IF}(f_{\rm IF})}{V_{\rm pc}(f_{\rm GW})} \cdot \frac{1}{A_{\rm pc}(f_{\rm GW})} \cdot C_{\rm pc}(f_{\rm GW}), \tag{5.22}$$

where the intermediate frequency is $f_{\rm IF} = f_{\rm GW} - f_{\rm RF}$; $A_{\rm pc}$ represents the phase modulation efficiency of the Pockels cell; $C_{\rm pc} \equiv \Gamma/h$ is the conversion coefficient between the depth Γ of the phase modulation in the recycling cavity and the amplitude of a gravitational wave; $V_{\rm pc}(f_{\rm GW})$ is the applied voltage to the Pockels cell at $f_{\rm GW}$. Thus the calibration factor $V_{\rm IF}(f_{\rm IF})/h(f_{\rm GW})$ is derived from the three terms: $A_{\rm pc}$, $C_{\rm pc}$, and the ratio $V_{\rm IF}(f_{\rm IF})/V_{\rm pc}(f_{\rm GW})$.

For each interferometer, the phase modulation efficiency of the Pockels cell is measured and estimated as $A_{\rm pc} \simeq 8.5 \times 10^{-3}$ rad/V. The conversion coefficient $C_{\rm pc}$ is calculated in the following form:

$$\frac{1}{C_{\rm pc}(f)} = \frac{t_{\rm BS}^2 - r_{\rm BS}^2 \exp(i\pi f/\nu_{\rm FSR} \cdot l_1/L) \exp(-i2\pi f/\nu_{\rm FSR})}{2\frac{\nu_0}{f} \sin^2[\pi f/(2\nu_{\rm FSR})](r_{\rm BS}^2 + t_{\rm BS}^2) \exp(-i\pi f/\nu_{\rm FSR})}, \tag{5.23}$$

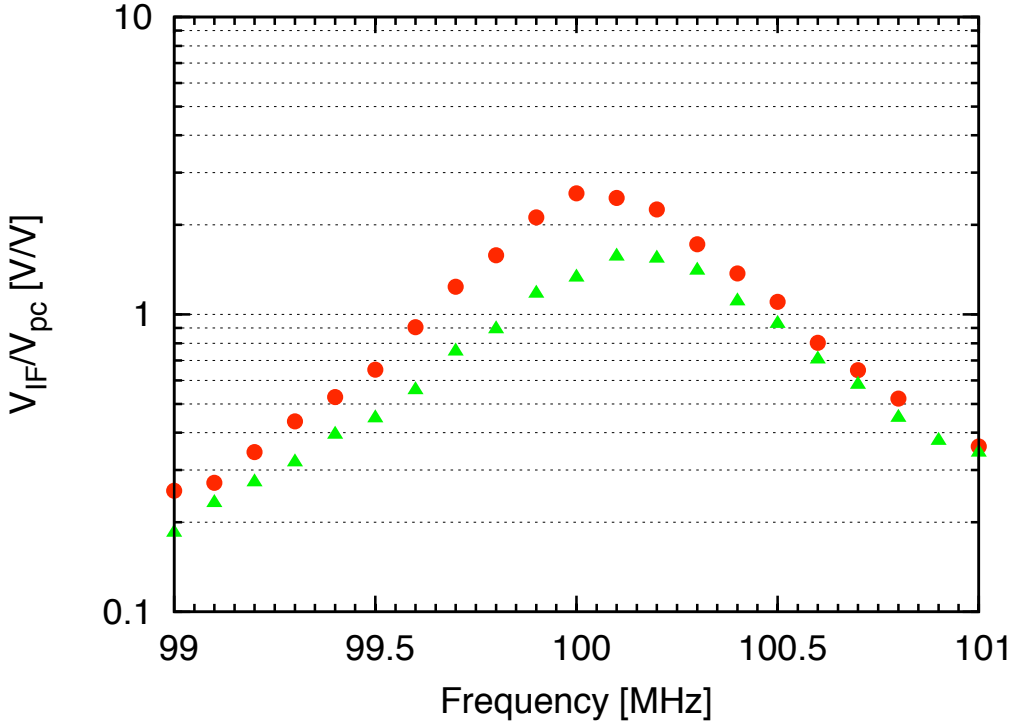

Figure 5.18 Measurements of the ratio $V_{\rm IF}(f_{\rm IF})/V_{\rm pc}(f_{\rm GW})$. The horizontal axis represents $f_{\rm GW}$, which corresponds to $f_{\rm IF} = f_{\rm GW} - f_{\rm RF}$ for the output signal $V_{\rm IF}$. The frequency of the RF sidebands is $f_{\rm RF} = 85.4$ MHz. The red filled circles represent the measurement for IFO-1, and the green filled triangles for IFO-2.

where $r_{\rm BS}$ and $t_{\rm BS}$ are amplitude reflectance and transmittance, respectively; $l_1 = 25\,{\rm cm}$ is a distance from the recycling mirror to the center of the Pockels cell. When $f = \nu_{\rm FSR}$, the response h/Γ is maximized if $l_1 = L$, while it is minimized if $l_1 = 0$ or $2L$. Today we do not have any standard star of gravitational waves for the calibration. Instead, the spacetime strain induced by gravitational waves is imitated by the phase modulation with the Pockels cell through the above relation (5.23).

For each interferometer, the ratio $V_{\rm IF}(f_{\rm IF})/V_{\rm pc}(f_{\rm GW})$ is measured as follows: the Pockels cell is driven by $V_{\rm pc}$ at discrete frequencies around 100 MHz, and the output signals $V_{\rm IF}$ at the corresponding intermediate frequencies are observed. Figure 5.18 shows the measurements, where the red filled circles represent the measurements for IFO-1, and the green filled triangles for IFO-2. Note that the input frequencies $f_{\rm GW}$ are different from the output (intermediate) frequencies $f_{\rm IF}$. When the light is detected at the antisymmetric port with the photodetector, the signal sidebands at $\nu_0 \pm f_{\rm GW}$ are mixed with the optical local oscillator at $\nu_0 \pm f_{\rm RF}$, then the electrical signals arises at $f_{\rm IF} = f_{\rm GW} - f_{\rm RF}$.

From the ratio $V_{\rm IF}(f_{\rm IF})/V_{\rm pc}(f_{\rm GW})$, we can estimate the finesse and the resonant frequency of each recycling cavity. For each interferometer, the output signal $V_{\rm IF}$ is

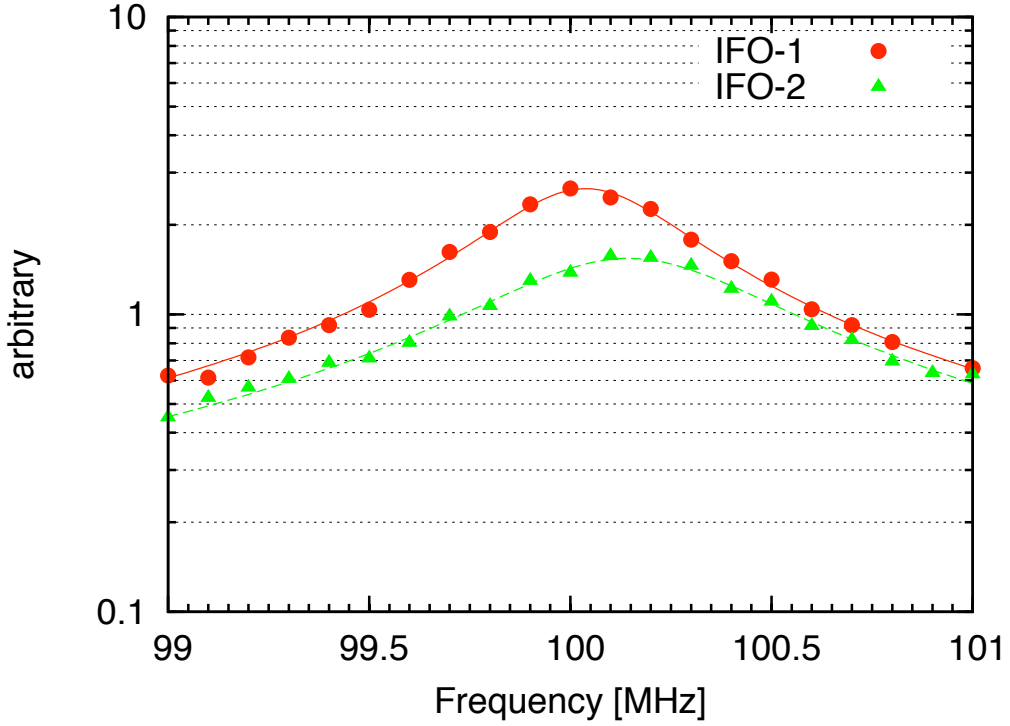

Figure 5.19 Frequency responses of the recycling cavities of IFO-1 and IFO-2. For IFO-1, red filled circles represent the measurements, to which solid red line is fitted with a resonant frequency of 100.038 MHz and a finesse of 203.352. For IFO-2, solid green triangles represent the measurements, to which dashed green line is fitted with a resonant frequency of 100.144 MHz and a finesse of 142.562.

affected by the photodetector at the antisymmetric port. Each photodetector has a resonance at $f_c = 14.75$ MHz, with $Q = 13.7$, thus the frequency response is

$$R_{\rm PD}(f) \propto \frac{{\rm i}f/(f_{\rm c}Q)}{1 + {\rm i}f/(f_{\rm c}Q) - (f/f_c)^2}. \tag{5.24}$$

Removing this response from the ratio $V_{\rm IF}(f_{\rm IF})/V_{\rm pc}(f_{\rm GW})$, one can estimate the frequency response Eq.(3.53) of each recycling cavity as shown in Figure 5.19. For IFO-1, red filled circles represent the measurements, to which the solid red line is fitted with a resonant frequency of 100.038 MHz and a finesse of 203.352. For IFO-2, solid green triangles represent the measurements, to which the dashed green line is fitted with a resonant frequency of 100.144 MHz and a finesse of 142.562.

5.4 Sensitivity to 100-MHz gravitational waves

Figure 5.20 shows the strain sensitivities of the interferometers to gravitational waves. Red (solid) and green (dashed) curves are for IFO-1 and IFO-2, respectively.

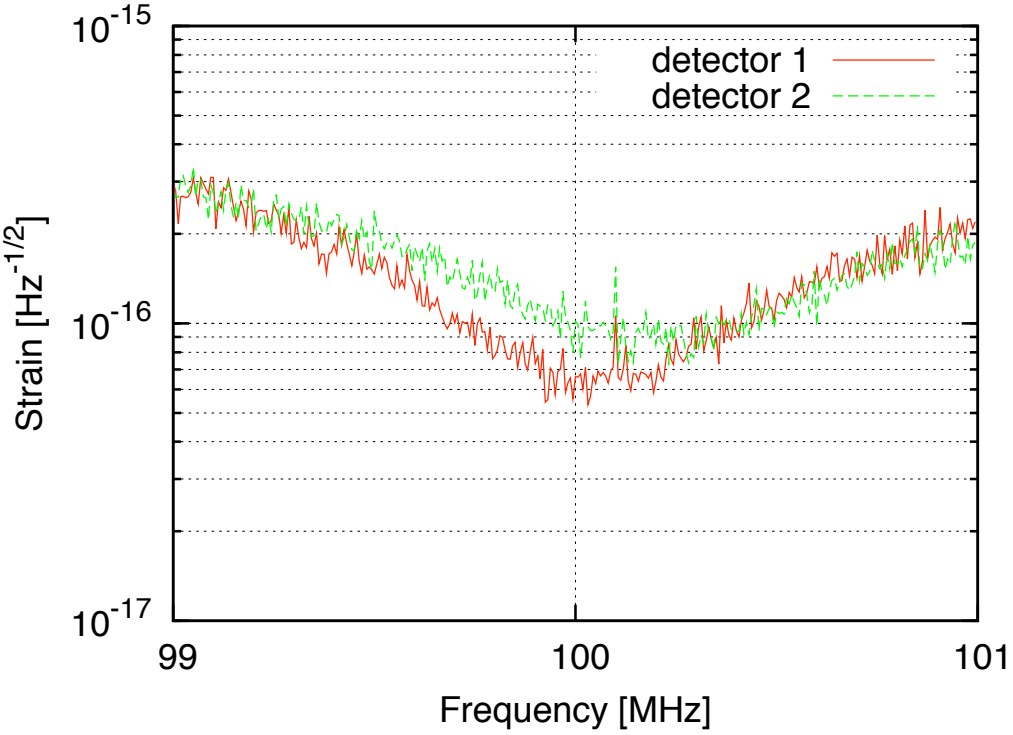

Figure 5.20 Strain sensitivities of interferometers to gravitational waves. Red (solid) and green (dashed) curves are for IFO-1 and IFO-2, respectively.

For IFO-1, the best sensitivity is about $6.4 \times 10^{-17}\,\mathrm{Hz}^{-1/2}$ at 100.0 MHz. For IFO-2, the best sensitivity is about $8.5 \times 10^{-17}\,\mathrm{Hz}^{-1/2}$ at 100.1 MHz. Note that the "strain sensitivity" described here is derived as follows: the output of each interferometer is caused by an optimal gravitational wave, that is, propagating in the vertical direction with plus-polarization.

Now we use a BS designed to be $r_{\mathrm{BS}} = t_{\mathrm{BS}} = 1/\sqrt{2}$ (nominal), thus only a few amounts of 1st LO (optical local oscillator) due to the practical imbalance of the BS ratio can appear at the dark port; we tune the alignment of the Sagnac part slightly so that a small amount of 1st LO appears at the dark port. At each dark port, the laser power becomes 15 mW, that is, about 3% of the incident light.

Chapter 6

Search for a stochastic background of 100-MHz gravitational waves

6.1 Output signals from the interferometers

Let $x_1(t)$ and $x_2(t)$ represent strain signals from IFO-1 and IFO-2, respectively (see Figure 5.1); the strain signals are converted from the output signals of the interferometers with the assumption that each output signal is caused by the *optimal* gravitational waves — propagating in the vertical direction with plus polarization. The *one-sided* amplitude specturm density per unit frequency interval[1] of $x_i(t)$, where $i = 1, 2$, corresponds to the illustration in Figure 5.20.

Each strain signal $x_i(t)$ contains the random noise in IFO-i, and would contain the desired signals from the gravitational-wave background. Then one finds

$$x_i(t) = s_i(t) + n_i(t), \qquad i = 1, 2 \tag{6.1}$$

where $n_i(t)$ is the random noise in IFO-i at time t, and $s_i(t)$ is the gravitational-wave signal at time t. Hereafeter we assume that [$\langle \ldots \rangle$ represents an ensemble average.]

$\langle n_i(t) \rangle = 0$ and $\langle s_i(t) \rangle = 0$, thus $\langle x_i(t) \rangle = 0$,
$n_1(t)$ and $n_2(t)$ are independent, and
$n_i(t)$ and $s_j(t)$ are also independent $(i, j = 1, 2)$.

On the other hand, the desired signals $s_1(t)$ and $s_2(t)$ are not independent, because they are from the identical source: a gravitational-wave background $s(t)$. If the two interferometers are co-located and co-aligned, the signals satisfy $s_1(t) = s_2(t)$.

For the physically correct interpretation of the interferometer outputs into the starin

[1] It is the square root of the *one-sided* power sepctrum density per unit frequency interval.

signals, one must take into consideration that the output signal will be caused by the gravitational waves from all directions with plus and cross polarizations. In this thesis, this consideration is included in the definition of the *reduced* overlap reduction function in Eq.(6.32).

6.2 Cross-correlation analysis

6.2.1 Cross-correlation function

A cross-correlation of two random signals $x_1(t), x_2(t)$ is defined as [61]

$$R_{12}(t, t') = \langle x_1(t) x_2(t') \rangle, \tag{6.2}$$

where the symbol $\langle \ldots \rangle$ indicates an ensemble average. Generally, the cross-correlation is a time-dependent function. On the other hand, if the signals are (weakly) stationary, the cross-correlation becomes a function of a time interval $\tau = t' - t$. Thus one finds $R_{12}(\tau) = R_{12}(t, t+\tau)$, or

$$R_{12}(\tau) = \langle x_1(t) x_2(t+\tau) \rangle. \tag{6.3}$$

Note that $R_{12}(\tau) = R_{21}(-\tau)$. From the Wiener-Khinchin theorem, it is also written as

$$R_{12}(\tau) = \int_{-\infty}^{\infty} S_{12}(f)\, \mathrm{e}^{\mathrm{i}2\pi f\tau}\, df, \tag{6.4}$$

where $S_{12}(f)$ is a *two-sided* cross-spectrum density per unit frequency interval for the signals $x_1(t), x_2(t)$. Note that $S_{12}(f) = S_{12}^*(-f)$. From Eqs. (6.3) and (6.4),

$$\langle \tilde{x}_1^*(f) \tilde{x}_2(f') \rangle = S_{12}(f) \delta(f - f'), \tag{6.5}$$

where $\delta(f)$ is the Dirac delta function, and $\tilde{x}_i(f)$ is the Fourier component of $x_i(t)$ defined as follows:

$$x_i(t) = \int_{-\infty}^{\infty} \tilde{x}_i(f)\, \mathrm{e}^{\mathrm{i}2\pi ft}\, df, \tag{6.6}$$

$$\tilde{x}_i(f) = \int_{-\infty}^{\infty} x(t)\, \mathrm{e}^{-\mathrm{i}2\pi ft}\, dt. \tag{6.7}$$

In particular,

$$R_{12}(0) = \langle x_1(t) x_2(t) \rangle \tag{6.8}$$

$$= \int_{-\infty}^{\infty} S_{12}(f)\, df. \tag{6.9}$$

Here recall Eq.(6.1) and assume $s(t) = s_1(t) = s_2(t)$, then one can find

$$R_{12}(0) = \langle (s_1(t) + n_1(t))(s_2(t) + n_2(t)) \rangle \tag{6.10}$$
$$= \langle s_1(t) s_2(t) \rangle \tag{6.11}$$
$$= \left\langle s^2(t) \right\rangle, \tag{6.12}$$

where the second equality is from the independency among $s(t)$, $n_1(t)$, and $n_2(t)$. The variance of $s(t)$ is written as

$$\sigma_s^2 = \left\langle s^2(t) \right\rangle - \langle s(t) \rangle^2 \tag{6.13}$$
$$= \left\langle s^2(t) \right\rangle \tag{6.14}$$
$$= R_{12}(0), \tag{6.15}$$

where the second equality comes from that the signal $s(t)$ has a zero mean: $\langle s(t) \rangle = 0$. Therefore we can estimate the energy density of a gravitational-wave background, which is proportional to σ_s^2, by calculating the zero-lag cross-correlation $R_{12}(0)$ of the two output signals $x_1(t), x_2(t)$.

On the other hand, if there is only one interferometer, the variance of the output signal $x(t)$ is

$$\sigma_x^2 = \left\langle x^2(t) \right\rangle - \langle x(t) \rangle^2 \tag{6.16}$$
$$= \left\langle s^2(t) \right\rangle + \left\langle n^2(t) \right\rangle \tag{6.17}$$
$$= \sigma_s^2 + \sigma_n^2, \tag{6.18}$$

where the second equality is from the independency of $s(t)$ and $n(t)$. The relation $\sigma_s^2 \ll \sigma_n^2$ would be satisfied for the actual gravitational-wave detectors in the prensent day, thus one finds

$$\sigma_x^2 \simeq \sigma_n^2. \tag{6.19}$$

In this case, the output signal is dominated by the random noises in the interferometer.

6.2.2 Cross-correlation estimate I: simple case

For the actual experiment, the observation time interval is finite; the data record has the beginning and ending. Thus we need a finite-time statistic from which σ_s^2 can be estimated. Here we define a statistic:

$$Z_{12} = \frac{1}{T} \int_0^T x_1(t) x_2(t)\, dt. \tag{6.20}$$

Signal estimate

The ensemble average of Z_{12} is

$$\mu_Z \equiv \langle Z_{12} \rangle \tag{6.21}$$

$$= \left\langle \frac{1}{T} \int_0^T x_1(t) x_2(t)\, dt \right\rangle \tag{6.22}$$

$$= \frac{1}{T} \int_0^T \langle s_1(t) s_2(t) \rangle\, dt, \tag{6.23}$$

$$= \frac{1}{T} \int_{-\infty}^{\infty} df \int_{-\infty}^{\infty} df' \delta_T(f - f') \langle \tilde{s}_1^*(f) \tilde{s}_2(f') \rangle \mathrm{e}^{-\mathrm{i}\pi(f-f')T} \tag{6.24}$$

where the finite-time delta function is defined as

$$\delta_T(f) \equiv \int_{-T/2}^{T/2} \exp(-\mathrm{i}2\pi f t)\, dt \tag{6.25}$$

$$= \frac{\sin(\pi f T)}{\pi f} \tag{6.26}$$

$$= T\, \mathrm{sinc}(\pi f T). \tag{6.27}$$

The function $\delta_T(f)$ reduces to the Dirac delta function[2] in the limit of $T \to \infty$. Thus one finds

$$\mu_Z \simeq \frac{1}{T} \int_{-\infty}^{\infty} \langle \tilde{s}_1^*(f) \tilde{s}_2(f) \rangle df \tag{6.28}$$

in the long-observation limit.

As shown in Eq.(3.103),

$$\tilde{s}_i(f) = \sum_{A=+,\times} \int_\Omega d\mathbf{\Omega}\, \tilde{h}_A(f; \mathbf{\Omega}) D_i^A(\mathbf{\Omega})\, \mathrm{e}^{-\mathrm{i}2\pi f \mathbf{\Omega} \cdot \mathbf{X}_i / c}, \tag{6.29}$$

thus one finds

$$\langle \tilde{s}_1^*(f) \tilde{s}_2(f') \rangle = \sum_A \sum_{A'} \int_\Omega d\mathbf{\Omega} \int_{\Omega'} d\mathbf{\Omega}' \left\langle \tilde{h}_A^*(f; \mathbf{\Omega}) \tilde{h}_{A'}(f'; \mathbf{\Omega}') \right\rangle \left[D_1^A(f; \mathbf{\Omega}) \right]^* D_2^{A'}(f'; \mathbf{\Omega}') \exp\left[\mathrm{i}2\pi (f \mathbf{\Omega} \cdot \mathbf{X}_1 - f' \mathbf{\Omega}' \cdot \mathbf{X}_2)/c \right]. \tag{6.30}$$

---

[2] This is true in the sense of

$$\lim_{T \to \infty} \int_{-\infty}^{\infty} f(x) \delta_T(x)\, dx = f(0).$$

Note that the limit

$$\lim_{T \to \infty} \delta_T(x)$$

does not exist in the usual sense. See, for example, Ref. [62].

Note that the *reduced* detector tensor $D_i^A(\mathbf{\Omega})$ is a complex function. The superscript "$*$" attached to $D_1^A(\mathbf{\Omega})$ indicates the complex conjugate of $D_1^A(\mathbf{\Omega})$. The superscript can be omitted in the low-frequency limit, where the detector tensor reduces to a real function [46, 35].

Substituting Eq.(2.62) into the above equation yields

$$\langle \tilde{s}_1^*(f)\tilde{s}_2(f')\rangle = \frac{3H_0^2}{20\pi^2}\frac{\Omega_{\rm gw}(|f|)}{|f|^3}\delta(f-f')\gamma_{12}(f), \tag{6.31}$$

where the *reduced*[3] overlap reduction function $\gamma_{12}(f)$ is defined as

$$\gamma_{12}(f) \equiv \frac{5}{8\pi}\sum_A \int_\Omega d\mathbf{\Omega}\ \left[D_1^A(f;\mathbf{\Omega})\right]^* D_2^A(f;\mathbf{\Omega})\, {\rm e}^{-{\rm i}2\pi f\,(\mathbf{X}_2-\mathbf{X}_1)\cdot\mathbf{\Omega}/c}. \tag{6.32}$$

The factor $\frac{5}{8\pi}$ is a normalization constant. Although $D_i^A(f;\mathbf{\Omega})$ is a complex function $(i=1,2)$, $\gamma_{12}(f)$ is a real function, thus

$$\gamma_{21}(f) = \gamma_{12}^*(f) = \gamma_{12}(f). \tag{6.33}$$

In the low-frequency limit, Eq.(6.32) reduces to the *usual* overlap reduction function (see, for example, Refs. [46, 63, 64, 65]), which represents the reduction of the signal correlation due to the distance between the two interferometer sites. Note that a gravitational wave travels in vacuum at the speed of light.

As a result, the ensemble average of Z_{12} is written as

$$\mu_Z = \int_{-\infty}^{\infty} \frac{3H_0^2}{20\pi^2}\frac{\Omega_{\rm gw}(|f|)}{|f|^3}\gamma_{12}(f)\, df. \tag{6.34}$$

Thus we can estimate $\Omega_{\rm gw}(f)$ from the ensemble average of Z_{12}.

In the time domain, one finds

$$\langle s_1(t)s_2(t+\tau)\rangle = \int_{-\infty}^{\infty} df \int_{-\infty}^{\infty} df' \langle \tilde{s}_1^*(f)\tilde{s}_2(f')\rangle\, {\rm e}^{{\rm i}2\pi(f'-f)\tau} \tag{6.35}$$

$$= \int_{-\infty}^{\infty} \frac{3H_0^2}{20\pi^2}\frac{\Omega_{\rm gw}(|f|)}{|f|^3}\gamma_{12}(f)\, {\rm e}^{{\rm i}2\pi f\tau}\, df \tag{6.36}$$

$$= \int_{-\infty}^{\infty} S_{12}(f)\, {\rm e}^{{\rm i}2\pi f\tau}\, df, \tag{6.37}$$

where $S_{12}(f)$ is the two-sided cross-spectrum density per unit frequency interval for $s_1(t)$ and $s_2(t)$, and the last equality is from the Wiener-Khinchin theorem. If the noises inherent in the interferometers could be ignored, the gravitational-wave background can be measured directly with the relation:

$$S_{12}(f) = \frac{3H_0^2}{20\pi^2}\frac{\Omega_{\rm gw}(|f|)}{|f|^3}\gamma_{12}(f). \tag{6.38}$$

[3] The term "reduced" is attached so that one can distinguish $\gamma_{12}(f)$ defined in Eq.(6.32) from the "overlap reduction function" defined in Ref. [48].

The right-hand side is a real function because $\Omega_{\rm gw}(f)$ and $\gamma_{12}(f)$ are real functions. Thus the cross-spectrum density $S_{12}(f)$ is considered to be a power specturm density of a real signal, that is, the gravitational-wave background.

Signal-to-noise ratio of the estimate

The uncertainty or *noise* in the estimate is expressed as the variance of Z_{12}, which is

$$\sigma_Z^2 = \left\langle Z_{12}^2 \right\rangle - \left\langle Z_{12} \right\rangle^2 \tag{6.39}$$

$$\simeq \left\langle Z_{12}^2 \right\rangle, \tag{6.40}$$

where the second equality would be valid in the realsitic case today. Because the noises $n_1(t)$ and $n_2(t)$ are independent, one finds [46]

$$\langle x_1(t)x_2(t)x_1(t')x_2(t')\rangle \simeq \langle n_1(t)n_2(t)n_1(t')n_2(t')\rangle \tag{6.41}$$

$$= \langle n_1(t)n_1(t')\rangle\langle n_2(t)n_2(t')\rangle. \tag{6.42}$$

Then the right-hand side of Eq.(6.40) is written as

$$\left\langle Z_{12}^2 \right\rangle = \frac{1}{T^2}\int_0^T dt \int_0^T dt' \, \langle x_1(t)x_2(t)x_1(t')x_2(t')\rangle \tag{6.43}$$

$$\simeq \frac{1}{T^2}\int_0^T dt \int_0^T dt' \, \langle n_1(t)n_1(t')\rangle\langle n_2(t)n_2(t')\rangle \tag{6.44}$$

$$= \frac{1}{4T^2}\int_{-\infty}^{\infty} df \int_{-\infty}^{\infty} df' \, \delta_T^2(f-f')P_1(|f|)P_2(|f'|), \tag{6.45}$$

where $P_i(f)$ is the *one-sided* power spectrum density per unit frequency interval for the noises in the interferometers ($i = 1, 2$), and is written as

$$\langle \tilde{n}_i^*(f)\tilde{n}_i(f')\rangle = \frac{1}{2}P_i(|f|)\delta(f-f'). \tag{6.46}$$

Now assume that T is large enough such that one of the finite-time delta functions in Eq.(6.45) is replaced by the Dirac delta function. Then Eq.(6.45) reduces to

$$\sigma_Z^2 \simeq \left\langle Z_{12}^2 \right\rangle \simeq \frac{1}{4T}\int_{-\infty}^{\infty} P_1(|f|)P_2(|f|)\, df. \tag{6.47}$$

The power signal-to-noise ratio (SNR) is defined as

$$\frac{\mu_Z}{\sigma_Z} = \frac{\mu_Z}{\sqrt{\sigma_Z^2}} \tag{6.48}$$

$$\simeq \frac{3H_0^2}{10\pi^2}\sqrt{T}\,\frac{\displaystyle\int_{-\infty}^{\infty} \frac{\Omega_{\rm gw}(|f|)}{|f|^3}\gamma_{12}(f)\, df}{\sqrt{\displaystyle\int_{-\infty}^{\infty} P_1(|f|)P_2(|f|)\, df}}. \tag{6.49}$$

The equation states that the SNR increases proportional to the square root of the observation time interval T. Therefore we can improve the SNR by cross-correlating the outputs of the two interferometers over a long observation time interval.

6.2.3 Cross-correaltion estimate II: optimal filtering

In the low-frequency limit, an optimal filter has been used for the cross-correlation analysis (for example, see Refs. [46, 51, 52, 34]). The filter is expected to optimize (or maximize) the power signal-to-noise ratio of the estimate. Here we redefine the statistic Z_{12} in Eq. (6.20) as

$$Z_{12} \equiv \frac{1}{T}\int_0^T dt \int_0^\infty dt'\, x_1(t)x_2(t')Q(t-t'), \tag{6.50}$$

where $Q(t)$ represents a filter, which is applied to the signal $x_2(t)$ in this expression. We can as well maximize the power signal-to-noise ratio by the choise of the proper filter.

Signal estimate

In the frequency domain, Eq.(6.50) is written as

$$Z_{12} = \frac{1}{T}\int_{-\infty}^{\infty} df \int_{-\infty}^{\infty} df'\, \delta_T(f-f')\tilde{x}_1^*(f)\tilde{x}_2(f')\tilde{Q}(f')\,\mathrm{e}^{-\mathrm{i}\pi(f-f')T}, \tag{6.51}$$

where $\tilde{Q}(f)$ is the frequency component of $Q(t)$. The ensemble average of Z_{12} is written as

$$\mu_Z \equiv \langle Z_{12}\rangle \tag{6.52}$$

$$= \frac{1}{T}\int_{-\infty}^{\infty} df \int_{-\infty}^{\infty} df'\, \delta_T(f-f')\langle\tilde{s}_1^*(f)\tilde{s}_2(f')\rangle\tilde{Q}(f')\,\mathrm{e}^{-\mathrm{i}\pi(f-f')T}. \tag{6.53}$$

From Eq.(6.31), one finds

$$\mu_Z = \frac{3H_0^2}{20\pi^2}\int_{-\infty}^{\infty} \frac{\Omega_{\mathrm{gw}}(|f|)}{|f|^3}\gamma_{12}(f)\tilde{Q}(f)\,df. \tag{6.54}$$

Signal-to-noise ratio of the estimate

The uncertainty or noise in the estimate is expressed as the variance of Z_{12}, which is

$$\sigma_Z^2 = \left\langle Z_{12}^2\right\rangle - \langle Z_{12}\rangle^2 \tag{6.55}$$

$$\simeq \left\langle Z_{12}^2\right\rangle, \tag{6.56}$$

where the second equality would be valid in the realsitic case today. In the same procedure from Eq.(6.42) to Eq.(6.45),

$$\sigma_Z^2 \simeq \frac{1}{T^2}\int_{-\infty}^{\infty} df \int_{-\infty}^{\infty} df' \int_{-\infty}^{\infty} d\nu \int_{-\infty}^{\infty} d\nu'\, \delta_T(f-f')\delta_T(\nu-\nu')\times \\ \langle \tilde{n}_1^*(f)\tilde{n}_2(f')\tilde{n}_1(\nu)\tilde{n}_2^*(\nu')\rangle \tilde{Q}(f')\tilde{Q}^*(\nu')\, \mathrm{e}^{-\mathrm{i}\pi(f-f')T}\, \mathrm{e}^{+\mathrm{i}\pi(\nu-\nu')T}, \tag{6.57}$$

where

$$\langle \tilde{n}_1^*(f)\tilde{n}_2(f')\tilde{n}_1(\nu)\tilde{n}_2^*(\nu')\rangle = \langle \tilde{n}_1^*(f)\tilde{n}_1(\nu)\rangle\langle \tilde{n}_2(f')\tilde{n}_2^*(\nu')\rangle. \tag{6.58}$$

Substituting Eq.(6.46) yields

$$\sigma_Z^2 \simeq \frac{1}{4T^2}\int_{-\infty}^{\infty} df \int_{-\infty}^{\infty} df' \delta_T^2(f-f') P_1(|f|)P_2(|f'|)\,|\tilde{Q}(f')|^2 \tag{6.59}$$

$$\simeq \frac{1}{4T}\int_{-\infty}^{\infty} df P_1(|f|)P_2(|f|)\,|\tilde{Q}(f)|^2, \tag{6.60}$$

where the same procedure as Eq.(6.20) gives the last equality.

As a result, from Eqs.(6.54) and (6.60), the power signal-to-noise ratio with the filter $Q(t)$ is written as

$$\mathrm{SNR} \equiv \frac{\mu_Z}{\sqrt{\sigma_Z^2}} = \frac{3H_0^2}{10\pi^2}\sqrt{T}\frac{\displaystyle\int_{-\infty}^{\infty} |f|^{-3}\,\Omega_{\mathrm{gw}}(|f|)\gamma_{12}(f)\tilde{Q}(f)\,df}{\displaystyle\sqrt{\int_{-\infty}^{\infty} P_1(|f|)P_2(|f|)\,|\tilde{Q}(f)|^2\,df}}. \tag{6.61}$$

The power SNR (per unit observation time period) is maximized with the so-called optimal filter [46]:

$$\tilde{Q}(f) = K\frac{\Omega_{\mathrm{gw}}(|f|)\,\gamma_{12}(f)}{|f|^3 P_1(|f|)P_2(|f|)}, \tag{6.62}$$

where $K \in \mathbb{R}$ is a real normalization constant. The optimal estimate for the ensemble average of Z_{12} is

$$\mu_Z = K\frac{3H_0^2}{20\pi^2}\int_{-\infty}^{\infty} \frac{\Omega_{\mathrm{gw}}^2(|f|)\,\gamma_{12}^2(f)}{|f|^6 P_1(|f|)P_2(|f|)}\,df, \tag{6.63}$$

the noise in the estimate (the variance of Z_{12}) is

$$\sigma_Z^2 = \frac{K^2}{4T}\int_{-\infty}^{\infty} \frac{\Omega_{\mathrm{gw}}^2(|f|)\gamma_{12}^2(f)}{|f|^6 P_1(|f|)P_2(|f|)}\,df, \tag{6.64}$$

and thus the optimal (or maximized) power SNR is written as

$$\mathrm{SNR} = \frac{3H_0^2}{10\pi^2}\sqrt{T}\sqrt{\int_{-\infty}^{\infty} \frac{\Omega_{\mathrm{gw}}^2(|f|)\,\gamma_{12}^2(f)}{|f|^6 P_1(|f|)P_2(|f|)}\,df}. \tag{6.65}$$

The SNR increases proportional to the square root of the observation time interval T. This time-dependency is the same as the previous SNR defined in Eq.(6.49). The difference is the weighting factor in the denominator of the integrand in μ_Z, that is, the interferometer noises $P_1(f), P_2(f)$. If one *a priori* knows that the interferometer noises are large at certain frequencies, the weighting factor reduces the contributions of $x_1(t)$ and $x_2(t)$ to μ_Z at the frequencies. This optimal filter is a kind of so-called matched filter [66], and we need to know in advance what the desired signal $\Omega_{\rm gw}(f)$ itself is to be, before preparing the optimal filter to optimally estimate the desired signal. Thus some assumptions are requred for the frequency spectrum of $\Omega_{\rm gw}(f)$ in this optimal filtering scheme.

Note that the SNR is independent from the choice of K, thus the normalization constant K will be chosen as an appropriate value such that we can derive $\Omega_{\rm gw}(f)$ from μ_Z.

6.3 Data reduction

6.3.1 Preprocessing

Signal downconversion

Figure 6.1 shows the schematic view of our gravitational-wave detector, which consists of two interferometers (see also Figure 5.1). The raw output from each interferometer is the intermediate-frequency (IF) voltage signal at $f_{\rm IF} = f_{\rm GW} - f_{\rm RF}$, where $f_{\rm GW}$ is the frequency of the original gravitational wave, and $f_{\rm RF}$ is the frequency spacing of the RF sidenbands (or 1st LO) from the carrier light in Fourier space.

The IF signal is downconverted into the audio-frequency (AF) signal with the 2nd LO at

$$f_{\rm LO2} = f_0 - f_{\rm RF} - \frac{1}{2}\Delta f, \tag{6.66}$$

where f_0 is the center frequency of the observation, and Δf is the frequency bandwidth to be analyzed. If the two interferometers both have the same resonant frequency $\nu_{\rm FSR}$, the center frequency f_0 should be chosen as $\nu_{\rm FSR}$. But the actual interferometers have the different repsonses to gravitational waves (see Figures 5.19 and 5.20). As a whole, the original gravitational waves at $f_{\rm GW}$ are downconverted into the voltage signal at

$$f_{\rm AF} = f_{\rm IF} - f_{\rm LO2} \tag{6.67}$$

$$= f_{\rm GW} - f_0 + \frac{1}{2}\Delta f. \tag{6.68}$$

Gravitational waves at $f_{\rm GW} = f_0 - \Delta f/2$ are converted into the 0 Hz voltage signal. Gravitational waves at f_0 are converted into $\Delta f/2$. Gravitatinal waves at $f_0 + \Delta f/2$ are converted into Δf. We choose $f_0 = 100.1$ MHz and $\Delta f/2 = 3.16$ kHz, thus the

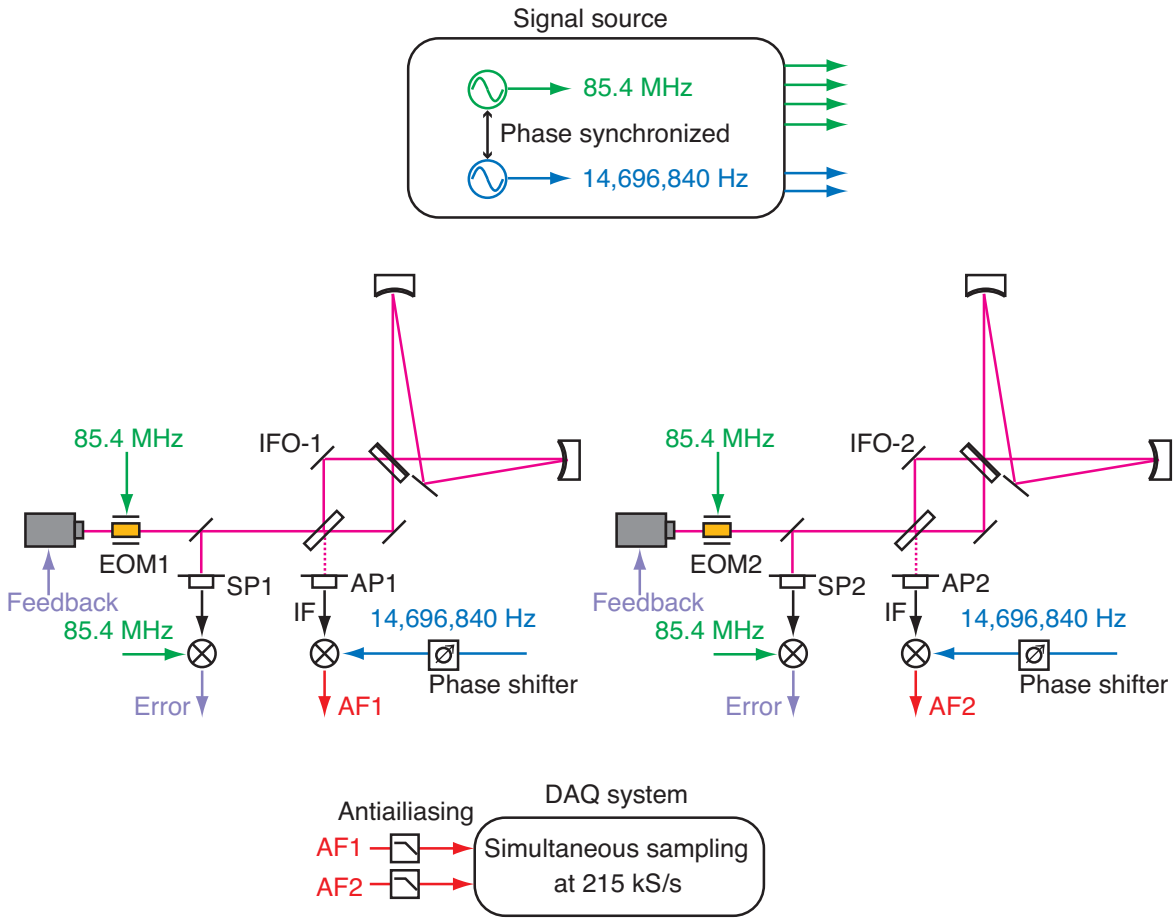

Figure 6.1 Schematic view of the interferometers. The RF signal for the phase-modulation at $f_{\rm RF} = 85.4$ MHz and the 2nd LO at $f_{\rm LO2} \simeq 14.7$ MHz are phase-synchronized. A total of six RF signals illustrated in this figure are originated from a single source.

2nd LO is

$$f_{\rm LO2} = 100.1\ {\rm MHz} - 85.4\ {\rm MHz} - 3.16\ {\rm kHz} \tag{6.69}$$

$$= 14.696840\ {\rm MHz}\,. \tag{6.70}$$

The 2nd LO and the modulation signal at $f_{\rm RF}$ is phase-synchronized (see Figure 6.1).

Common noises (correlated noises) in $x_1(t)$ and $x_2(t)$ cannot be removed with the cross-correlation method described in the previous section. Note that the low-frequency components of the electrical signals would be dominated by noises, and such the low-frequency noises could be commonly mixed in the downconverted signals. In order to avoid the low-frequency common noises, we use the data of about 2 kHz bandwidth centerd at 3.16 kHz, which correpsonds to the gravitational-wave background ranging from 100.099 MHz to 100.101 MHz.

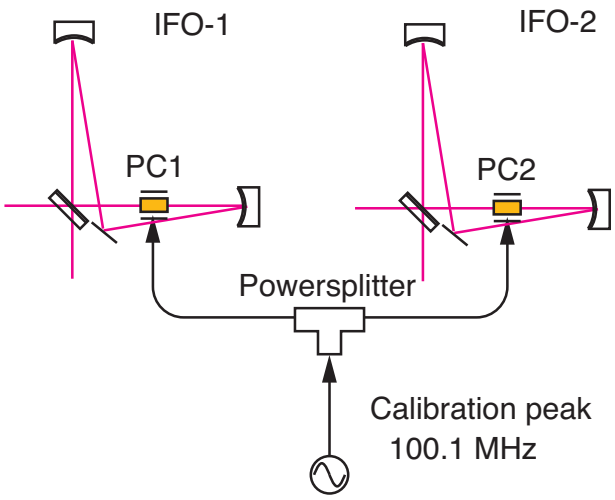

Figure 6.2 Imitation of a gravitational wave at 100.1 MHz propagating in the vertical direction with plus polarization. The calibration peak is split into two ways, and each are supplied to each Pockels cell (PC1 or PC2), using cables with the same length.

Induction of the calibration peak

For each interferometer, the AF signal is translated into the gravitational-wave signal with the Pockels cell in the recycling cavity (PC1 or PC2 in Figure 5.1)

In the same manner as section 5.3, we imitate a gravitational wave at 100.1 MHz propagating in the vertical direction with plus-polarization. A signal source generates a sinusoidal signal at 100.1 MHz (calibration peak). The calibration peak is split into two ways, and each are supplied to each Pockels cell, using cables with the same length (see Figure 6.2).

Compensation of the relative phase

With the calibration peak, we tune the demodulation phase at AP2 with a phase shifter (PS) for the IFO-2 so that the relative phase between the AF signals (AF1 and AF2) at 3.16 kHz vanishes (see Figure 6.1).

In fact, the frequency responses of the two interferometers are different as shown in Figure 5.19. Thus, even if the optimal gravitational wave is incident on the interferometers, the AF1 and AF2 are different in their amplitudes and phases. Now consider that $\tilde{x}_0(f_{\rm GW}^{\rm cal})$ is the Fourier component of the optimal gravitational wave at $f_{\rm GW}^{\rm cal}$. Then the raw AF1 and AF2 are (indicated by $\tilde{r}_1$ and $\tilde{r}_2$, respectively)

$$\tilde{r}_1(f_{\rm AF}^{\rm cal}) = \zeta_1 G_1(f_{\rm GW}^{\rm cal})\tilde{x}_0(f_{\rm GW}^{\rm cal}), \tag{6.71}$$

$$\tilde{r}_2(f_{\rm AF}^{\rm cal}) = \zeta_2 G_2(f_{\rm GW}^{\rm cal})\tilde{x}_0(f_{\rm GW}^{\rm cal})\,\mathrm{e}^{-\mathrm{i}\phi_{\rm rel}}, \tag{6.72}$$

where $\phi_{\rm rel}$ represents the tunable relative phase by the phase shifter. The terms ζ_i and $G_i(f)$ are the net transimpedance from the photocurrent to the AF signal, and

the interferometer response to the gravitational wave, respectively ($i = 1, 2$). When the net relative phase vanishes at $f_{\rm AF}^{\rm cal}$ with the phase tuning, the following relation is satisfied:

$$\arg\left[\tilde{r}_1(f_{\rm AF}^{\rm cal})\right] = \arg\left[\tilde{r}_2(f_{\rm AF}^{\rm cal})\right], \tag{6.73}$$

in other words,

$$\phi_{\rm rel} = \arg\left[G_2(f_{\rm GW}^{\rm cal})\right] - \arg\left[G_1(f_{\rm GW}^{\rm cal})\right]. \tag{6.74}$$

In order to restore the original frequency component $\tilde{x}_0$ from $\tilde{r}_2$, we again compensate $\phi_{\rm rel}$ in the data reduction scheme as described later.

Antialiasing filter

The frequency response function of each antialiasing filter before the data acquisition sysmtem is approximated by

$$F_{\rm a}(f) = \frac{100}{1 + {\rm i}f/(f_c Q) - (f/f_c)^2} \cdot \frac{1}{1 + {\rm i}f/250\ {\rm kHz}}, \tag{6.75}$$

where $f_c = 29.24$ kHz and $Q = 0.487$.

6.3.2 Estimation of the cross correlation

The observation is done on 17 September 2007 (Japan standard time) at Mitaka, Japan. The data acquisition system[4] samples the AF1 and AF2 simultaneously at 215 kS/s (kilo-samples per second). The data record used for the cross-correlation analysis is divided into $\mathcal{N} = 439$ segments. Each segment contains $N = 2^{19}$ points. Thus the observation time inteval is $T = 1070.5$ seconds.

Power spectrum density

Each segment is divided into $\mathcal{N}_{\rm sub} = 64$ subsegments. Thus each subsegment contains $M = 8192$ points of raw data $r_i[k]$, where $i = 1, 2$ and $k = 1, 2, \ldots M$. For each subsegment, the mean of the subsegment is removed from the data. Then the data are Hanning windowed. After that, the subsegment is zero-padded[5] so that the length of the subsegment doubles. Then the (mean removed) raw data $r_i[k]$ reduces to

$$r_i'[k] = \begin{cases} w[k]\, r_i[k] & (k = 1, 2, \ldots, M) \\ 0 & (k = M+1, \ldots, 2M) \end{cases}, \tag{6.76}$$

where $w[k]$ is the Hanning window function [61]:

$$w[k] = 0.5 - 0.5\cos(2\pi(k-1)/M). \tag{6.77}$$

[4] National Instruments Co., PCI-6143

[5] The zero-padding doubles the frequency resolution of DFT (say, from 1 Hz to 0.5 Hz). This scheme prevents the wrap-around effect for the calculation of cross-correlation function [61].

Then the discrete Fourier transform (DFT) of the data $\{r_i'[k]\}$ is

$$X_i[f_k] = \delta t \sqrt{\tfrac{8}{3}} \sum_{n=1}^{2M} r_i'[n] \exp\left(-\mathrm{i}\frac{2\pi k(n-1)}{2M}\right), \tag{6.78}$$

where $\delta t = 1/215000$ is the sampling time interval, $\sqrt{8/3}$ recovers the signal loss with the Hanning window [61, 67], and the discrete frequencies are

$$f_k = \frac{1}{\delta t}\frac{k}{2M} = k\delta f. \tag{6.79}$$

The one-sided power spectrum density per unit freuqnecy intervel of the strain sensitivity (corresponds to the illustrations in Figure 5.20) is estimated as

$$P_i[f_k^{\mathrm{GW}}] = 2\frac{1}{N\delta t}\sum_{n=1}^{\mathcal{N}_{\mathrm{sub}}} \frac{\left|X_i^{(n)}[f_k]\right|^2}{\left|R_i(f_k^{\mathrm{GW}})\right|^2}\frac{1}{\left|F_{\mathrm{a}}(f_k)\right|^2}, \tag{6.80}$$

where

$$f_k^{\mathrm{GW}} = f_k + f_{\mathrm{RF}} + f_{\mathrm{LO2}}, \tag{6.81}$$

and the superscript (n) of X_k indicates the data from the n-th subsegment, $F_{\mathrm{a}}(f)$ is the antialiasing filter in Eq.(6.75), $N = M\mathcal{N}_{\mathrm{sub}}$, and $R_i(f)$ is the calibration function of each interferometer $(i = 1, 2)$.

The calibration functions are formed in the same manner as section 5.3; the difference is that the raw signal here is at f_{AF}, not f_{IF}. They are

$$R_1(f) = \frac{V_{\mathrm{AF1}}^{\mathrm{cal}}}{V_{\mathrm{pc}}}\frac{G_1(f)}{|G_1(f_{\mathrm{GW}}^{\mathrm{cal}})|}\frac{1}{A_{\mathrm{pc}}(f_{\mathrm{GW}}^{\mathrm{cal}})}C_{\mathrm{pc}}(f_{\mathrm{GW}}^{\mathrm{cal}}), \tag{6.82}$$

$$R_2(f) = \frac{V_{\mathrm{AF2}}^{\mathrm{cal}}}{V_{\mathrm{pc}}}\frac{G_2(f)}{|G_2(f_{\mathrm{GW}}^{\mathrm{cal}})|}\frac{1}{A_{\mathrm{pc}}(f_{\mathrm{GW}}^{\mathrm{cal}})}C_{\mathrm{pc}}(f_{\mathrm{GW}}^{\mathrm{cal}})\,\mathrm{e}^{-\mathrm{i}\phi_{\mathrm{rel}}}, \tag{6.83}$$

where $V_{\mathrm{AF}i}^{\mathrm{cal}}$ is the converted calibration peaks at $f_{\mathrm{AF}}^{\mathrm{cal}}$ for IFO-i, ϕ_{rel} is derived in Eq.(6.74), and

$$f_{\mathrm{GW}}^{\mathrm{cal}} = f_{\mathrm{AF}}^{\mathrm{cal}} + f_{\mathrm{RF}} + f_{\mathrm{LO2}}. \tag{6.84}$$

The converted calibration peaks $V_{\mathrm{AF1}}^{\mathrm{cal}}$ and $V_{\mathrm{AF2}}^{\mathrm{cal}}$ are estimated from the beginning of the data record (about 60 seconds), where the calibration peaks at $f_{\mathrm{GW}}^{\mathrm{cal}}$ is applied to the PCs in the recycling cavities. The data record with the calibration peaks is not used for the computation of the power spectrum densities (and cross-spectrum densiy described below). The response function $G_i(f)$ is formally derived in Eq.(3.52) as $G_{\mathrm{sync}}(f)$. For each interferometer, the resonant frequency $\nu_{\mathrm{FSR}(i)}$ and the finesse $\mathcal{F}_i$ is estimated in Figure 5.19. Note that

$$r_{\mathrm{r}}r_{\mathrm{c}} \simeq 1 + \frac{1}{2}\left(\frac{\pi}{\mathcal{F}}\right)^2 - \frac{1}{2}\frac{\pi}{\mathcal{F}}\sqrt{4 + \left(\frac{\pi}{\mathcal{F}}\right)^2} \tag{6.85}$$

from Eq.(3.55).

Optimal filter

The optimal filter is defined in Eq.(6.62) for the continuous frequency. The optimal filter $\tilde{Q}(f)$ contains the desired signal $\Omega_{\rm gw}(f)$ itself. Thus we assume the form of the desired signal [35, 46, 51]:

$$\Omega_{\rm gw}(f) \propto f^{\alpha}, \tag{6.86}$$

where the index α is expected to be order of unity. Assume that the gravitational-wave detector has a signal bandwidth Δf around a center frequency $f_0 \sim 100$ MHz, and the signal bandwidth is narrow such that the following approximation (Taylor expantion) is valid:

$$\Omega_{\rm gw}(f_0 + \Delta f) \propto {f_0}^{\alpha} \left(1 + \alpha \frac{\Delta f}{f_0}\right). \tag{6.87}$$

Then $\Omega_{\rm gw}(f)$ is considered to be a constant for the calculation of the optimal filter, because our detector has the bandwidth of $\Delta f \sim 1$ kHz, and thus $\alpha \Delta f / f_0 \ll 1$ is satisified[6].

As a result, we use the following form [51]:

$$\tilde{Q}(f) = \mathcal{K} \frac{\gamma_{12}(f)}{|f|^3 P_1(|f|) P_2(|f|)}, \tag{6.88}$$

where $\mathcal{K} \in \mathbb{R}$ is a real normalization constant. Then Eqs.(6.63) and (6.64) are written as

$$\mu_Z = \mathcal{K}\, \Omega_{\rm gw|100\ MHz} \frac{3H_0^2}{20\pi^2}\, 2 \int_{f_{\rm min}}^{f_{\rm max}} \frac{\gamma_{12}^2(f)}{f^6 P_1(f) P_2(f)}\, df, \tag{6.89}$$

$$\sigma_Z^2 = \frac{\mathcal{K}^2}{4T}\, 2 \int_{f_{\rm min}}^{f_{\rm max}} \frac{\gamma_{12}^2(f)}{f^6 P_1(f) P_2(f)}\, df. \tag{6.90}$$

The term $\Omega_{\rm gw|100\ MHz}$ is the normalized energy density per unit logarithmic frequency interval around 100 MHz. See Eq.(2.48) for the definition of $\Omega_{\rm gw}(f)$.

The normalization constant $\mathcal{K}$ is determined such that

$$\Omega_{\rm gw|100\ MHz} = \mu_Z \frac{20\pi^2}{3H_0^2}, \tag{6.91}$$

thus

$$\mathcal{K} = \left[2 \int_{f_{\rm min}}^{f_{\rm max}} \frac{\gamma_{12}^2(f)}{f^6 P_1(f) P_2(f)}\, df \right]^{-1}, \tag{6.92}$$

[6] Although the bandwidth of the interferomter is ~ 1 MHz as shown in Figure 5.19, here we use a bandwidth of ~ 1 kHz for the analysis.

and

$$\sigma_Z^2 = \frac{\mathcal{K}}{4T}. \tag{6.93}$$

In our experiment, the reduced overlap reduction function $\gamma_{12}(f)$ is almost constant at around 100 MHz $\pm$1 kHz, thus $\gamma_{12}(100\ \mathrm{MHz}) \simeq 0.93$ is used in this analysis. As shown in Figure 5.1, two interferometers are co-aligned and almost co-located, and the distance between the RM1 and the RM2 is about 10 cm.

The discrete-frequency representations of Eqs.(6.90), (6.92), and (6.88) are

$$\hat{\sigma}_Z^2 = \frac{\hat{\mathcal{K}}}{4N\delta t}, \tag{6.94}$$

$$\hat{\mathcal{K}} = \left[2\,\delta f \sum_{k=k_{\min}}^{k_{\max}} \frac{\left(\gamma_{12}\left[f_k^{\mathrm{GW}}\right]\right)^2}{\left(f_k^{\mathrm{GW}}\right)^6 P_1\left[f_k^{\mathrm{GW}}\right] P_2\left[f_k^{\mathrm{GW}}\right]} \right]^{-1}, \tag{6.95}$$

$$\tilde{Q}[f_k] = \hat{\mathcal{K}} \frac{\gamma_{12}\left[f_k^{\mathrm{GW}}\right]}{\left(f_k^{\mathrm{GW}}\right)^3 P_1\left[f_k^{\mathrm{GW}}\right] P_2\left[f_k^{\mathrm{GW}}\right]} \tag{6.96}$$

where $k_{\max}$ and $k_{\min}$ correspond to $f_k \simeq 2.08$ kHz and $f_k \simeq 4.19$ kHz, respectiverly.

Cross-correlation estimate

The cross-correlation estimate is calculated as follows.

The mean of the segment is removed. The segment is not windowed[7], but zero-padded such that the length of the segment doubles. Then the (mean-remoced) raw data reduces to

$$r_i''[k] = \begin{cases} r_i[k] & (k = 1, 2, \ldots N) \\ 0 & (k = N+1, \ldots 2N) \end{cases}. \tag{6.97}$$

The DFT of the segment is

$$Y_i[f_k''] = \delta t \sum_{n=1}^{2N} r_i''[n] \exp\left(-\mathrm{i}\frac{2\pi k(n-1)}{2N}\right) \tag{6.98}$$

with the frequency resolution of $f_{k+1}'' - f_k'' = \delta f'' = 1/(2\delta t N)$. The cross-spectrum density (raw) estimate is

$$C_k = \left[\frac{Y_1[f_k'']}{R_1(f_k''^{\mathrm{GW}})F_{\mathrm{a}}(f_k'')}\right]^* \left[\frac{Y_2[f_k'']}{R_2(f_k''^{\mathrm{GW}})F_{\mathrm{a}}(f_k'')}\right]. \tag{6.99}$$

[7] Instead of windowing, the frequency binning is performed [61]. Neverthless the windowing would be required if the data have a large dynamic range as for the low-frequency interferometer [68]; there would be electrical line noises (they are integer times 50 Hz in the eastern part of Japan) and so on.

The frequency resolution of C_k reduces to that of $P_i[f_k]$ and $\tilde{Q}[f_k]$ with the following frequency-binning scheme. The component of C_k is averaged every frequency interval: $N_{\rm seg}\delta f$. Then the frequency-binned cross-spectrum density estimate is

$$C_{12}[f_k] = \frac{1}{\mathcal{N}_{\rm sub}} \sum_{l=l_{\rm min}}^{l_{\rm max}} C_l, \qquad (k = 0, 1, \dots) \tag{6.100}$$

where $l_{\rm min} = k\mathcal{N}_{\rm sub}$ and $l_{\rm max} = (k+1)\mathcal{N}_{\rm sub} - 1$. Now $C_{12}[f_k]$ corresponds to the *two-sided* cross-spectrum density per unit frequency interval.

From Eq.(6.51), the cross-correlation estimate of each segment is calculated as follows:

$$\hat{Z}_{12} = \frac{1}{N\delta t}\, 2\,{\rm Re}\left[\delta f \sum_{k=k_{\rm min}}^{k_{\rm max}} C_{12}[f_k]\tilde{Q}[f_k]\right]. \tag{6.101}$$

Ensemble average of the estimators

The ensemble average is approximated by taking a mean of the corss correlation estimated from each segment. The mean is a kind of weighted average over all observation time interval $T = \mathcal{N}N\delta t$ as follows [69]:

$$\hat{\mu}_Z = \frac{\displaystyle\sum_{n=1}^{\mathcal{N}} \frac{\hat{Z}_{12}^{(n)}}{\hat{\sigma}_Z^{2(n)}}}{\displaystyle\sum_{n=1}^{\mathcal{N}} \frac{1}{\hat{\sigma}_Z^{2(n)}}}, \tag{6.102}$$

where (n) indicates the quantity of the n-th segment. If all $\hat{\sigma}_Z^{2(n)}$ are identical, the above equation reduces to

$$\hat{\mu}_Z = \frac{1}{\mathcal{N}} \sum_{n=1}^{\mathcal{N}} \hat{Z}_{12}^{(n)}. \tag{6.103}$$

A noisy interval would have a large $\hat{\sigma}_Z^2$, thus the contribution to $\hat{\mu}_Z$ form such a noisy interval is reduced by the weighting. At the same time, the uncertainty in the estimation is calculated as

$$\hat{\sigma}_\mu^2 = \left[\sum_{n=1}^{\mathcal{N}} \frac{1}{\hat{\sigma}_Z^{2(n)}}\right]^{-1}. \tag{6.104}$$

If the uncertainty in each interval is identical, the above equation reduces to

$$\hat{\sigma}_\mu^2 = \frac{\hat{\sigma}_Z^2}{\mathcal{N}}. \tag{6.105}$$

After the $T = 1070.5$ seconds observation, the cross-correlation of the two interferometer outputs is estimated as

$$\hat{\mu}_Z = 4.9 \times 10^{-12}, \tag{6.106}$$

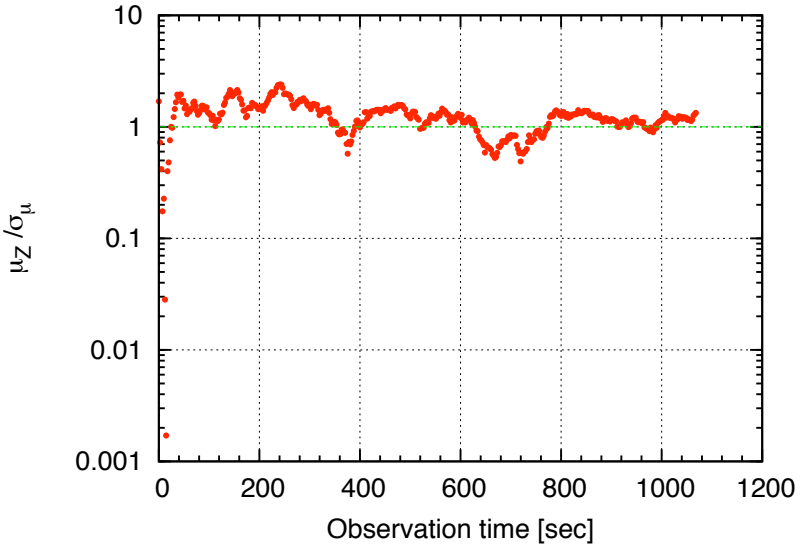

Figure 6.3 Estimation of SNR: $\widehat{\mathrm{SNR}} \equiv |\hat{\mu}_Z|/\hat{\sigma}_\mu$ (shown as the red filled circles). The green dashed line represents SNR = 1. Because the SNR is nearly unity after $T \simeq 1000\,\mathrm{sec}$ observation and does not seem to increase proportional to $\sqrt{T}$, we could say that the cross-correlataion estimate $\hat{\mu}_Z$ is still dominated by uncorrelated noises.

and the standard deviation of the estimate is estimated as

$$\hat{\sigma}_\mu = 3.7 \times 10^{-12}. \tag{6.107}$$

Variation of an estimated SNR ($\widehat{\mathrm{SNR}} \equiv |\hat{\mu}_Z|/\hat{\sigma}_\mu$) with respect to the observation time are shown in Figure 6.3 as red filled circles. The green dashed line represents SNR = 1. The estimated SNR is nearly unity even after $T \simeq 1000\,\mathrm{sec}$ observation, and does not seem to increase proportional to $\sqrt{T}$. Thus we could say that the cross-correlataion estimate $\hat{\mu}_Z$ is still dominated by uncorrelated noises. Moreover, Figure 6.4 shows the corss-correlation estimate with respect to the observation time. Estimations of $\hat{\mu}_Z$ are shown as the red filled circles. The black curves enclose the two-sided 90% confidence interval of μ_Z:

$$[\hat{\mu}_Z - 1.65\hat{\sigma}_\mu,\ \hat{\mu}_Z + 1.65\hat{\sigma}_\mu]. \tag{6.108}$$

After 1000 sec observation, the 90% confidence interval still includes $\mu_Z = 0$; thus we cannot declare that the gravitational-wave background induces $\hat{\mu}_Z$. Instead, we estimate an upper limit on the amounts of the energy density of the gravitational-wave background. Note that the uncertainty $\hat{\sigma}_\mu$ decreases as $1/\sqrt{T}$, even though the SNR remains nearly unity.

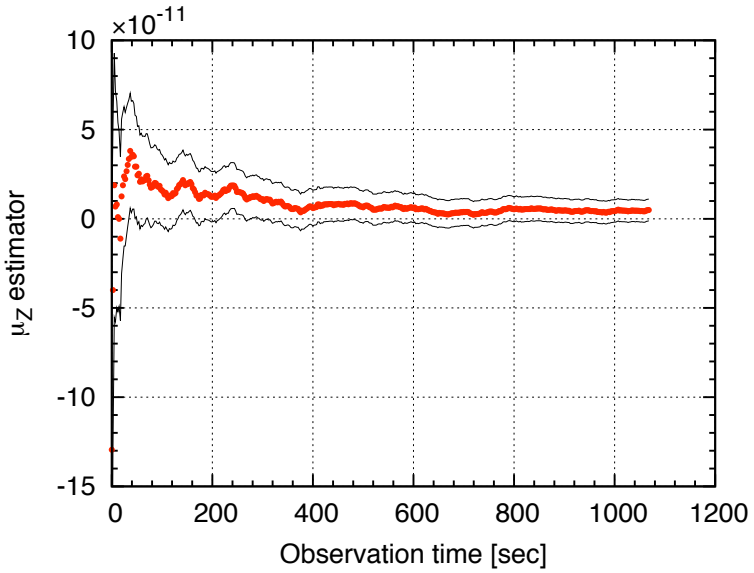

Figure 6.4 Estimation of $\hat{\mu}_Z$ (shown as the red filled circles). The two-sided 90% confidence interval is the region enclosed by the black curves. The uncertainty $\hat{\sigma}_\mu$ decreases as $1/\sqrt{T}$, where T is the observation time (horizontal axis), even though the SNR remains nearly unity (see Figure 6.3)

6.3.3 Upper limit on the gravitational-wave background at 100 MHz

From Eq.(6.91) and (2.43), one finds

$$h_0^2\hat{\Omega}_{\mathrm{gw}|100\ \mathrm{MHz}} = \hat{\mu}_Z \frac{20\pi^2}{3(H_0/h_0)^2} \tag{6.109}$$

$$= 3.0 \times 10^{+25} \tag{6.110}$$

with the standard deviation of

$$\hat{\sigma}_\Omega = \hat{\sigma}_\mu \frac{20\pi^2}{3(H_0/h_0)^2} \tag{6.111}$$

$$= 2.3 \times 10^{+25}. \tag{6.112}$$

Note that the calculations are for $h_0^2\Omega_{\mathrm{gw}}(f)$, not for $\Omega_{\mathrm{gw}}(f)$.

We define the upper limit of $h_0^2\Omega_{\mathrm{gw}}(f)$ at around 100.1 MHz as the one-sided 90% confidence level [51]. Then the upper limit is estimated as

$$h_0^2\hat{\Omega}_{\mathrm{gw}|100\ \mathrm{MHz}} + 1.28\hat{\sigma}_\Omega \simeq 6.0 \times 10^{+25}. \tag{6.113}$$

Apart from $\hat{\sigma}_\mu^2$, the calibration process would have an uncertainty of $\sim 10\%$, which comes from the modulation efficieny of each Pockels cell inserted in the recycling

cavity (PC1 or PC2). There are two interferometers with such uncertainties, then each uncertainty contributes to the uncertainty of the cross-correlation estimate. Therefore the upper limit would have an uncertatinty of 20%; the result is

$$h_0^2\Omega_{\mathrm{gw}|100\ \mathrm{MHz}} < (6.0 \pm 1.2) \times 10^{+25}. \tag{6.114}$$

6.3.4 Frequency components of the estimation

The strain sensitivity of each interferometer is estimated from their power spectrum density. For each interferoemter, the ensemble average over the observation time gives a smooth spetrum. From Eq.(6.80), the ensemble averaged one-sided power spectrum density is calculated as

$$\hat{P}_i[f_k^{\mathrm{GW}}] = \frac{1}{\mathcal{N}} \sum_{n=1}^{\mathcal{N}} P_i^{(n)}[f_k]. \tag{6.115}$$

Figure 6.5 shows the $\sqrt{\hat{P}_1[f_k^{\mathrm{GW}}]}$ and $\sqrt{\hat{P}_2[f_k^{\mathrm{GW}}]}$ for the strain sensitivity of IFO-1 and IFO-2, respectively. For the analyzed frequency range, they are

$$\sqrt{\hat{P}_1} \simeq 1.09 \times 10^{-16}\ \mathrm{Hz}^{-1/2}, \tag{6.116a}$$

$$\sqrt{\hat{P}_2} \simeq 1.44 \times 10^{-16}\ \mathrm{Hz}^{-1/2}\,. \tag{6.116b}$$

respectively. They are worse than the illustrations in Figure 5.20. This would be caused by the demodulation scheme from the IF signal to the AF signal. When the 2nd LO is mixed with the IF signal, the noises from the lower sideband of the 2nd LO, that is, the frequency component of $f_{\mathrm{LO2}} - f_{\mathrm{IF}}$ contaminates the AF signals. With single sideband demodulators for the frequency conversion, this noise would be expected to be suppressed.

The noise-equivalent cross-correlation is defined such that the power SNR in Eq.(6.65) is unity. Consider that $\Omega_{\mathrm{gw}}(f)$ =const, $\gamma_{12|100\,\mathrm{MHz}} \simeq 0.93$, $P_1(f) = \hat{P}_1$, and $P_2(f) = \hat{P}_2$ in the integrand of Eq.(6.65). For the observation time $T \simeq 1000$ seconds, and the observation bandwidth $\Delta f_{\mathrm{obs}} \simeq 2$ kHz, the noise-equivalent cross-correlation should be

$$\mu_Z^{\mathrm{noise}} \simeq \frac{1}{2\sqrt{T}} \frac{f^3\sqrt{\hat{P}_1\hat{P}_2}}{|\gamma_{12}|\sqrt{\Delta f_{\mathrm{obs}}}} \tag{6.117}$$

$$\simeq 5 \times 10^{-12}, \tag{6.118}$$

which is consistent with Eq.(6.106). From Eq.(2.50), μ_Z^{noise} corresponds to

$$h_{\mathrm{rms}}(f) \simeq \sqrt{\frac{5\mu_Z^{\mathrm{noise}}}{f^3}} \simeq 5 \times 10^{-18}\ \mathrm{Hz}^{-1/2}\,. \tag{6.119}$$

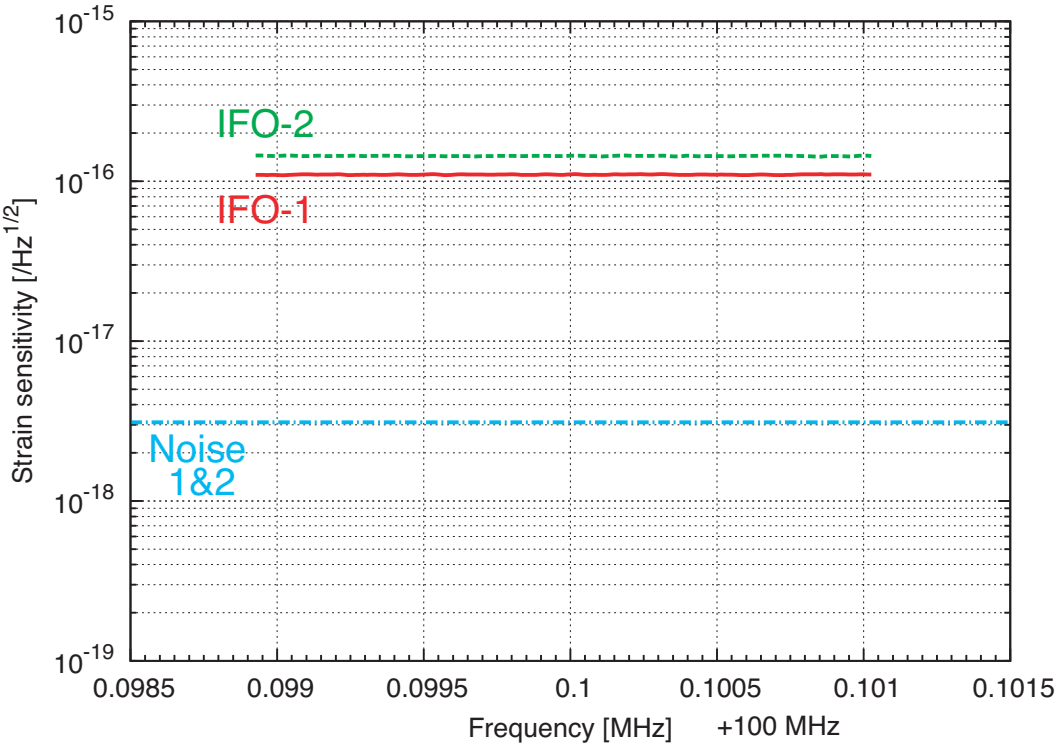

Figure 6.5 Ensemble averaged amplitude spectrum densities of the interferometer noises. The vertical axis represents the strain sensitivity in the unit of $\mathrm{Hz}^{-1/2}$. The horizontal axis represents the gravitational-wave frequency, which is offset by 100 MHz (for example, "0.1 MHz" means 100.1 MHz). The red solid and green dashed lines are the amplitude spectrum densities of IFO-1 and IFO-2, respectively. The light blue dash-dotted line (Noise 1&2), which shows the improvement of the estimation owing to the cross-correlation analysis, is calculated from the red and green lines with the assumption that the interferometer outputs are dominated by uncorrelated noises.

Form Eq.(3.109), μ_Z^{noise} is represented in the strain sensitivity:

$$h_{\mathrm{sn}}(f) \simeq \sqrt{\frac{2\,\gamma_0(f)\mu_Z^{\mathrm{noise}}}{f^3}} \simeq 3 \times 10^{-18}\ \mathrm{Hz}^{-1/2}, \tag{6.120}$$

which is shown in Figure 6.5 as a light blue dash-dotted line ("Noise 1&2").

Chapter 7

Discussions and future works

7.1 Interferometers

For each interferometer, the strain sensitivity to gravitational waves is esimated from the IF signal as shown in Figure 5.20. The amounts of the noise is larger than the calculation shown in Figure 4.8. The amouts of the light field at the antisymmetric port (dark port) is about 15 mW, which is sufficient so that the noise in the AP photodetector is dominated by the shot noise of the light field at the dark port. On the other hand, the amout of 1st LO would not be sufficient. The beamsplitter in each interferometer is now a standard aviable beamsplitter, which has a splitting ratio of nominal 50%/50%. Thus in principle, the 1st LO vanishes at the dark port as well as the carrier. The amount of the junk light, which would arise from the mode mismatch between the incident laser light and the recycling cavity and so on, would appear at the dark port. The junk light does not contribute to the extraction of desired signal (of gravitational waves), and become a noise source. If the amount of 1st LO is not sufficient to overtake the noise caused by the junk light, the resultant sensitivity would get worse. The amount of the 1st LO is expected to increase by replacing the beamsplitter with a partial reflector, which has an asymmetric beamsplitting ratio, but note that a photodiode can not recieve too much amount of light. The suitable asymmetry would be about 55%/45%.

The actual free-spectral range of the recycling cavity is different from the design frequency of 101.6 MHz. The difference is about 1.5%, which corresponds to 7.5 mm with respect to the baseline length 75 cm. The design does not considers the refractive index of the Pockels cell in the recycling cavity. The Pockels cell is a lithium niobate ($LiNbO_3$) crystal with a size of $4 \times 4 \times 40$ mm. A lithium niobate has a refractive index of ~ 2.2, thus if the cavity is formed as the design, the free-spectral range would be 99.97 MHz. Moreover, the resonant frequency of the recycling cavity could not be precisely decided from the fitting in Figure 5.19. Now the cavity is constructed in air, thus the finesse of the cavity is low. Then the ambiguity of the resonant frequency would not largely contribute to the cross-correlation estimate. We have a future plan to construct the interferometers in vacuum, where the finesse of the cavity

would be improved. Thus controlling the absolute-length of the cavity (for example see Refs. [55, 56]) will be required,[1].

The calibration scheme will need more improvement. Now we are using the Pockels cell, with which the finesse of the recycling cavity gets down. In order to achieve higher finesse, another way of imitating gravitational-wave at 100 MHz must be developed.

7.2 Cross-correlation analysis

For each interferometer, the strain sensitivity to gravitational waves is esimated from the AF signal as shown in Figure 6.5. The amounts of the noise is larger than the estimation in Figure 5.20.

The conversion scheme from the IF signal to the AF signal increases the noise by $\sqrt{2}$ times in the term of strain sensitivity. This is caused by the lower sideband of the 2nd LO, which converts the IF signal into the AF signal. The desired IF signal corresponds to the upper sideband of the 2nd LO, thus the 2nd LO converts both upper and lower sidebands into the AF signal. Then from the strain sensitivity estimated from AF signal [see Eq.(6.116)] the IF signal should be 7.71×10^{-17} Hz$^{-1/2}$ for IFO-1, and 1.02×10^{-16} Hz$^{-1/2}$ for IFO-2. The illustrations in Figure 5.20 are almost consistent with theses estimations at 100.1 MHz. In order to take out only the desired signal, we would need a single sidenband demodulator.

The cross-correlation estimate in Eq.(6.106) is consistent with the noise-equaivalent estimate in Eq(6.106). In other words, we could say that the integration time interval (or observation time interval) seems not sufficient for the actural observation of the gravitational waves, and the interferometer noises are independent at this noise level. The signal-to-noise ratio (SNR) of the cross-correlation estimate increases proportional to the square root of the integration time interval. For the improvement of the SNR by one order of magnitude, the required integration time is 10^5 seconds, that is, about one day. The one-year observation will improve the SNR by about 176 times with respect to the 1000 seconds observation.

The relative phase of the AF2 signal to the AF1 signal is tuned to vanish with the phase shifter for the 2nd LO supplied to IFO-2. It is now tuned manually. If there is a "standard star" of gravitational waves (at 100 MHz), we could tune the relative phase such that the correlation signal is maximized in the data reduction scheme as well as by manual tuning. In fact, the realistic way of tuning or confirmation of the relative phase would be testing possible values of $\phi_{\rm rel}$ in the data analysis scheme.

The correlation analysis uses a non-overlapping estimates for the cross-spectrum density. The uncertainty in the estimation procedure is expected to decrease with the overlapping procedures [67], which is used in the search for a low-frequency gravitational wave [70]. The overlapping recovers the effective loss of observation time caused by the windowing.

[1] In fact, we are considering such a control scheme based on Ref. [56].

Chapter 8

Conclusion

We searched directly for a stochastic background of gravitational waves at 100 MHz using laser interferometry.

We have developed a laser-interferometric gravitational-wave detector, which is a pair of 75-cm baseline synchronous recycling interferometers. Although the concept of the synchronous recycling technique was proposed in 1980s, this is the first construction of the interferometer for actual use. Moreover, this is the first laser-interferometric detector for 100-MHz gravitational waves.

The synchronous recycling interferometer has an advantage for the detection of gravitational waves at such very high frequencies; the interferometer has a resonant resoponse at a specific frequency (in our case, the 75-cm baseline correpsonds to a 100-MHz resonance), and the interferometer can be more sensitive at the frequency than a standard laser-interferometric gravitational-wave detector based on a Michelson interferometer.

Each interferometer was locked to its operation point by the Pound-Drever-Hall technique, which is generally used for laser interferometry. On the other hand, we have developed a scheme to extract gravitational-wave signals from the interferometer; the gravitational-wave signals are converted into intermediate-frequency electrical signals by an optical heterodyne technique, and the intermediate-frequency signals are converted into recordable low-frequency signals by an electrical heterodyne technique.

For each interferometer, we achieved a strain sensitivity of $\sim 10^{-16}\,\mathrm{Hz}^{-1/2}$, which is the highest signal-to-noise ratio for gravitational waves at around 100 MHz today. Using both interferometers, we directly searched for a stochastic background of gravitational waves centered at 100.1 MHz with a narrow (2 kHz) bandwidth in 1070.5 seconds. In order to improve the signal-to-noise ratio of this search, we performed a corss-correlation analysis of the outputs of two interferometers.

Thus, as the first step of the direct search, we find a one-sided 90% confidence upper limit of $h_0^2\Omega_{\mathrm{gw}}(100\ \mathrm{MHz}) < (6.0 \pm 1.2) \times 10^{+25}$ on the energy density of the gravitational-wave background.

Appendix A

Michelson interferometer

This chapter describes the shot-noise-limted strain sensitivity of a Michelson interferometer.

Consider a Michelson interferometer illustrated in Figure A.1. Here the one-way length of each arm is L; the amplitude reflectance of the beamsplitter (BS) is $+1/\sqrt{2}$ for the symmetric port (SP), and is $-1/\sqrt{2}$ for the antisymmetric port (AP); the amplitude transmittance of the BS is $1/\sqrt{2}$; the amplitude reflectance of each end mirror is 1.

A.1 Detection limit of the differential phase fluctuation

Consider the incident light filed is $E_{\rm inc}\mathrm{e}^{\mathrm{i}\Omega_0 t}$. Then the light field appears at the AP is

$$E_{\rm AP} = \tfrac{1}{2}\left(\mathrm{e}^{-\mathrm{i}\phi_2} - \mathrm{e}^{-\mathrm{i}\phi_1}\right) E_{\rm inc} \tag{A.1}$$

$$= -\mathrm{i}\mathrm{e}^{-\mathrm{i}\frac{\phi_+}{2}} \sin\left(\tfrac{\phi_-}{2}\right) E_{\rm inc}, \tag{A.2}$$

where ϕ_1, ϕ_2 is the round-trip phases for the inline arm and the perpendicular arm, respectively, and

$$\phi_+ \equiv \phi_2 + \phi_1 \tag{A.3}$$

$$\phi_- \equiv \phi_2 - \phi_1. \tag{A.4}$$

If the dark fringe condition is satisfied at the AP, the differential phase becomes

$$\phi_-(t) = 2\pi k + \delta\phi_- \cos(\omega t), \tag{A.5}$$

where k is an integer. Then the light field at the AP is written as

$$E_{\rm AP} = \mathrm{i}E_{\rm inc}\mathrm{e}^{-\mathrm{i}\varphi}\,\frac{\delta\phi_-}{2}\cos(\omega t), \tag{A.6}$$

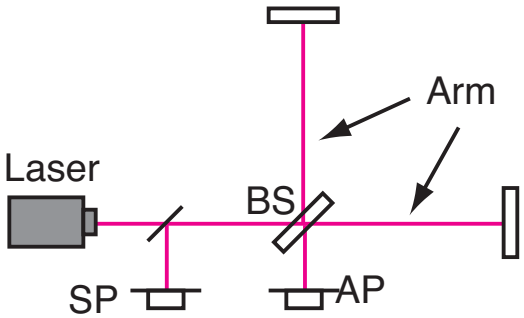

Figure A.1 Michelson interferometer.

where φ is an arbitrary phase.

Even if the light field at the AP is directly detected, one cannot obtain a photocurrent proportional to $\delta\phi_- \cos(\omega t)$. Instead, let us prepare an optical local oscillator $E_{\rm LO}e^{i\Omega_0 t}$ with a certain relative phase such that the light field at the AP is written as

$$E_{\rm AP} = E_{\rm LO}e^{-i\varphi} + iE_{\rm inc}e^{-i\varphi}\,\frac{\delta\phi_-}{2}\cos(\omega t). \tag{A.7}$$

Now consider that the relative phase of the optical local oscillator satisfies

$$\arg\left(E_{\rm LO}/E_{\rm inc}\right) = -\pi/2. \tag{A.8}$$

Then the time-averaged power of the light field is written as

$$\bar{P}_{\rm AP} \simeq \bar{P}_{\rm LO} + \sqrt{\bar{P}_{\rm LO}\bar{P}_{\rm inc}}\,\delta\phi_- \cos(\omega t). \tag{A.9}$$

The AP photodiode recieves this light and products the photocurrent:

$$i_{\rm AP} = \frac{\eta e}{\hbar\Omega_0}\left(\bar{P}_{\rm LO} + \sqrt{\bar{P}_{\rm LO}\bar{P}_{\rm inc}}\delta\phi_- \cos(\omega t)\right) \tag{A.10}$$

$$= i_{\rm dc} + i_{\rm sig}\cos(\omega t). \tag{A.11}$$

Thus the transfer function from the differential phase fluctuation $\delta\phi_-$ to the signal current $i_{\rm sig}$ is

$$\frac{i_{\rm sig}}{\delta\phi_-} = \frac{\eta e}{\hbar\Omega_0}\sqrt{\bar{P}_{\rm LO}\bar{P}_{\rm inc}}. \tag{A.12}$$

The differential phase fluctuation corresponding to the shot noise[1] $\sqrt{2\,e\,i_{\rm dc}}$ is

$$\delta\phi_-^{\rm shot} = \sqrt{\frac{2\hbar\Omega_0}{\eta\bar{P}_{\rm inc}}} \tag{A.13}$$

in the unit of rad/$\sqrt{\rm Hz}$. From Eq.(A.13), one finds that the detection limit of the differential phase fluctuation for the Michleson interferometer is independent from the power of the local oscillator field $E_{\rm LO}$.

[1] Square root of the one-sided power spectrum density per unit frequency interval.

A.2 Shot-noise-limited strain sensitivity

Consider gravitational wave are incident on a Michelson interferometer in the vertical direction. From Eq.(3.8) the evolution of round-trip phase of the light in the inline arm is

$$\phi_1 = \frac{2\Omega_0 L}{c} + \frac{\Omega_0}{2}\int_{t-2L/c}^{t} h(t)\,dt \tag{A.14}$$

$$= \phi_0 + \delta\phi(t). \tag{A.15}$$

In the same manner, $\phi_2 = \phi_0 - \delta\phi(t)$. Substituting Eq.(3.14) into Eq.(A.15) yields

$$\delta\phi(t) = \int_{-\infty}^{\infty} H_{\rm MI}(f)\tilde{h}(f)\,\mathrm{e}^{\mathrm{i}2\pi f}\,df, \tag{A.16}$$

$$H_{\rm MI}(f) = \frac{\Omega_0}{\omega}\sin(\omega L/c)\mathrm{e}^{-\mathrm{i}\omega L/c}, \tag{A.17}$$

where $\omega \equiv 2\pi f$. Using the defintion: $\phi_- \equiv \phi_2 - \phi_1$, one finds

$$\frac{\delta\tilde{\phi}_-}{\tilde{h}}(f) = -2H_{\rm MI}(f). \tag{A.18}$$

From Eq.(A.13), the shot-noise-limited strain sensitivity of the Michelson interferometer is

$$h_{\rm shot}(f) = \sqrt{\frac{2\hbar\Omega_0}{\eta\bar{P}_{\rm inc}}}\,\frac{1}{2\,|H_{\rm MI}(f)|}. \tag{A.19}$$

Consider a gravitational wave at $\nu_{\rm g} = \omega_{\rm g}/(2\pi)$. In order to maximize $|H_{\rm MI}|$ at that frequency, the arm length should be

$$L = \frac{c}{4\nu_{\rm g}}, \tag{A.20}$$

and thus it yields

$$|H_{\rm MI}(f)| = \frac{\nu_0}{f}\left|\sin\left(\frac{\pi}{2}\frac{f}{\nu_{\rm g}}\right)\right|. \tag{A.21}$$

As a result, at the frequency of $f = \nu_{\rm g}$, the maximum is

$$|H_{\rm MI}^{\rm max}| = \frac{\nu_0}{\nu_{\rm g}}. \tag{A.22}$$

This equation states that $|H_{\rm MI}|$ decreases in the higher frequency as f^{-1}. Thus the Michelson interferometer would be inadequate for detecting very-high-frequency gravitational waves.

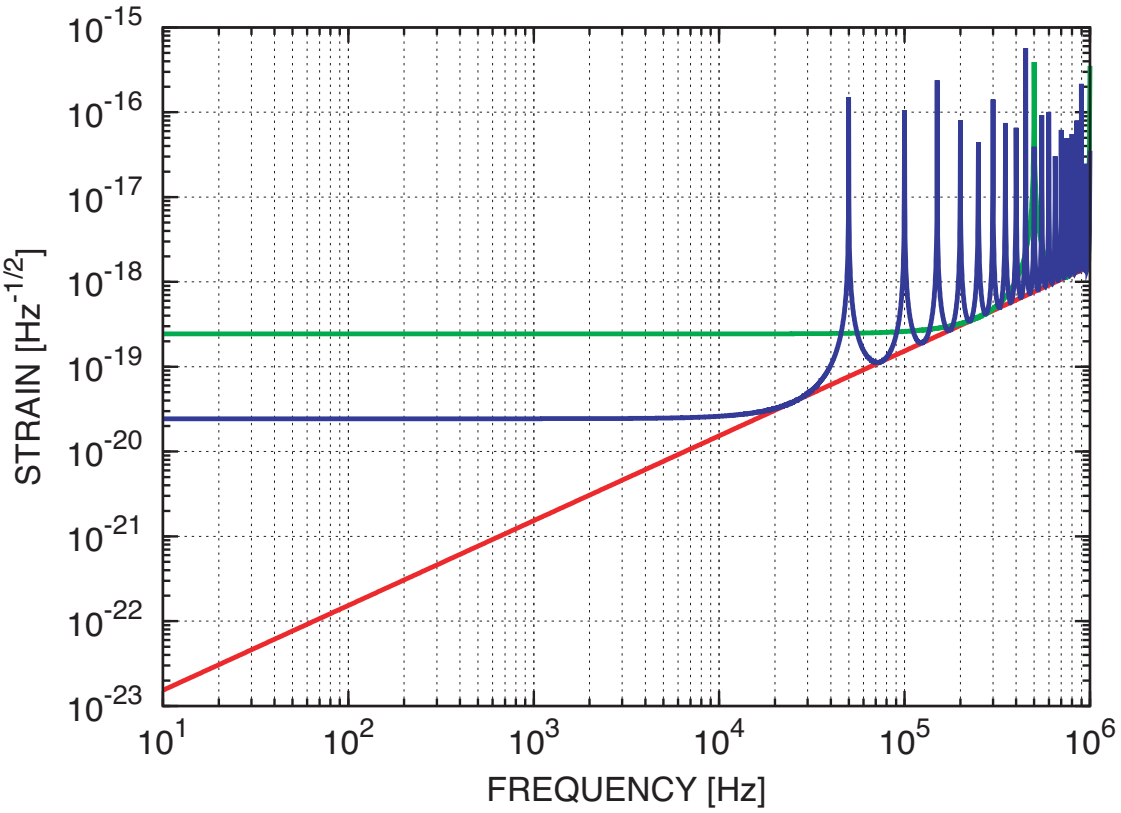

Figure A.2 Shot-noise-limited strain sensitivity of a Michleson interferometer. The red line represents the limit when the arm length L is optimized for each frequency. The green line represents the limit for a Michelson interferometer with $L = 300\,\mathrm{m}$ and the blue line for $L = 3\,\mathrm{km}$. The power of the incident light is $0.5\,\mathrm{W}$.

As a result, the shot-noise-limited sensitivity of a Michelson interferometer is

$$h_{\mathrm{shot}}(\nu_{\mathrm{g}}) = \sqrt{\frac{2\hbar\Omega_0}{\eta \bar{P}_{\mathrm{inc}}}}\,\frac{\nu_{\mathrm{g}}}{2\,\nu_0} \tag{A.23}$$

for each frequency ν_{g}. Figure A.2 shows the detection limit (strain sensitivity); the power of incident light is $\bar{P}_{\mathrm{inc}} = 0.5\,\mathrm{W}$. The vertical axis represents one-sided amplitude spectrum density[2] of the strain sensitivities, and the horizontal axis represents the frequency of the gravitatioanl wave. The red line plots Eq.(A.23). The green line is the plot for the case that the arm length is fixed at $L = 300\,\mathrm{m}$, and the blue line is for $L = 3\,\mathrm{km}$.

[2] Square root of one-sided spectrum density

A.3 Shot-noise-limited strain sensitivity with the frontal modulation scheme

This section describes the shot-noise-limted sensitivity of a practical Michelson interferometer; the interferometer is locked to the operational point (dark fringe at the AP) with the frontal modulation (or Schnupp modulation) scheme [54].

Before the laser light is incident on the interferometer, the RF sideband with a modulation depth of β is induced by the EOM. Then the incident light is represented by Eq.(4.7). The light field at the AP is written in the same form as Eq.(4.33), but the parameters are

$$a_0 = 0, \tag{A.24}$$

$$a_1 = -\mathrm{i}J_0(\beta)\frac{h}{2}H_{\mathrm{MI}}(\omega_{\mathrm{g}}) \tag{A.25}$$

$$a_{-1} = -a_1^*, \tag{A.26}$$

$$b_1 = J_1(\beta)\sin\left(\frac{\omega_{\mathrm{m}}\ell_-}{c}\right), \tag{A.27}$$

$$b_{-1} = -b_1^*. \tag{A.28}$$

Here ℓ_- is called the Schnupp asymmetry [54]. The photocurrent produced by the AP photodiode is

$$i_{\mathrm{AP}} = \frac{e\,\eta\bar{P}_{\mathrm{inc}}}{\hbar\Omega_0}\left(2|b_1|^2 + 8\mathrm{Im}\left[a_1\mathrm{e}^{\mathrm{i}\omega_{\mathrm{g}}t}\right]\mathrm{Im}\left[b_1 e^{\mathrm{i}\omega_{\mathrm{m}}t}\right] + \dots\right) \tag{A.29}$$

$$= i_{\mathrm{AP0}} + i_{\mathrm{AP1}}(t) + \dots, \tag{A.30}$$

where

$$i_{\mathrm{AP0}} \equiv \frac{e\,\eta\bar{P}_{\mathrm{inc}}}{\hbar\Omega_0}\,2|b_1|^2, \tag{A.31}$$

$$i_{\mathrm{AP1}} \equiv \frac{e\,\eta\bar{P}_{\mathrm{inc}}}{\hbar\Omega_0}\,8\mathrm{Im}\left[a_1\mathrm{e}^{\mathrm{i}\omega_{\mathrm{g}}t}\right]\mathrm{Im}\left[b_1 e^{\mathrm{i}\omega_{\mathrm{m}}t}\right]. \tag{A.32}$$

From Eq.(4.23), demodulating i_{AP1} at Q-phase yields

$$v_{\mathrm{Q}}(t) = \zeta\,\frac{1}{\Delta t}\int_{t-\Delta t}^{t} 8\mathrm{Im}\left[a_1\mathrm{e}^{\mathrm{i}\omega_{\mathrm{g}}t}\right]\mathrm{Im}\left[b_1 e^{\mathrm{i}\omega_{\mathrm{m}}t}\right]\cos(\omega_{\mathrm{m}}t + \pi/2)\,dt \tag{A.33}$$

$$\simeq \zeta\,4\mathrm{Re}\left[b_1\right]\mathrm{Im}\left[a_1\mathrm{e}^{\mathrm{i}\omega_{\mathrm{g}}t}\right] \tag{A.34}$$

$$= \zeta\,4J_1(\beta)\sin\left(\omega_{\mathrm{m}}\ell_-/c\right)\mathrm{Im}\left[a_1\mathrm{e}^{\mathrm{i}\omega_{\mathrm{g}}t}\right]. \tag{A.35}$$

Thus the response function is

$$\frac{\tilde{v}_{\mathrm{Q}}}{\tilde{h}}(f) = -g_{\mathrm{dem}}Z_{\mathrm{pd}}\frac{e\,\eta\bar{P}_{\mathrm{inc}}}{\hbar\Omega_0}\,2J_0(\beta)J_1(\beta)\sin\left(\omega_{\mathrm{m}}\ell_-/c\right)H_{\mathrm{MI}}(f). \tag{A.36}$$

If we do not consider the non-stationary shot noise, the shot noise before the demodulation is $\sqrt{2\,e\,i_{\rm AP0}}$. By the demodulation, the shot noise components in the photocurrent at $\omega_{\rm m} \pm \omega_{\rm g}$ seem to be added statistically ($= 2\sqrt{e\,i_{\rm AP0}}$), but this is also divided into halves[3] and converted into the signal at $\omega_{\rm g}$. Thus one finds

$$v_{\rm Q}^{\rm shot} = g_{\rm dem} Z_{\rm pd} \sqrt{e i_{\rm AP0}}. \tag{A.37}$$

in the unit of $\mathrm{V}/\sqrt{\mathrm{Hz}}$ (one-sided amplitude spectrum density). Thus the strain noise corresponding to the shot noise is

$$h_{\rm shot}(f) = \sqrt{\frac{2\hbar\Omega_0}{\eta \bar{P}_{\rm inc}}}\,\frac{1}{2\,|H_{\rm MI}(f)|}\,\frac{1}{J_0(\beta)}, \tag{A.38}$$

where $J_0(\beta)$ corresponds to the penalty function in Eq.(4.49). In the limit of $\beta \to +0$, that is, in the limit such that $J_0(\beta)^2 \bar{P}_{\rm inc}$ goes to $\bar{P}_{\rm inc}$, Eq.(A.38) reduces to Eq.(A.19).

Non-stationary shot noise. In the above discussion, we ignore the effect of the non-stationary shot noise. In the early prototype of laser interferometer [71], there is a discrepancy between the predicted shot noise and that observed. After various efforts [72, 73, 74, 75], one realized that a shot noise derives from the vacuum fluctuation[4], and that the excess noise is unavoidable if one uses the simple optical heterodyne. Eq.(A.38) should change slightly [77, 78]:

$$h_{\rm shot}(f) = \sqrt{\frac{2\hbar\Omega_0}{\eta \bar{P}_{\rm inc}}}\,\frac{\sqrt{3/2}}{2\,|H_{\rm MI}(f)|}\,\frac{1}{J_0(\beta)}. \tag{A.39}$$

[3] Note that: $\cos(\omega_{\rm m} t)\cos[(\omega_{\rm m}+\omega_{\rm g})t] = \frac{1}{2}\cos[\omega_{\rm g} t] + \frac{1}{2}\cos[(2\omega_{\rm m}+\omega_{\rm g})t]$. Only the former term at $\omega_{\rm g}$ is picked up by the demodulator.

[4] In other words, a shot noise derives from a quamtum mechanical effect. Now these efforts develop to a part of quantum optics; for example, Ref. [76] is a basic reference that treats laser-interferometric gravitational-wave detectors in a frame of quantum optics.

Appendix B

Fabry-Perot Michelson interferometer

This chapter describes the shot noise limted sensitivity of a Fabry-Perot Michelson interferometer.

Consider a Fabry-Perot Michelson interferometer with the following parameters: the one-way length of the Fabry-Perot cavity is L; the amplitude reflectance of the front mirror is r_{f}; the amplitude transmittance of the front mirror is t_{f}; the amplitude reflectance of each end mirror is r_{e}. The amplitude reflectance of the beamsplitter (BS) is $+1/\sqrt{2}$ for the symmetric port (SP) and $-1/\sqrt{2}$ for the antisymmetric port (AP). The amplitude transmittance of the BS is $1/\sqrt{2}$.

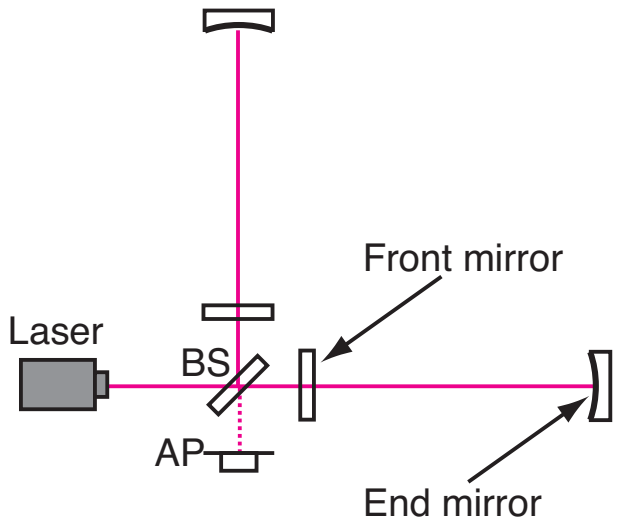

Figure B.1 Fabry-Perot Michelson interferometer.

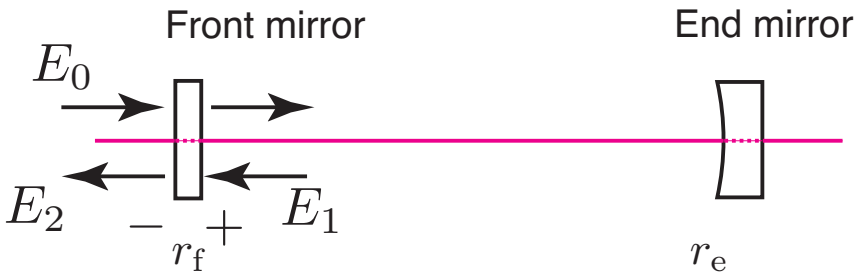

Figure B.2 Fabry-Perot cavity.

B.1 Phase modulation by gravitational waves in the Fabry-Perot cavity

Consider a gravitational wave is incident on the Fabry-Perot cavity in the vertical direction with plus polarization. Then the time interval Δt_x required for the one round trip in x-direction is represented in Eq.(3.8). The phase evolution after the n round trips is

$$\phi_n = \frac{2\Omega_0 L}{c} n + \frac{\Omega_0}{2} \int_{t-2nL/c}^{t} h(t)\, dt. \tag{B.1}$$

From Eq.(3.14), it is

$$\phi_n = \frac{2\Omega_0 L}{c} n + \frac{\Omega_0}{2} \int_{-\infty}^{\infty} h(\omega) \frac{1 - \mathrm{e}^{-\mathrm{i}\frac{2L\omega}{c} n}}{\mathrm{i}\omega} \mathrm{e}^{\mathrm{i}\omega t}\, d\omega. \tag{B.2}$$

Consider the light field $E_0 \mathrm{e}^{\mathrm{i}\Omega_0 t}$ is incident on the Fabry-Perot cavity. Then the circulating light field $E_1 \mathrm{e}^{\mathrm{i}\Omega_0 t}$ is (see Figure B.2)

$$E_1 = t_\mathrm{f} r_\mathrm{e} \mathrm{e}^{-\mathrm{i}\phi_1} E_0 + t_\mathrm{f} r_\mathrm{f} {r_\mathrm{r}}^2 \mathrm{e}^{-\mathrm{i}\phi_2} E_0 + \dots \tag{B.3}$$

$$= t_\mathrm{f} r_\mathrm{e} \sum_{n=1}^{\infty} (r_\mathrm{f} r_\mathrm{e})^{n-1} \mathrm{e}^{-\mathrm{i}\phi_n} E_0. \tag{B.4}$$

Without gravitational waves, the round-trip phase is

$$\phi_n = 2nL\Omega_0/c = 2k\pi \ \ (k \in \mathbb{Z}), \tag{B.5}$$

thus $\mathrm{e}^{-\mathrm{i}\phi_n} = 1$ then,

$$E_1 = \frac{t_\mathrm{f} r_\mathrm{e}}{1 - r_\mathrm{f} r_\mathrm{e}} E_0. \tag{B.6}$$

From Eq.(B.2) and the relation

$$\exp(-\mathrm{i}\phi_n) \simeq \mathrm{e}^{-\mathrm{i}\frac{2\Omega_0 L}{c} n} \left(1 - \mathrm{i}\frac{\Omega_0}{2} \int_{-\infty}^{\infty} h(\omega) \frac{1 - \mathrm{e}^{-\mathrm{i}\frac{2L\omega}{c} n}}{\mathrm{i}\omega} \mathrm{e}^{\mathrm{i}\omega t}\, d\omega \right), \tag{B.7}$$

Eq. (B.4) reduces to

$$E_1 = \frac{t_\mathrm{f} r_\mathrm{e}}{1 - r_\mathrm{f} r_\mathrm{e}} E_0 \left\{1 - \mathrm{i}\delta\phi(t)\right\}, \tag{B.8}$$

where

$$\delta\phi(t) = \int_{-\infty}^{\infty} h(\omega) H_\mathrm{FP}(\omega) \mathrm{e}^{\mathrm{i}\omega t}\, d\omega, \tag{B.9}$$

$$H_\mathrm{FP}(\omega) = \frac{\Omega_0}{\omega} \frac{\sin(\omega L/c)}{1 - r_\mathrm{f} r_\mathrm{e} \mathrm{e}^{-\mathrm{i}2\omega L/c}} \mathrm{e}^{-\mathrm{i}\omega L/c}. \tag{B.10}$$

This satisfies $H_\mathrm{FP}(\omega) = H_\mathrm{FP}^*(-\omega)$. Moreover,

$$H_\mathrm{FP}(\omega) = \frac{H_\mathrm{MI}(\omega)}{1 - r_\mathrm{f} r_\mathrm{e} \mathrm{e}^{-\mathrm{i}2\omega L/c}}, \tag{B.11}$$

so H_FP is identical with H_MI if $r_\mathrm{e} = 1, r_\mathrm{f} = 0$.

In the same manner, the calculation about y-direction yeilds

$$E_1 = \frac{t_\mathrm{f} r_\mathrm{e}}{1 - r_\mathrm{f} r_\mathrm{e}} E_0 \left\{1 + \mathrm{i}\delta\phi(t)\right\}. \tag{B.12}$$

B.2 Shot noise limited strain sensitivity

The net amplitude reflectances for x- and y-directions are written

$$r_x = r_\mathrm{reso} - \mathrm{i}\frac{{t_\mathrm{f}}^2 r_\mathrm{e}}{1 - r_\mathrm{f} r_\mathrm{e}} \delta\phi(t), \tag{B.13}$$

$$r_y = r_\mathrm{reso} + \mathrm{i}\frac{{t_\mathrm{f}}^2 r_\mathrm{e}}{1 - r_\mathrm{f} r_\mathrm{e}} \delta\phi(t), \tag{B.14}$$

where $r_\mathrm{reso} = -r_\mathrm{f} + {t_\mathrm{f}}^2 r_\mathrm{e}/(1 - r_\mathrm{f} r_\mathrm{e})$. Thus the light field at the AP is

$$E_\mathrm{AP} = \tfrac{1}{2}(r_y - r_x) E_\mathrm{inc} \tag{B.15}$$

$$= \mathrm{i}\frac{{t_\mathrm{f}}^2 r_\mathrm{e}}{1 - r_\mathrm{f} r_\mathrm{e}} \delta\phi(t) E_\mathrm{inc}. \tag{B.16}$$

Now consider a monochromatic gravitational wave in Eq.(3.37) is propageting in the vertical direction. The Ap light field is

$$E_\mathrm{AP} = E_\mathrm{inc}(a_1 \mathrm{e}^{\mathrm{i}\omega_\mathrm{g} t} + a_{-1} \mathrm{e}^{-\mathrm{i}\omega_\mathrm{g} t}), \tag{B.17}$$

where

$$a_1 = \mathrm{i}\frac{h}{2} \frac{{t_\mathrm{f}}^2 r_\mathrm{e}}{1 - r_\mathrm{f} r_\mathrm{e}} H_\mathrm{FP}(\omega_\mathrm{g}), \tag{B.18}$$

$$a_{-1} = -a_1^*. \tag{B.19}$$

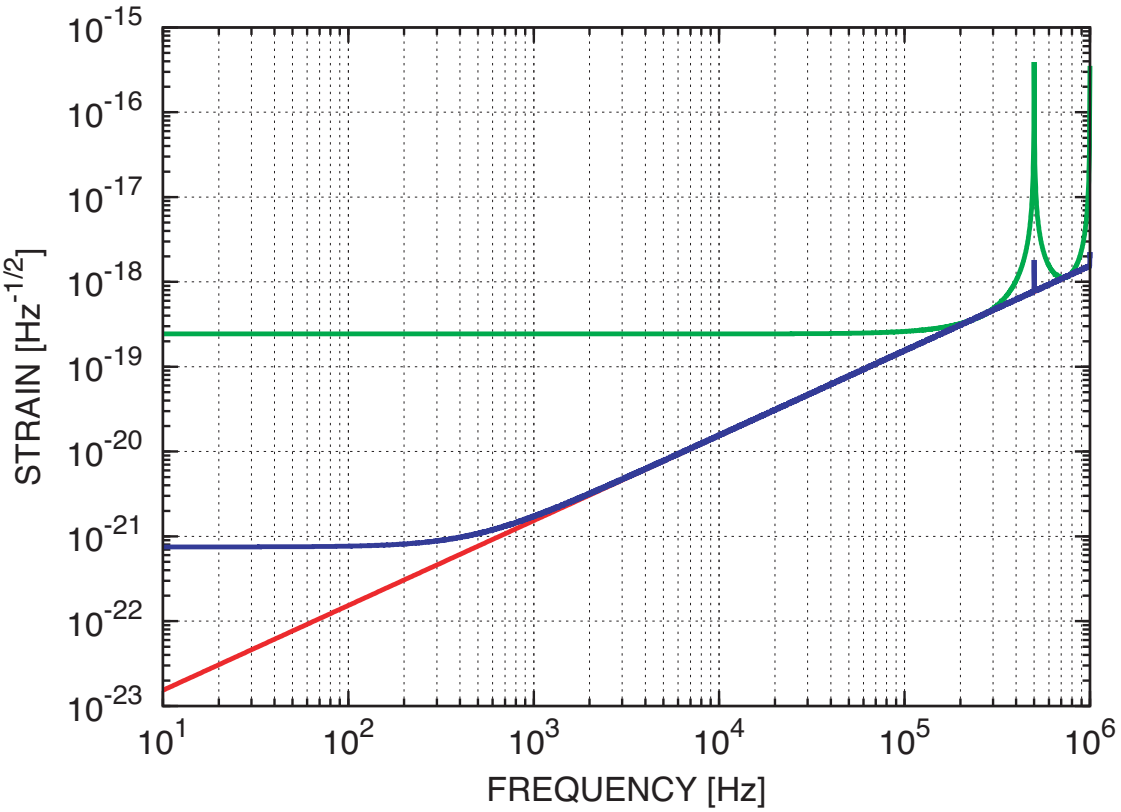

Figure B.3 Comparing the shot noise limited sensitivities of FPMI and MI. The red and green curves, which are the same ones as illustrated in FigureA.2, represent the detection limits of MI for each frequency, and the detection limit when the arm length is fixed at $L = 300$ m, respectively. The blue curve is that of FPMI, where each arm lenght is fixed at$L = 300\,\mathrm{m}$. The intensity of incident light is assumed $0.5\,\mathrm{W}$.

In the same manner as the calculation for the synchronous recycling interferometer, the interferometer response function is

$$G_{\mathrm{FPMI}}(\omega) = \frac{{t_{\mathrm{f}}}^2 r_{\mathrm{e}}}{1 - r_{\mathrm{f}} r_{\mathrm{e}}} H_{\mathrm{FP}}(\omega), \tag{B.20}$$

and the shot noise limited strain sensitivity is

$$h_{\mathrm{FPMI}}^{\mathrm{shot}} = \sqrt{\frac{2\hbar\Omega_0}{\eta \bar{P}_{\mathrm{inc}}}} \frac{1}{2\,|G_{\mathrm{FPMI}}|}. \tag{B.21}$$

Consider that the desired frequency of gravitational waves is $\nu_{\mathrm{g}} = \omega_{\mathrm{g}}/(2\pi)$. At the frequency, $|H_{\mathrm{FP}}|$ will be maximized when each arm length is

$$L = \frac{c}{4\nu_{\mathrm{g}}}, \tag{B.22}$$

in the same manner as the Michelson interferometer. Then one finds

$$|G_{\mathrm{FPMI}}| = \frac{\nu_0}{\nu_{\mathrm{g}}} \frac{{t_{\mathrm{f}}}^2 r_{\mathrm{e}}}{1 - (r_{\mathrm{f}} r_{\mathrm{e}})^2}. \tag{B.23}$$

If $r_{\mathrm{e}} = 1$, one finds

$$|G_{\mathrm{FPMI}}| = \frac{\nu_0}{\nu_{\mathrm{g}}}. \tag{B.24}$$

Appendix C

Geometry of the recycling cavity

In this chapter, the stability condition and the eigenmode of the recycling cavity is described.

C.1 ABCD matrix

The recycling cavity corresponds to the lens sequence [58, 79, 80] shown in Figure C.1. In this figure, each lens is labeled as $2s, 2s+1, \ldots$ and so on.

Assume that the both end mirrors have the same curvature, while the recycling mirror and the transfer mirror has flat surfaces[1]. Then we can write the ABCD matrix [58, 80] of the recycling cavity in the following form:

$$\begin{pmatrix} A & B \\ C & D \end{pmatrix} = \begin{pmatrix} 1 & 0 \\ -\frac{2}{R} & 1 \end{pmatrix} \begin{pmatrix} 1 & 2L_2 \\ 0 & 1 \end{pmatrix} \begin{pmatrix} 1 & 0 \\ -\frac{2}{R} & 1 \end{pmatrix} \begin{pmatrix} 1 & 2L_1 \\ 0 & 1 \end{pmatrix}, \tag{C.1}$$

where R is the radius of curvature of each end mirror, $2L_1$ is the optical distance between the end mirrors via the recycling mirror, and $2L_2$ is the optical distance between the end mirrors via the transfer mirror. The components of the left-hand

[1] In our design, the laser beam should be bent to nealy 90° at the recycling mirror and the transfer mirror, because curved mirrors that will reflect beas by 45° indient angle (with high reflectance suitable for cavity use) are not usually available today.

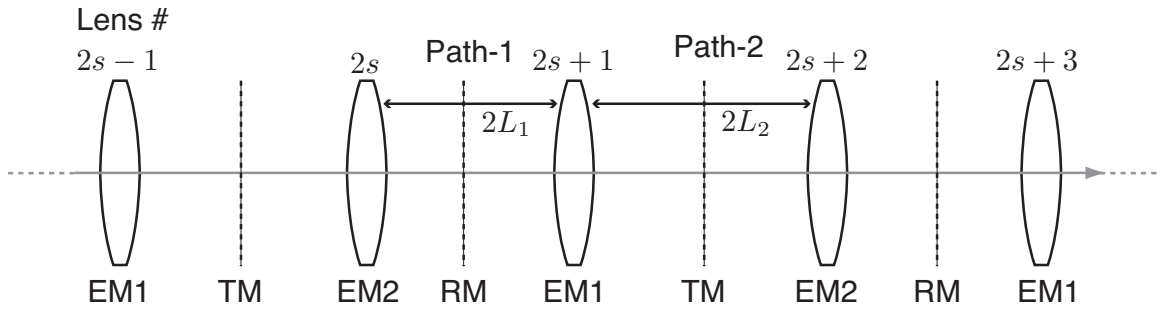

Figure C.1 Lens sequence model of the recycling cavity. The indices $2s$, $2s+1$, and so on are lens numbers. For each lens, the corresponding mirror name (EM1 or EM2) is attached. The black broken lines represent the flat mirrors (RM or TM). The gray solid arrow represents the propagation direction of the laser beam; in this case the laser beam circulates in the counter-clockwise direction. Path-1 represents the optical path between $(2s)$- and $(2s+1)$-th lenses, while path-2 represents the optical path between $(2s+1)$- and $(2s+2)$-th lenses. The lengths of path-1 and -2 are $2L_1$ and $2L_2$, respectively.

side are

$$A = 1 - \frac{4L_2}{R}, \tag{C.2a}$$

$$B = 2L_1 + 2L_2\left(1 - \frac{4L_1}{R}\right), \tag{C.2b}$$

$$C = -\frac{4}{R} + \frac{8L_2}{R^2}, \tag{C.2c}$$

$$D = -\frac{4L_1}{R} + \left(1 - \frac{4L_2}{R}\right)\left(1 - \frac{4L_1}{R}\right). \tag{C.2d}$$

Note that a laser beam incident on a spherical mirror with an incident angle $\theta \neq 0$ sees different radii of curvature between x-derction[2] and y-direction[3]. The effective radii of curvature of the spherical mirror are written as $R_x = R\cos\theta$ for x-direction and $R_y = R/\cos\theta$ for y-direction (for example, see Ref. [60]). For simplicity, we use the symbol R as a representative of R_x and R_y until the distinction is needed.

[2] Perpendicular to z-direction (beam's propagation direction), but parallel with the surface including incident and reflected beams.

[3] perpendicular to both z- and x- directions.

C.2 Stability condition

In order that the laser light is trapped and resonant in the cavity, the required condition is [58]

$$\left|\frac{A+D}{2}\right| \leq 1. \tag{C.3}$$

From Eqs. (C.2a) and (C.2d), the above inequality can be rewritten as

$$0 \leq \left(1-\frac{2L_1}{R}\right)\left(1-\frac{2L_2}{R}\right) \leq 1. \tag{C.4}$$

This is the stability condition of the recycling cavity.

C.3 Basic eigenmode

The laser beam, which is resonant in the cavity represented by Eq.(C.1), follows the condition

$$q_{2(s+1)} = \frac{Aq_{2s}+B}{Cq_{2s}+D} = q_{2s}, \tag{C.5}$$

where q_{2s} represents the factor $q(z)$ at $(2s)$-th lens [$q(z)$ is defined in Eq.(5.1)].

Solving the above equation about q_{2s}, one obtains

$$\frac{1}{q_{2s}} = \frac{D-A}{2B} \pm \mathrm{i}\frac{1}{B}\sqrt{1-\left(\frac{A+D}{2}\right)^2}. \tag{C.6}$$

Thus the radius of curvature of the beam wavefront at $(2s)$-th lens is

$$R_1 = \frac{2B}{D-A} \tag{C.7}$$

$$= -\frac{R}{2}\left\{1+\frac{L_2}{L_1}\frac{\left(1-\frac{2L_1}{R}\right)}{\left(1-\frac{2L_2}{R}\right)}\right\}, \tag{C.8}$$

where Eqs.(5.1) and (C.2) are used. Note that R represents the radius of curvature of each end mirror, not of the beam wavefront. Also, the (squared) spot radius at $(2s)$-th lens is

$$w_1^2 = \frac{\lambda_0}{\pi}\left[\frac{1}{B}\sqrt{1-\left(\frac{A+D}{2}\right)^2}\right]^{-1} \tag{C.9}$$

$$= \frac{\lambda_0}{\pi}\left/\sqrt{\frac{(L_1+L_2-2L_1L_2/R)(1-2L_1/R)(1-2L_2/R)}{R(L_1+L_2-4L_1L_2/R)^2}}\right. . \tag{C.10}$$

By exchanging L_1 and L_2 in the above equation, the radius of curvature of the beam wavefront at $(2s+1)$-th lens is

$$R_2 = -\frac{R}{2}\left\{1 + \frac{L_1}{L_2}\frac{\left(1-\frac{2L_2}{R}\right)}{\left(1-\frac{2L_1}{R}\right)}\right\}. \tag{C.11}$$

The beam radius at $(2s+1)$-th lens is $w_2 = w_1$, the same as the one at $(2s)$-th lens.

Now let us find the basic eigenmode of the recycling cavity, that is, the beam waists and the waist radii of the laser light that can be resonant in the cavity. Because the beam radii at the both ends of the path-1 [from $(2s)$-th lens to $(2s+1)$-th lens] are equal: $w_1 = w_2$, the beam waist of the path-1 is at the midpoint of this path, where the distance from each end mirror is L_1. From Eqs.(5.5) and (C.8), the waist radius in path-1 is

$$w_{01} = \sqrt{\frac{\lambda L_1}{\pi}}\left(\frac{|R_1|}{L_1} - 1\right)^{1/4}. \tag{C.12}$$

In the same manner, the beam waist in path-2 [from $(2s+1)$-th lens to $(2s+2)$-th lens] is at the midpoint of the path, where the distance from each end mirror is L_2, and the waist radius is

$$w_{02} = \sqrt{\frac{\lambda L_2}{\pi}}\left(\frac{|R_2|}{L_2} - 1\right)^{1/4}. \tag{C.13}$$

Note that these waists are at the recycling mirror and the transfer mirror.

C.4 Transverse-mode spacing

The phase evolution of the laser light resonant in the cavity is [58]

$$\phi(z) = \tan^{-1}\left(\frac{\lambda_0(z-z_0)}{\pi w_0^2}\right), \tag{C.14}$$

where z_0 is the beam waist. If the laser beam is in the ellipsoidal Gaussian mode, that is, the form of the beams (characterized by $q(z)$) are different for x- and y-directions, the phase evolution is modified as

$$\phi(z) = \tan^{-1}\left[\frac{\lambda_0(z-z_0)}{\pi w_{x0}^2}\right] + \tan^{-1}\left[\frac{\lambda_0(z-z_0)}{\pi w_{y0}^2}\right], \tag{C.15}$$

where w_{x0} and w_{y0} are the waist radii for x- and y-directions, respectively.

In the path-1,

$$\Delta\phi_1 = \phi_1(z_0+L_1) - \phi_1(z_0-L_1) \tag{C.16}$$

$$= (2\ell_x+1)\tan^{-1}\left[\frac{\lambda_0 L_1}{\pi w_{x01}^2}\right] + (2\ell_y+1)\tan^{-1}\left[\frac{\lambda_0 L_1}{\pi w_{y01}^2}\right] - 2kL_1, \tag{C.17}$$

and in the path-2,

$$\Delta\phi_2 = \phi_2(z_0 + L_2) - \phi_2(z_0 - L_2) \tag{C.18}$$

$$= (2\ell_x + 1)\tan^{-1}\left[\frac{\lambda_0 L_2}{\pi w_{x02}^2}\right] + (2\ell_y + 1)\tan^{-1}\left[\frac{\lambda_0 L_2}{\pi w_{y02}^2}\right] - 2kL_2. \tag{C.19}$$

Thus the total phase evolution is written as

$$\Delta\phi = \Delta\phi_1 + \Delta\phi_2 \tag{C.20}$$

$$= \left(\ell_x + \frac{1}{2}\right)2\pi\gamma_x + \left(\ell_y + \frac{1}{2}\right)2\pi\gamma_y - 2\pi n \tag{C.21}$$

where ℓ_x and ℓ_y are integers, while $n = 2(L_1 + L_2)/\lambda_0$ is also an integer, and

$$\gamma_x = \frac{1}{2\pi}\left\{\cos^{-1}\left[1 - \frac{2L_1}{R_{x1}}\right] + \cos^{-1}\left[1 - \frac{2L_2}{R_{x2}}\right]\right\}, \tag{C.22}$$

$$\gamma_y = \frac{1}{2\pi}\left\{\cos^{-1}\left[1 - \frac{2L_1}{R_{y1}}\right] + \cos^{-1}\left[1 - \frac{2L_2}{R_{y2}}\right]\right\}. \tag{C.23}$$

When the laser light is resonant in the recycling cavity, the condition

$$\Delta\phi = 2\pi n' = 2\pi\frac{2(L_1 + L_2)}{c}\nu_{n,\ell_x,\ell_y} \tag{C.24}$$

(n' is an integer) is met. Thus the frequency of the light resonant in the cavity is

$$\nu_{n,\ell_x,\ell_y} = \frac{c}{2(L_1 + L_2)}\left\{n + \left(\ell_x + \frac{1}{2}\right)\gamma_x + \left(\ell_y + \frac{1}{2}\right)\gamma_y\right\}. \tag{C.25}$$

As a result, the free-spectral range and the transverse-mode spacing are

$$\nu_{\mathrm{FSR}} = \frac{c}{2(L_1 + L_2)}, \tag{C.26}$$

$$\Delta\nu_{\ell_x} = \nu_{\mathrm{FSR}}\,\gamma_x, \tag{C.27}$$

$$\Delta\nu_{\ell_y} = \nu_{\mathrm{FSR}}\,\gamma_y. \tag{C.28}$$

Appendix D

Circuits

- In the captions of the following circuits, SP means symmetric port, AP means antisymmetric port.
- The concept of photodetectors with resonant circuits are the standard technique that we generally use for the laser interferometric gravitational-wave detectors [81, 82, 83].

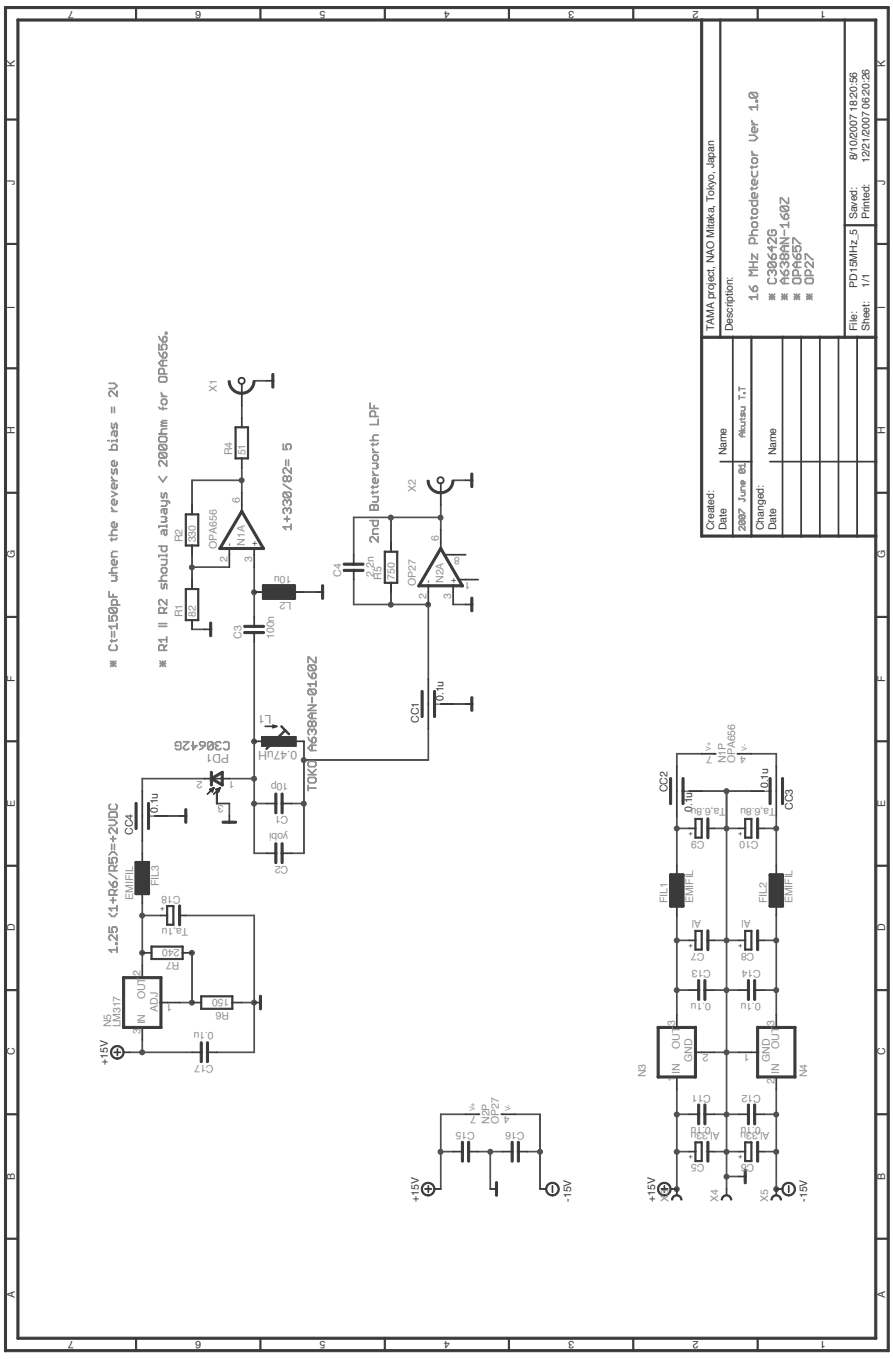

Figure D.1 AP Photodetector with resonant circuit at 14.7 MHz.

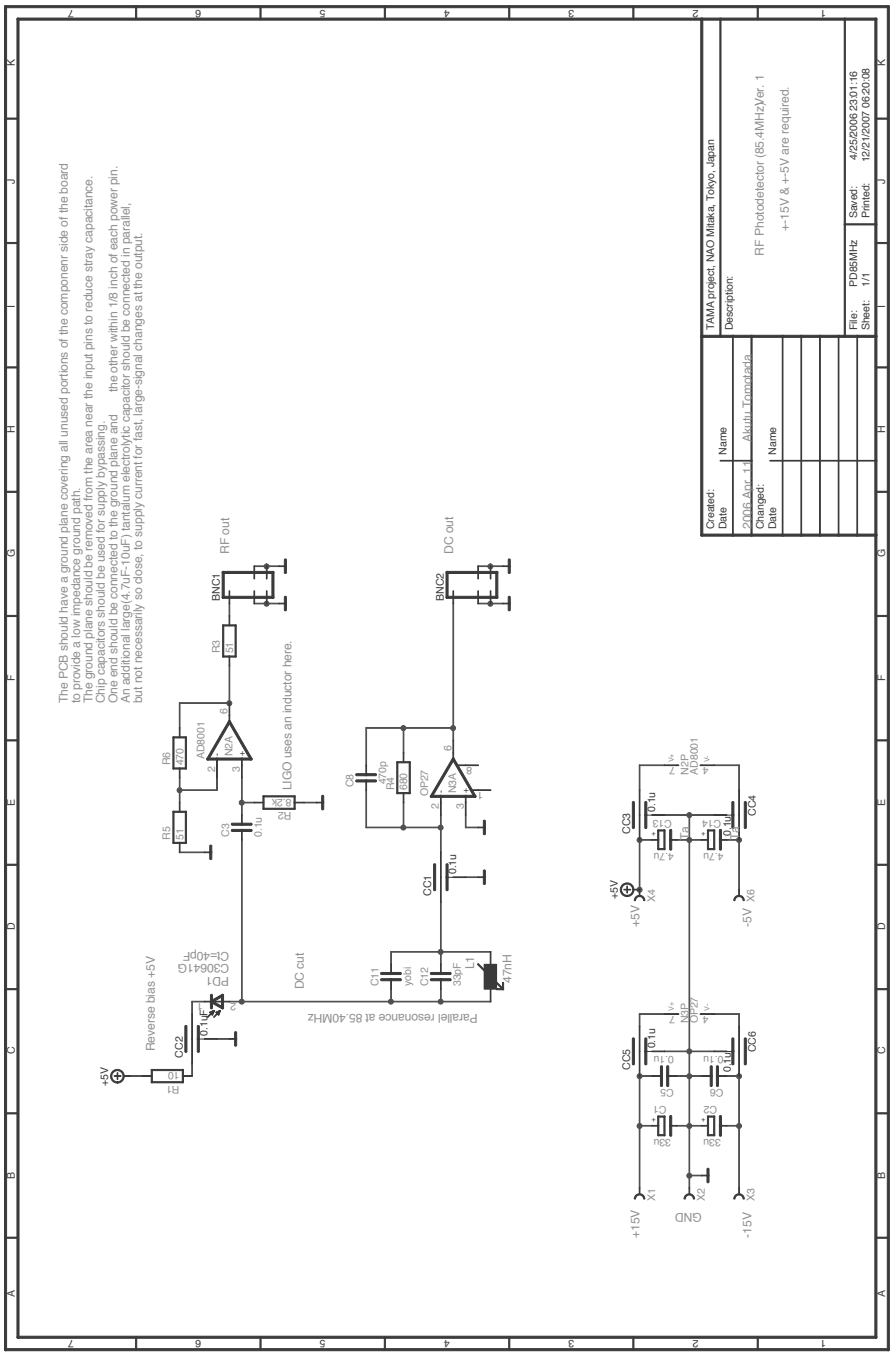

Figure D.2 SP1 Photodetector with resonant circuit at 85.4 MHz.

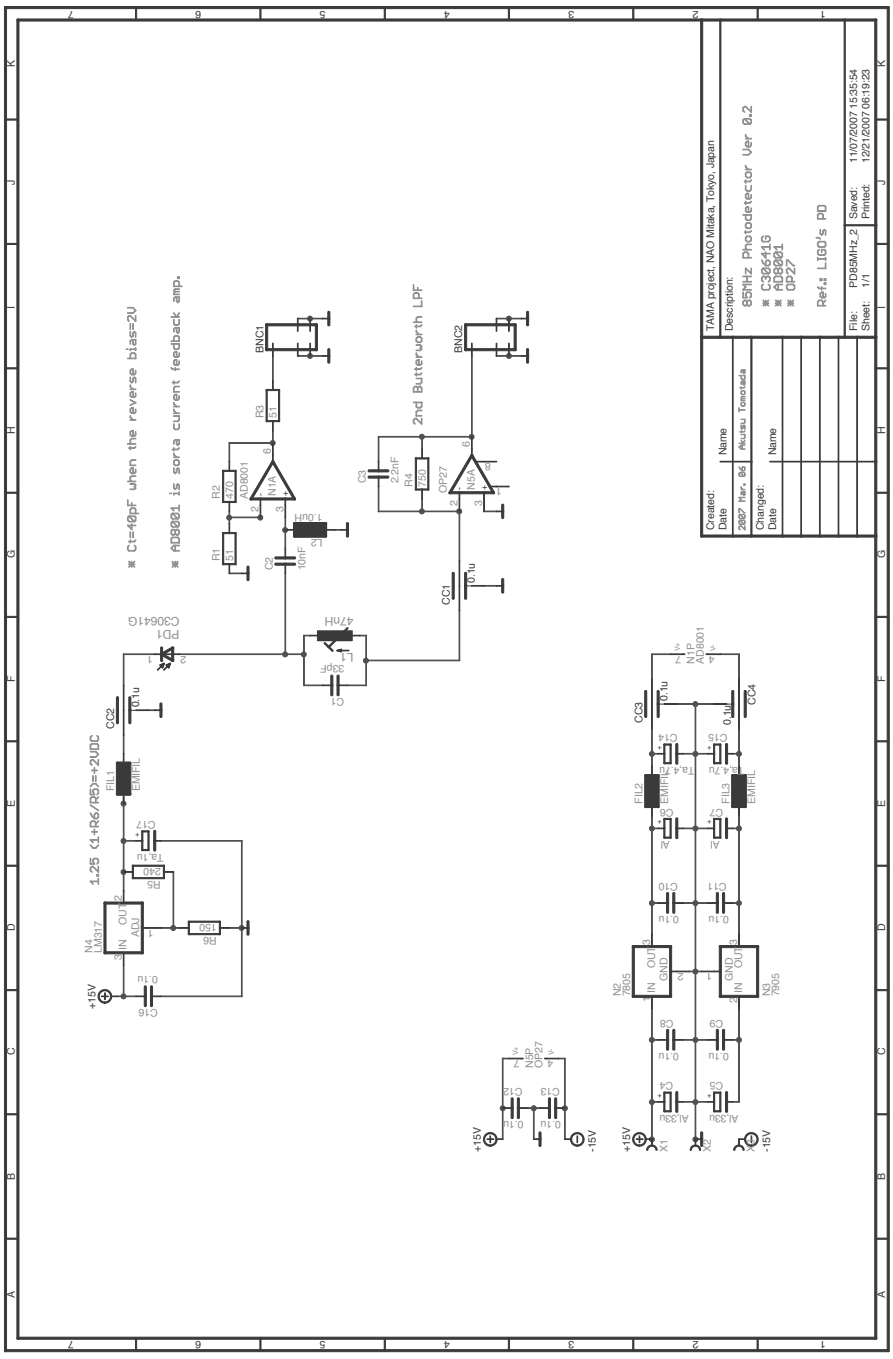

Figure D.3 SP2 Photodetector with resonant circuit at 85.4 MHz.

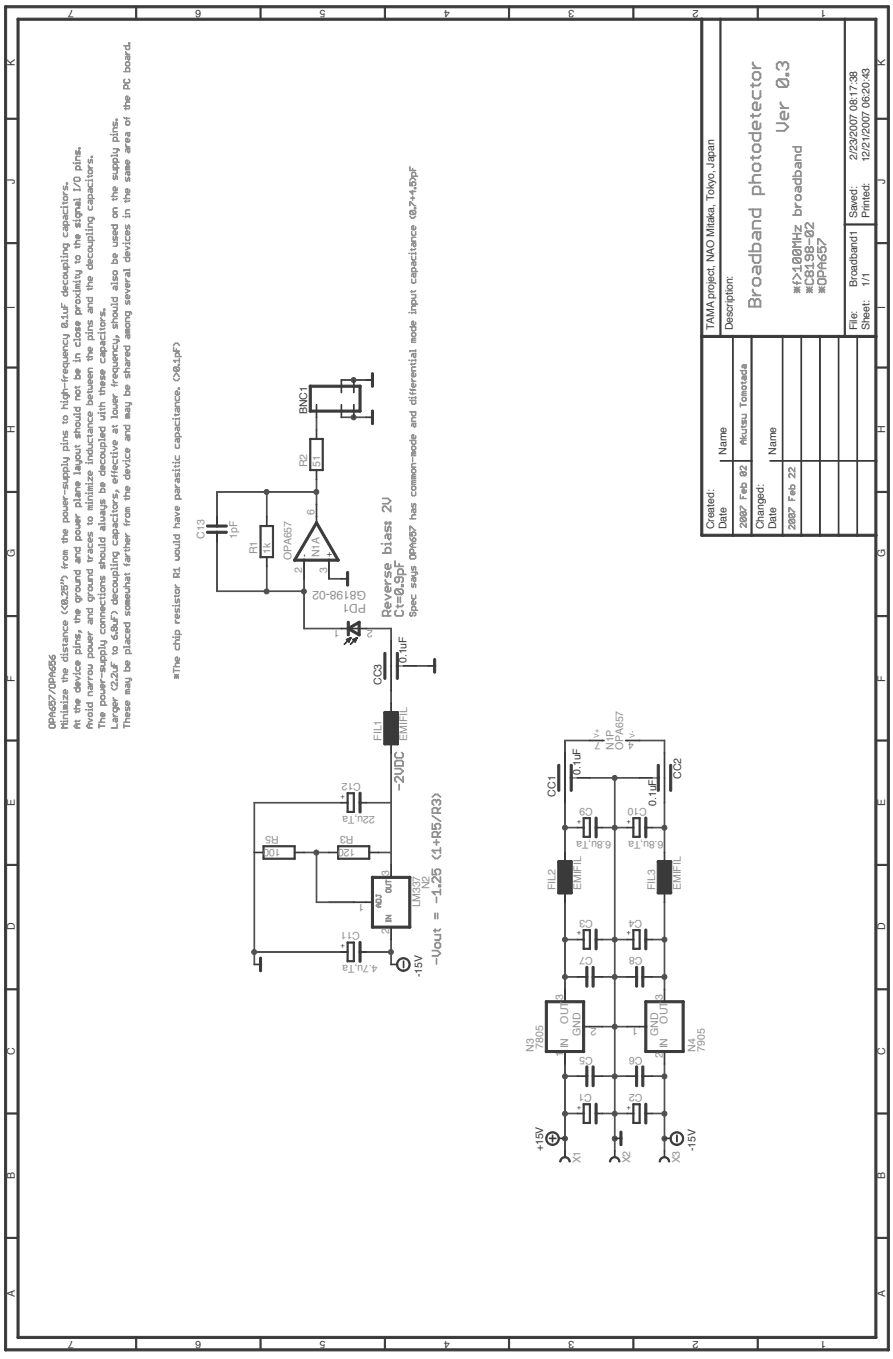

Figure D.4 Broadband photodetector (up to 100 MHz).

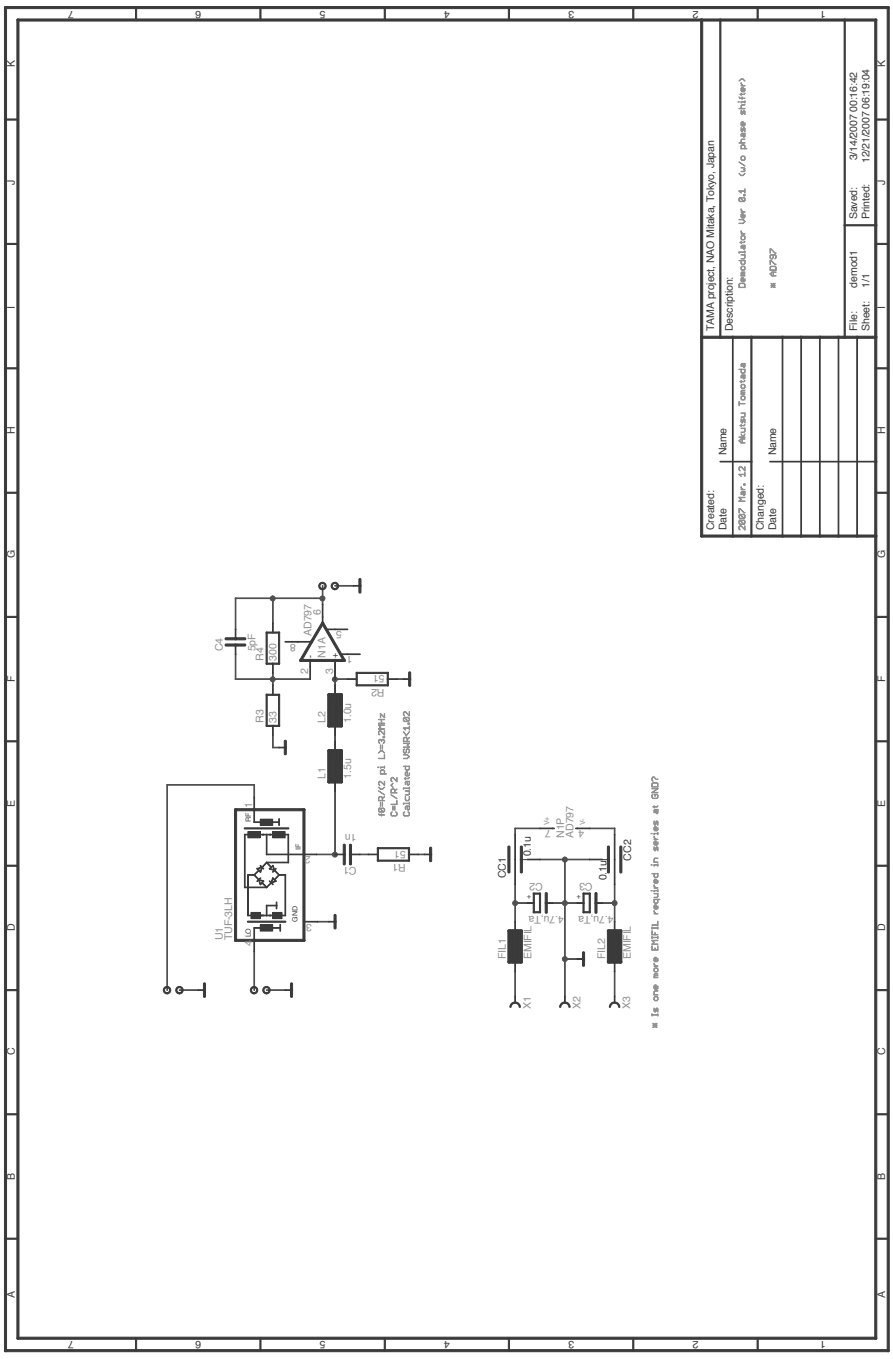

Figure D.5 Demodulator at SP

Bibliography

[1] C. W. Misner, K. S. Thorne, and J. A. Wheeler, *Gravitation*, W. H. Freeman (1973)

[2] B. F. Schutz, *A first course in general relativity*, Cambridge (1985) [translated into Japanese by Y. Eriguchi and T. Futamase, 相対論入門 上・下, 丸善]

[3] J. H. Hulse and R. A. Taylor, ApJ, **195**, l51 (1975)

[4] J. M. Weisberg and J. H. Taylor, "Relativistic Binary Pulsar B1913+16: Thirty Years of Observations and Analysis", astro-ph/0407149

[5] J. Weber, Phys. Rev. Lett. **20**, 1307 (1968)

[6] R. L. Forward, Phys. Rev. D **17**, 379 (1978)

[7] M. Ando et al., Class. Quantum. Grav. **22**, S881 (2005)

[8] D. Sigg, Class. Quantum. Grav. **21**, S409 (2004)

[9] B. Willke et al., Class. Quantum. Grav. **24**, S389 (2007)

[10] F. Acernese et al, Class. Quantum Grav. **21**, S385 (2004)

[11] S. Miyoki et al., Class. Quantum. Grav. **23**, S231 (2006)

[12] K. Kuroda et al., Class. Quantum. Grav. **23**, S215 (2006)

[13] LISA: System and Technology Study Report, ESA document ESA-SCI (2000)

[14] S. Kawamura et al., Class. Quantum. Grav. **23**, S125 (2006)

[15] P. J. E. Peebles and A. Vilenkin, Phys. Rev. D **59**, 063505 (1999)

[16] M. Giovannini, Phys. Rev. D **60**, 123511 (1999)

[17] M. Giovannini, Phys. Rev. D **58**, 083504 (1998)

[18] A. Riazuelo and J. P. Uzan, Phys. Rev. D **62**, 083506 (2000)

[19] H. Tashiro, T. Chiba, and M. Sasaki, Class. Quantum. Grav. **21**, 1761 (2004)

[20] R. Easther and E. A. Lim, astro-ph/0601617

[21] J. Garcia-Bellido and D. G. Figueroa, Phys. Rev. Lett. **98**, 061302 (2007)

[22] J. Dufaux, A. Bergman, G. Felder, L. Kofman, and J. Uzan, arXiv:0707.0875

[23] M. Gasperini and M. Giovannini, Phys. Rev. D **47**, 1519 (1993)

[24] R. Brustein, M. Gasperini, M. Giovannini, and G. Veneziano, Phys. Lett. B **361**, 45 (1995)

[25] M. Gasperini and G. Veneziano, Phys. Rep. **373**, 1 (2003)

[26] T. Nakamura, M. Sasaki, T. Tanaka, and K. S. Thorne, ApJL **487**, 139 (1997)

[27] K. Ioka, T. Chiba, T. Tanaka, and T. Nakamura, Phys. Rev. D **58**, 063003 (1998)

[28] G. S. Bisnovatyi-Kogan and V. N. Rudenko, Class. Quantum. Grav. **21**, 3347 (2004)

[29] S. S. Seahra, C. Clarkson, and R. Maartens, Phys. Rev. Lett. **94**, 121302 (2005)
[30] C. Clarkson and S. S. Seahra, Class. Quantum. Grav. **24**, F33 (2007)
[31] T. L. Smith, M. Kamionkowski, and A. Cooray, Phys. Rev. D **73**, 023504 (2006)
[32] F. A. Jenet et al., ApJ **653**, 1571 (2006)
[33] J. W. Armstrong, L. Iess, P. Tortora, and B. Bertotti, ApJ **599**, 806 (2003)
[34] B. Abbott et al., ApJ, **659**, 918 (2007)
[35] M. Maggiore, Phys. Rep. **331**, 283 (2000)
[36] A. M. Cruise and R. M. J. Ingley, Class. Quantum. Grav. **23**, 6185 (2006)
[37] A. M. Cruise, MNRAS **204**, 485 (1983)
[38] R.W.P. Drever, *Gravitational Radiation*, edited by N. Deruelle and T. Piran, North-Holland (1983), p.321
[39] N. Seto, S. Kawamura, and T. Nakamura, Phys. Rev. Lett. **87**, 221103 (2001)
[40] A. Nishizawa et al., Phys. Rev. D **77**, 022002 (2008) [see also arXiv:0710.1944]
[41] J.-Y. Vinet, B. Meers, C. N. Man, and A. Brillet, Phys. Rev. D **38**, 433 (1988)
[42] B. J. Meers, Phys. Rev. D **38**, 2317 (1988)
[43] W. M. Yao et al., J. Phys. G33, 1; Particle Data Group, "Review of Particle Physics" (2006)
[44] D. N. Spergel et al., ApJS, **170**, 377 (2007)
[45] L. Grishchuk et al., "Definitions of the Energy Density Spectrum in Stochastic Gravitational Waves", LIGO Technical Note T060270-00-Z (2006)
[46] B. Allen and J.D. Romano, Phys. Rev. D **59**, 102001 (1999)
[47] R. Schilling, Class. Quantum. Grav. **14**, 1513 (1997)
[48] A. Nishizawa et al., "Optimal Location of Two Laser-interferometric Detectors for Gravitational Wave Backgrounds at 100 MHz", arXiv:0801.4149v1, submitted to Phys. Rev. D
[49] S. Kawamura and Y. Chen, Phys. Rev. Lett. **93**, 211103 (2004)
[50] Y. Chen and S. Kawamura, Phys. Rev. Lett. **96**, 231102 (2006)
[51] B. Abbott et al., Phys. Rev. D **69**, 122004 (2004)
[52] B. Abbott et al., Phys. Rev. Lett. **95**, 221101 (2005)
[53] R. W. P. Drever, J. L. Hall, F. V. Kowalski, J. Hough, G. M. Ford, and H. Ward, Appl. Phys. B **31**, 97 (1983)
[54] Lise Schnupp, *unpublished*
[55] A. Araya et al., Appl. Opt. **38**, 2848 (1999)
[56] R. G. DeVoe and R. G. Brewer, Phys. Rev. A **30**, 2827 (1984)
[57] A. E. Siegman, *Lasers*, University Science Books (1986)
[58] A. Yariv, *Optical Electronics in Modern Communications* 5th ed., Oxford (1997) [translated into Japanese by K. Tada and T. Kamiya, 光エレクトロニクス 基礎編・展開編, 丸善]
[59] K.-X. Sun, M. M. Fejer, E. Gustafson, and R. L. Byer, Phys. Rev. Lett. **76**, 3053 (1996)
[60] 新井 宏二, 3 枚鏡 ring 型モードクリーナーのモードの計算 (1995) [K. Arai, internal

report *in Japaniese*]
[61] J. S. Bendat and A. G. Piersol, *Random Data: Analyis and Measurement Procedures* 3rd ed., Wiley (2000)
[62] G. Arfken, *Mathematical methods for physicists* 2nd ed., Academic Press (1970)
[63] N. L. Christensen, "On measuring the stochastic gravitational radiation background with laser interferometer antennas", Ph.D. Thesis, Massachusetts Institute of Technology (1990)
[64] N. Christensen, Phys. Rev. D **46**, 5250 (1992)
[65] E. E. Flanagan, Phys. Rev. D **48**, 2389 (1993)
[66] R. L. Fante, *Signal analysis and estimation*, Wiley (1988)
[67] P. D. Welch, IEEE Transactions on Audio and Electroacoustics, AU-**15**, 70 (1967)
[68] J. T. Whelan, "Cross-correlation of windowed, discretely-sampled data", LIGO Technical Note T040125-00-Z (2004)
[69] P. R. Bevington and D. K. Robinson, *Data Reduction and Error Analysis for the Physical Sciences* 3rd ed., McGraw-Hill (2003)
[70] A. Lazzarini and J. Romano, "Use of overlapping windows in the stochastic background search", LIGO Technical Note T040089-00-Z (2004)
[71] D. Shoemaker, R. Schilling, L. Schnupp, W. Winkler, K. Maischberger, and A. Rüdiger, Phys. Rev. D **38**, 423 (1988)
[72] T. M. Niebauer, R. Schilling, K. Danzmann, A. Rüdiger, and W. Winkler, Phys. Rev. A **43**, 5022 (1991)
[73] B .J. Meers and K. A. Strain, Phys. Rev. A **44**, 4693 (1991)
[74] N. Mio and K. Tsubono, Phys. Lett. A **164**, 255 (1992)
[75] M. B. Gray, A. J. Stevenson, H.-A. Bachor, and D. E. McClelland, Opt. Lett. **18**, 759 (1993)
[76] H. J. Kimble, Y. Levin, A. B. Matsko, K. S. Thorne, and S. P. Vyatchanin, Phys. Rev. D **65**, 022002 (2001)
[77] D. Sigg et al., "Frequency Response of the LIGO Interferometer", LIGO Technical Note T970084-00-D (1997)
[78] R. Adhikari, "Sensitivity and noise analysis of 4 km laser interferometric gravitational wave anntenae", Ph.D. Thesis, Massachusetts Institute of Technology (2004)
[79] H. Kogelnik, Appl. Opt. **4**, 1562 (1965)
[80] H. Kogelnik and T. Li, Appl. Opt. **5**, 1550 (1966)
[81] G. Heinzel, "Advanced optical techniques for laser-interferometric gravitational-wave detectors", Dr. rer. nat. Thesis, Universität Hannover (1999)
[82] N. Mio, M. Ando, G. Heinzel, and S. Moriwaki, Jpn. J. Appl. Phys. **40**, 426 (2001)
[83] H. Grote, Rev. Sci. Instrum. **78**, 054704 (2007)

Acknowledgment

To all who have supported me, I would like to express my thanks in Japanese.
本研究にあたり，たくさんの方にお世話になりました．心より感謝申し上げます．

国立天文台の藤本教授，川村准教授からはご指導，ご助言をいただくとともに，自由に研究に専念できる環境を提供していただきました．また，同・新井助教には実験に不可欠な技術を教えていただくとともに，さまざまな議論におつきあいいただきました．同・高橋助教および辰巳助教からは，いろいろな面でご助言いただきました．同・山元研究員には，短い間でしたが実験にご協力いただきました．同・佐藤研究員（当時）には，気軽な質問にも対応していただきました．同・山崎技師および福嶋技師には，二度にわたる実験室の整備作業[1]について多大な協力をいただきました．また同・事務支援員である近藤さん，西村さん，吉住さんには，物品購入をはじめとする事務手続き一般に関して大変お世話になりました．また，NICT の長野研究員からは，実験を始めるにあたってさまざまなご助言をいただきました．名古屋大学の杉山教授および高橋研究員，日本大学の千葉准教授には本研究を理論面から支えていただきました．

東京大学の坪野教授からは，レーザー光源を貸し出していただけました．また，その運搬にあたっては，同・安東助教に大変お世話になりました．この光源によって二台目の干渉計が完成し，相互相関処理も可能になりました．

私と同じ研究室で D3 の川添さん，阪田さんには，海外渡航で分からないところをいろいろと助けてもらいました．同・D2 の西澤くんには本研究の理論面を大いに助けてもらいました．同・D2 の苔山さんには実験部品の製作に協力してもらいました．JASMINE 推進室 D2 の丹羽くんは測定機材をこころよく貸してくれました．京都大学の阪上教授からは，ためになるお話をたくさん聞かせていただきました．

最後に，博士過程に進学した私を暖かく見守り支えて続けてくれた友人の皆様に，とくに感謝したいと思います．

[1] まさかせっかく整備した北研の実験室から，たった半年で ATC へ引っ越すことになろうとは．